University of Sheffield
Department of Physics and Astronomy

Dynamics and phase separation during spin casting of polymer films

A thesis submitted for the degree of
Doctor of Philosophy

Youmna Mouhamad

November 2014

This thesis is dedicated to my late sister Ilham Mouhamad, in Arabic her first name means inspiration, and that is exactly what she was and still is to me.

Abstract

Spin coating is a process often used to make thin films. A substrate covered with a polymer solution is rotated rapidly. The solution spreads due to the centrifugal force and a film is obtained once the solvent has evaporated. In organic devices, films are often deposited via spin coating. The efficiency of such devices depends on the morphology of the film, which can be controlled by changing the concentration of the solution, the polymer ratio, the solvent, the vapour pressure and the temperature. A full understanding of the dynamics of spin coated films is necessary in order to control the structure of the film.

The thinning rate of spin cast films of polysterene (PS) and poly(methyl methacrylate) (PMMA) was investigated using time-resolved optical reflectivity. Spin coating is usually modelled by accounting for the centrifugal forces and a constant evaporation rate. We show that an accurate modelling of the early stage of the process requires consideration of the speed difference between the fluid and the substrate (inertial forces). We propose a model for spin coating of polymer solutions which accounts for these inertial forces, the centrifugal forces, a constant evaporation rate and a concentration dependent viscosity (Huggins viscosity). This model is in good agreement with the experimental data and enables modelling of the polymer concentration during the coating.

In-situ light scattering was used to monitor development of a structure during coating of solutions of PS and PMMA in toluene, with solvent volume fractions of 90%, 86%, and 88% at 21°C. The phase separation was less pronounced as the toluene volume fraction increases. A mean field theory (Flory-Huggins) was applied, and it revealed that despite the different structure the thermodynamics of the process is unchanged and the drying rate increases with the solvent concentration.

We studied how the interactions between the PS and PMMA chains affect the structure of the film by controlling the temperature prior to and during coating. The experiment was performed at four temperatures: 21°C, 15°C, 7°C and 0°C. The polymer solutions studied had equal amounts of PS and PMMA with toluene volume fractions of 90, 86, and 88%. UV-visible spectroscopy showed that at 0°C these solutions entered the two phase region. There seem to be little correlation between the morphology of the film and the miscibility of the solution. The results are discussed in terms of the evaporation rate, the thickness of the film and instabilities in the film due to the different surface gradient (the Marangoni effect).

Acknowledgements

Foremost I would like to thank my supervisor Professor Mark Geoghegan for guiding me through my PhD while leaving enough flexibility for me to explore the aspects in my project that interested me. I am also very grateful for his support and understanding during the challenges I encountered in my PhD and in my personal life when they affected my work. I would like to thank him for not only being a supervisor but also a mentor, who cares about the personal development of his students.

Many thank to Dr Parvaneh Mokarian-Tabari who besides the physical distance that separates us has always been available to discuss my data or give me guidance with the experimental set up. She has also been a great mentor giving valuable advice in my career plan. I also would like to thank Professor Nigel Clarke and his PhD student Sam Coveney for the insightful discussions. I would like to thank Professor Richard A.L Jones for his support and the Engineering and Physical Sciences Research Council for financing this research.

I would like to thank the mechanical workshop, especially Mr Simon Dixon and Mr Paul Kemp-Russell who helped me to resolve the many challenges faced with the optospinometer. I particularly would like to thank them for increasing the safety of the optospinometer and the reproducibility of data acquired with it. I would like to thank Mr Richard Webb for helping me to tackle the computing and the electronic issues that arose with the optospinometer. I would also like to thank Mr Pete Robinson and Mr Chris Vickers for their help.

I am grateful for the friends and colleagues who made my Sheffield experience more enjoyable. Many thank my to sister by heart; Mary Ongore, Safiya Alismaili, Eleonore Carrot, Amayele Dia and Selma Shimutwikeni for their moral support. I would thank Penny and Kevin Carter for their help, kindness and generosity; many thank to their daughter Hazel-Anne for bringing joy and laughter during the challenging times that come with writing a thesis.

Last but not least, I would like thank my parents Mariama Abasse and Mouhamad Moussa for instilling in me many values that were very useful during my PhD. My sister and brother, Nihad, Galeb, Akram, Widaad, Khalil and Iklas for their love and support.

Contents

Nomenclature

$\overrightarrow{\omega}$	Angular velocity vector
ϵ	Aspect ratio
z	Axial coordinate
$\overrightarrow{t_\theta}$	Axial tangential vector
u_z	Axial velocity
W	Axial velocity scale
θ	Azimuthal coordinate
$\overrightarrow{t_r}$	Azimuthal tangential vector
u_θ	Azimuthal velocity
V	Azimuthal velocity scale
k_B	Boltzman constant
l	Bond length
ϕ_∞	Bulk volume fraction
C_∞	Characteristic ratio
CCD	**C**harge-**C**oupled **D**evice
CB	Chlorobenzene
c_RBD	Correction term in the RBD model
c_SE	Correction term in the semi-empirical model
$\overrightarrow{f_{co}}$	Coriolis forces
$\overrightarrow{f_{ce}}$	Centrifugal forces
c	Concentration of polymer
C_e	Constant of evaporation
$\tilde{n}_1$	Complex refractive index of media 1
$\tilde{n}_2$	Complex refractive index of media 2
$\mathrm{T_c}$	Critical temperature

ρ	Density
dPS	Deuterated polystyrene
E	Dimensionless evaporation rate
P^*	Dimensionless pressure
t^*	Dimensionless time
$\overrightarrow{R_n}$	End-end distance
ε	Energy of interaction between two neighbouring monomers
ε	Energy of interaction between two monomers
δH_v	Enthalpy of evaporation
$\triangle S_{mix}$	Entropy
$\triangle H_{mix}$	Enthalpy
EBP	**E**mersli **B**onner **P**eck
e	Evaporation rate
v	Excluded volume
K	Extension coefficient
h_f	Final thickness without post deposition treatment
n_f	Final refractive index
$\triangle G_{mix}$	Flory Huggins free energy
$\overrightarrow{u}$	Fluid velocity vector
$\overrightarrow{u_{in}}$	Fluid velocity vector at the interface of the film and the air
G_{A+B}	Free energy of mixture
G_A	Free energy of polymer A
G_B	Free energy of polymer B
F	Froude number
g_n	Gradient of the time dependent refractive index
R	Gas constant
$\overrightarrow{g}$	Gravitational vector
g	Gravitational constant
E_i	Incoming light
n_i	Initial refractive index
h_o	Initial thickness
χ	Interaction parameter
χ_{w}	Interaction parameter at $\mathrm{T_w}$

χ_c	Interaction parameter at T_c
$[\eta]$	Intrinsic viscosity
ν	Kinematic viscosity
a	Kuhn length
LCST	**L**ower **C**ritical **S**olution **T**emperature
Ma	Marangoni number
k_e	Mass transfer coefficient
x	Mass fraction
J	Mass transfer
$< \vec{R_n^2} >$	Mean-square average end-end
M_w	Molecular Weight
D_{mu}	Mutual diffusion
h_a^*	Normalised annealed thickness
$z*$	Normalised axial coordinate
u_z^*	Normalised axial velocity
$\theta*$	Normalised azimuthal coordinate
u_θ^*	Normalised azimuthal velocity
h_f^*	Normalised final thickness without post deposition treatment
h^*	Normalised thickness
r^*	Normalised radial coordinate
u_r^*	Normalised radial velocity
$\overrightarrow{n}$	Normal vector
x	Number of nearest neighbour
n_b	Number of bonds
N	Number of Kuhn bonds
E_o	Outgoing light
E_{ip}	Parallel component of incoming light
E_{op}	Parallel component of outgoing light
dPEP	Perdeuterated poly(ethylenepropylene)
E_{is}	Perpendicular component of the incoming light
E_{os}	Perpendicular component of the outgoing light
PMMA	Poly(methyl methacrylate)
PS	Polystyrene

PB	Polybutadiene
PI	Polyisoprene
THF	Tetrahydrofolate
PFB	Poly(9,9-dioctylfluorene-co-bis-N,N'-(4-butylphenyl)-bis-N, N'-phenyl-1,4-phenylenediamine)
F8BT	Poly(9,9-dioctylfluorene-co-benzothiadiazole)
P	Pressure
P_o	Pressure scale
q	Radial flow per unit of circumference
r	Radial coordinate
$\overrightarrow{r}$	Radial vector
u_r	Radial velocity
U	Radial velocity scale
R_g	Radius of the gyration
R	Radius of the substrate
r_d	Radius of a droplet
r_p	Reflection coefficient for light polarised parallel to the incident plane
r_s	Reflection coefficient for light polarised perpendicular to the incident plane
n	Refractive index
n_1	Refractive index of media 1
n_2	Refractive index of media 2
RBD	**R**eisfeld **B**ankoff **D**avis
R_H	Relative humidity
RK	**R**unge **K**utta
Re	Reynolds number
Re_{lq}	Reynolds number for a liquid
τ	Shear stress
$\dot{\gamma}$	Shear rate
T_b	Solvent boiling temperature
C_P	Specific heat
η_{sp}	Specific viscosity
w	Spin speed
SD	**S**pinodal **D**ecomposition

$\kappa(\phi)$	Square concentration gradient
b	Step size in the RK methods
Z^*	Surface excess
σ	Surface tension
T	Temperature
t	Time
T_o	Time scale
t_{end}	Time at the end of the instabilities
t_{on}	Time at the onset of the instabilities
t_{eq}	Time at which the inertial forces are negligible
t_{vmax}	Time at which the maximum is reached in the velocity
$t_{\triangle Gmin}$	Time at which the minimum in the free energy is reached
h	Thickness
ϕ_{on}	Toluene Volume fraction the onset of the instabilities
ϕ_{end}	Toluene Volume fraction the end of the instabilities
UCST	**U**pper **C**ritical **S**olution **T**emperature
$u_{z/\mathrm{RBD}}$	Velocity term in the RBD model
$u_{z/\mathrm{SE}}$	Velocity term in the semi-empirical model
$u_{z/\mathrm{M}}$	Velocity term in the Meyerhofer model
$\overrightarrow{f_{vis}}$	Viscous forces
T	Viscous stress tensor
η_{sol}	Viscosity of the solid
η	Viscosity of the solution
η_s	Viscosity of the solvent
S	Volume of solid
L	Volume of liquid
ϕ	Volume fraction
$\phi_{\triangle Gmin}$	Volume fraction at which the minimum in the free energy is reached
L_t	Volume of the liquid layer at the transition time
ϕ_{A}	Volume fraction of polymer A
ϕ_{B}	Volume fraction of polymer B
ϕ_{PMMA}	Volume fraction of Poly(methyl methacrylate)
ϕ_{PS}	Volume fraction of Polystyrene

ϕ_{to}	Volume fraction of Toluene
ϕ_s	Volume fraction of solvent
κ	Weber number
T_w	Wetting temperature
NG	**N**ucleation and **G**rowth

Chapter 1

Aims and motivations

Polymer coating is the deposition of polymer material on a substrate. The many applications of polymer films include protective and anti-reflection coatings, films for medical, microelectronic and organic electronic devices. There are many ways to make a polymer film; each of them a gives different film thickness, uniformities and morphologies. The simplest deposition technique is drop casting; a polymer solution is deposited on a substrate and a film is obtained once the solvent has completely evaporated. In spite of its simplicity, drop casting is not widely used in industry as the uniformity of the film obtained is poor. Although the thickness of the film can be adjusted by controlling the concentration of the solution, it is difficult to achieve fine adjustments. Moreover the uniformity and homogeneity of the films diminish as the coated area increases.

FIGURE 1.1: Diagram of drop casting

Dip coating is a deposition technique where the substrate is dipped in a polymer solution then withdrawn at a controlled speed. The thickness of the film can be controlled by adjusting the withdrawal speed and by adjusting the concentration of the polymer. The films obtained with this technique are fairly uniform and thin. However the process is time consuming and the two sides of the substrate get coated, even when this is unnecessary.

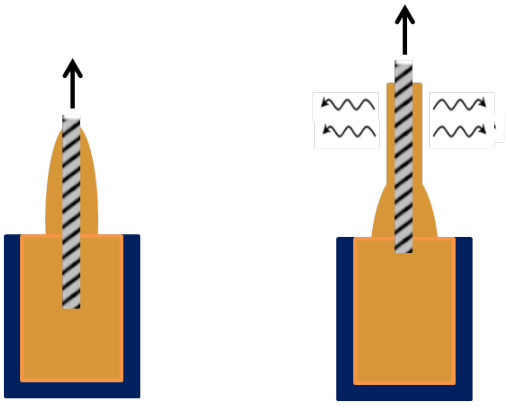

FIGURE 1.2: Diagram of dip coating

Another coating method is spray coating; as the name suggests a solution is sprayed on a substrate, a film is obtained once the solvent has evaporated. The thickness of the film can be adjusted by changing the nozzle and the concentration of the solution. The most important drawback with this technique is the poor uniformity of the films.

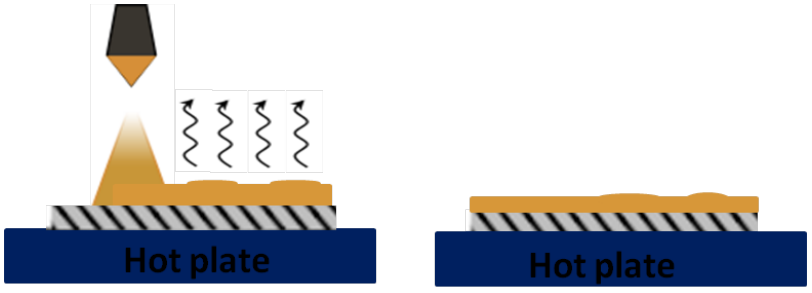

FIGURE 1.3: Diagram of spray coating

Spin coating is widely used due to its simplicity and the quality of the film obtained; a polymer solution is deposited on a substrate which is accelerated at spin speeds ranging between 1000 to 10 000 rpm. The solution spreads due to centrifugal forces. The cast solution can be a single component polymer solution or a multi-component solution. There are four stages involved in making a polymer film; the first one is the deposition of the solution on the substrate. The solution can be deposited via static deposition or

dynamic deposition. During static deposition the substrate is immobile and the solution deposited at the center of the substrate. Dynamic deposition consist of rotating the substrate while the solution is deposited. Dynamic deposition is required when coating large areas or when the substrate has a low wettability. This ensures that the solution is evenly spread on the substrate otherwise there may be uncovered areas. To ensure that the solution is free of non-dissolved polymers or dust that might lead to flaws on the film, the solution can be filtered prior to deposition. In the second stage the substrate is accelerated to its final thickness, here spiral vortices may exist in the film due to the inertial force endured by the top of the film as the lower layer of the fluid rotates. Eventually the fluid rotates at the same speed as the substrate. The duration of the acceleration phase depends on the ramp up speed of the spin coater. In the third stage the substrate and the fluid rotate at the same spin speed and the film thins gradually due to radial outflow. In this stage the centrifugal forces dominate the process; the film thins rapidly. Looking at the film very closely one can observe the changes in colour starting from the centre of the wafer and moving to the edge of the substrate. In the fourth stage the radial outflow due to the centrifugal forces is negligible and, the thinning rate is governed by the solvent evaporation rate.

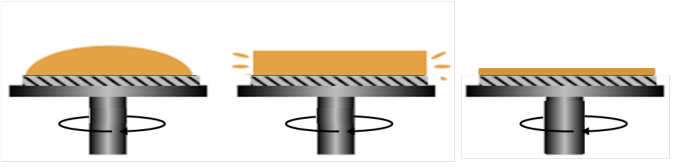

FIGURE 1.4: Diagram of spin coating

The biggest challenge faced with spin coating is the control of the dry film thickness and its morphology. Numerous groups have investigated which factors determine the final thickness [1–3]. With the aim to predict the thickness of the dry film Emslie, Bonner and Peck (EBP) [1], studied the dynamics of spin coating. They proposed a model to describe the rate of thinning of a non-evaporative liquid. According to their model the thickness of the film depends on the spin speed, the viscosity, the density of the solution, and the uniformity of the film is independent of the initial thickness profile. The non-uniformity of the film is due to the non-uniform solvent evaporation rate over the film. It was shown that static dispense allows better uniformity, which increases as the concentration of the solution decreases. The most challenging defect to eliminate in spin coated films is the formation of radial ridges called striations; which are caused by the non uniform evaporation rate [4, 5].

Despite the numerous polymers in existence, scientists still seek to combine desirable properties from several polymers by creating new blends. More often than not polymers are immiscible due to the low gain in entropy upon mixing. Spin coating can be used to make films of immiscible polymers. In this case the solution deposited on the substrate is a mixture of two polymers dissolved in a common solvent. This is exploited in polymer based electronic devices, where the mixing of polymers with different electron affinities enables to the production of solar cells or light emitting devices. Depending on the application, one might desire a multi-layered structure or phase separated structure. For organic solar cells a phase-separated network with a length scale of 10 nm is necessary to optimize the separation of the bounded electron and electron hole. Due to the enormous potential of plastic electronics, phase separation in polymer films has received considerable research interest in the last decades. Unlike phase separation in polymer films, phase separation in bulk polymer solutions is well understood. The Flory-Huggins theory enables us to calculate the free energy of mixing which can then be used to determine the proportions in which two polymers will be miscible. At a given pressure and temperature the free energy of mixing depends on the volume fraction of all the components, the interaction between the components and the molecular weights of the polymers. The interaction parameter χ quantifies the affinity between the two components, it depends on the molecular weight, the temperature and the concentration of the solution. Figure 1.5 shows the dependence of the various parameters involved in the formation of spin coating. The parameters that govern the free energy in spin coated films are shown in blue, those that govern the dynamics are shown in yellow and those that influence both process are shown in green. In Figure 1.5 A $\rightarrow$ B, mean that B depends on A. The spin speed does not depend on any parameter, however it control the evaporation rate and the change in the kinematic viscosity $\nu(t)$. When ω increases the films thin faster because the radial out flow increases. The thinning rates is inversely proportional to the kinematic viscosity, therefore, higher the kinematic viscosity lower will be the radial outflow. The viscosity of the polymer solution and therefore it concentration significantly affect the morphology of the film. Films coated from low polymer concentration solutions are smooth, those coated from highly concentrated solutions are laterally separated [6]. The evaporation rate is proportional to the square root of the spin speed and depends on the flow above the film and on the speed at which the top layer of the film is supplied with solvent (which depends on the diffusion). Bornside *et al.* [7] showed that the non uniform solvent evaporation is due to the

turbulent air flow above the film, the authors suggested that coating in the presence of an inert gas or solvent vapour will reduce the turbulent flow and give rise to better uniformities. It was also shown that smoother films are obtained when casting from solvents with low volatility [8].

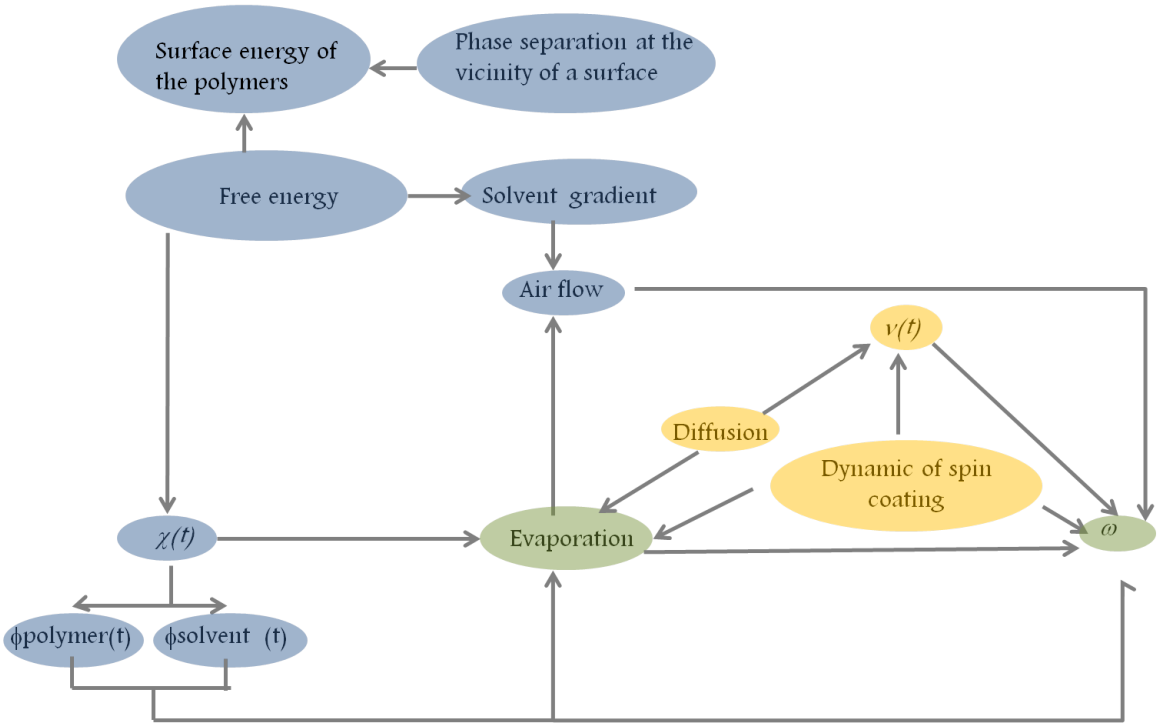

FIGURE 1.5: Dependency diagram for phase separation, uniformity and dynamics of spin coated films, at a given temperature and vapour pressure. A → B, mean that B depends on A. ω is the spin speed, $\nu(t)$ is the kinematic viscosity wich is equal to the ratio of the viscosity over the density, $\chi(t)$ is the intercation parameter and ϕ is the volume fraction.

Figure 1.6 shows the phase diagram of a bulk ternary solution made of a two polymers and one solvent. The descending arrow show the path taken during the spin coating of a ternary solution with an equal amount of polymer. The system is quenched from the region where the mixture is miscible to the region where it is not miscible. During spin coating, the quench depth depends on the speed at which the solvent depletes from the film. Note that Figure 1.5 show that the interaction parameters and the volume fractions of the components are time dependent, this dependency is a consequence of the solvent evaporation. This is where the challenge lays when it's come to studying the thermodynamic of polymer film during spin coating.

In 2005, *in-situ* light scattering technique was used for first the time to monitor the evolution of the length scale in spin coated films of polystyrene (PS) and poly(methyl

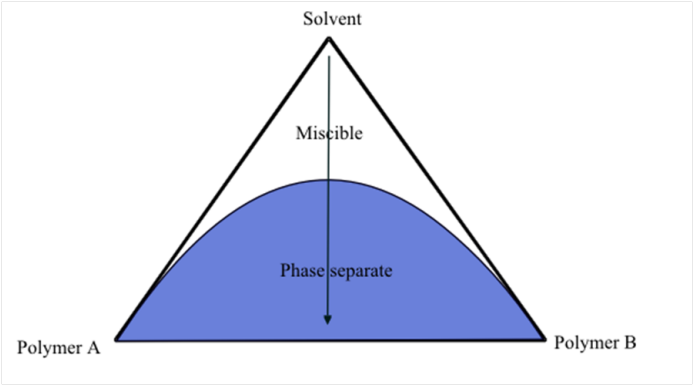

FIGURE 1.6: Diagram of the phase diagram of a ternary mixture, the region where the mixture is miscible is colored in white and the region where it is not miscisble is coloured in blue. The arrow shows the path borrowed by the ternary systeme during spin coating.

methacrylate) (PMMA) [9] . The scattering data showed that there are two important times during coating: the time at which the instabilities in the films start and the time at which a dominant length scale appears. Further research showed that phase separation in spin coated films of PS and PMMA occurs via a bilayer structure which breaks due to the evaporation rate gradient over the surface. The non uniform evaporation rate created a concentration gradient as well as a surface tension gradient, which create a flow from the regions of low surface tension to the regions of high surface tension. This motion creates convection cells, called Marangoni cells. Mokarian-Tabari *et al.* later showed that bilayer structure could be obtained when coating in presence of solvent vapour, the uniformity of the film was also shown to improve with the solvent vapour pressure.

An ideal method to study phase separation in spin coated films would be to combine the specular and off-specular techniques with a model that would describe the free energy in the film during coating. The free energy of a polymer mixture exposed to a surface is rather complex; as show Figure 1.5, the free energy of a spin coated film also depends on the interactions between the substrate and the polymers and the surface energy of the two polymers. In fact, it was shown experimentally and theoretically that the presence of a surface breaks the isotropic geometry of bulk phase separation and could even lead to the formation of layers [10]. The polymer with the lower surface energy is segregated at the top of the film, this enables to lower the free energy of the system, however there is a cost to pay for having a composition gradient. By neglecting the surface term and the concentration gradient term in the free energy, the Flory-Huggins theory

could be used to study the thermodynamics of spin coated film provided that we can estimate the solvent and the polymer volume fraction during the process. Figure 1.5 shows the necessity of a model which describes the dynamics in order to estimate the time dependency of the solvent and the polymer volume fractions during the coating.

The EBP model describes the thinning rate of a non-volatile solution, as a consequence this model is not relevant when studying the spin coating of a polymer solution. Meyerhofer [2] revisited this model by including a constant evaporation rate and taking into account changes in viscosity. He showed that the process has two time scales. The initial stage lasts a couple of milliseconds; in this phase the film thins due to the radial outflow caused by the centrifugal forces. Later the process is dominated by the solvent evaporation. Other models include parameters such as the solvent gradient in the film, the rheology of the fluid and the solvent vapour pressure above the film. For many years these models were not compared to the experimental results due to the lack of methods to monitor the changes in the film thickness. Horowitz was the first to use interferometry to follow the thinning of a spin coated film. Mokarian-Tabari *et al.* [11] and Birnie *et al.* [12, 13] used the same technique to study the thinning rate of a solid free layer. Birnie [12] applied a linear regression on the data to calculate the evaporation rate. Mokarian-Tabari *et al.* modelled the change in thickness by solving numerically the Meryerhofer equation. Later Birnie studied the thinning of a PMMA film dissolved in Tetrahydrofuran (THF). Here again linear regression was used to estimated the evaporation rate, but no direct fitting of the thickness profile was performed.

This project aspires to give a better understanding of the phase separation in spin coated films by using the dynamics to quantify the parameters that govern it. There are three results chapters. In chapter 4 we focus on the modelling of the thickness profiles of liquid layers and polymer films. The changes in thickness were monitored using *in-situ* specular reflectivity. The data was fitted with the Meyerhofer model, a model proposed by Reisfeld, Bankoff and Davis (RBD) [3] and a semi-empirical model proposed here. The last two models aim to give a better description of the early stage by including correction terms to account for the inertial forces which cause a gradient normal to the radial velocity within the film. We study the quality of the fits as a function of the spin speed and the shearing forces experienced by the top of the film. We show that the Meyerhofer and the RBD model are suited to describe the thinning of liquids which experience no inertial forces and liquids which experience weak inertial forces. An

excellent agreement is obtained between the semi-empirical model for the thinning of liquid films and polymer films. The semi-empirical model gives rise to new possibilities such as the modelling of the solvent volume fraction, the polymer volume fraction and the viscosity as a function of time.

In chapter 5 we investigate the phase separation of films coated from solutions with different toluene volume fractions and an equal amount of PS and PMMA. The length scale of the phase separation increases with the polymer concentration. The thinning rate of the film decreases when the polymer concentration increases. We use off-specular scattering to identify the cloud point and the onset of the interfacial instabilities during the coating. Using the Flory-Huggins theory alongside the semi-empirical model we calculate the free energy during coating and the solvent volume fraction in the film as it thins. The data reveal that the cloud point during spin coating does not differ from that in the bulk. A minimum in the free energy is observed at the onset of interfacial instabilities. Although the onset of the interfacial instabilities is delayed when the polymer concentration increases, these instabilities start when the solvent content in the film reaches a specific volume fraction. We show that the a change in the solvent concentration changes the morphology of the films and the kinetics of the phase separation rate but the thermodynamics remain unchanged.

In chapter 6 we investigate the influence of the interaction parameters on the morphology of films coated with different polymer concentrations, by reducing the temperature during coating. The off-specular data and the microscopic images suggest that lowering the temperature and the concentration promoted the formation of bilayer structures. The analysis of the thinning rate shows that the evaporation rate decreases with the temperature which suggests that films experience weaker Marangoni instabilities. As the interaction parameters increase due to the lowering of the temperature, the bilayer structure is promoted, probably due to a reduced contact between the two polymers as well as the weak Marangoni instabilities.

Chapter 2

Theory

In this chapter the reader will find all the theory necessary to understand the work done in this project. There are fours sections; in section 2.1 we review the thermodynamics of bulk system, this is needed since the films are cast from bulk polymer solutions.We will at first review the conformation of single chain in polymer solutions. Then we will review the Flory-Huggins theory which is a mathematical model used to describe the thermodynamics of polymer solutions. Since in this project the films are cast from ternary solutions of PS, PMMA and toluene, we choose to summarize the work done on the thermodynamics of this blend in its bulk phase. Phase separation in spin coated films differs from that of bulk solutions because of the proximity of the surface. In section 2.2 we revise the parameters and phenomena which govern the phase separation in thin films: surface tension, surface segregation, surface directed spinodal decomposition and the Marangoni effect. We finish this section with a literature review on phase separation near a surface. section 2.3 deals with the modelling of spin coating. In this section we will first describe the different stages of spin coating. We will then review the EBP model. The Meyerhofer and Reisfeld model will also be examined as they will be used to fit the experimental data. A complete understanding of spin coating requires an understanding of rheology and viscosity of polymer solution during the coating. This will be followed by a literature review on the spin coating of Newtonian and Non-Newtonian fluid and literature review on the dynamics of spin coating. Since we will be studying the phase separation and the dynamics of spin coating using *in situ* techniques, in section 2.4 we will cover the past work done on spin coating using *in-situ* methods .

2.1 Thermodynamics of bulk polymer blends

2.1.1 Chain conformation

2.1.1.1 Bonds conformation

A polymer chain consists of a main chain connected to side groups. Most polymers only have single bonds on their backbone. Unlike double bonds, single bonds have torsional freedom which leads to different configurations, each of which is associated with an energy. Figure 2.1 show a diagram of the different conformation of three bonds connecting four carbons (C_1, C_2, C_3 and C_4) in the backbone of a polyethylene chain. If the three bonds are in a same plane and in the configuration showed in Figure 2.1 (a), the bond between $C_2$and C_3 is said to be in a trans-conformation. If the three bonds are not in the same plane, the bond connecting C_2 and C_3 is said to be in a gauche configuration. There are two possible gauche conformations gauche (+) and gauche (-); these are better illustrated with the projection see Figure 2.1 (d) and (f). On the projection of the trans conformation (Figure 2.1 (b)) one can see that the distance between C_4 and C_1 is maximised therefore minimizing the total energy. In order to minimize its energy a polyethylene chain should have all the bonds in the trans configuration and in this case the end-end distance of the chain is maximised. Due to the large number of bonds in a polymer chain, the conformation of a chain cannot be described by reporting the conformation of every bond. The conformation of a polymer chain can only be described by statistical methods. The bond conformation affects the distance between the ends of the polymer chain; the end-end distance is therefore used to describe the configuration of a polymer chain.

2.1.1.2 Freely-jointed chain

In order to developed a statistical theory for polymer chains several models have been proposed. The freely jointed chain also called the ideal chain is the simplest model. It relies on four assumptions

- A polymer chain is regarded as a chain of points connected by n_b bonds of equal length l

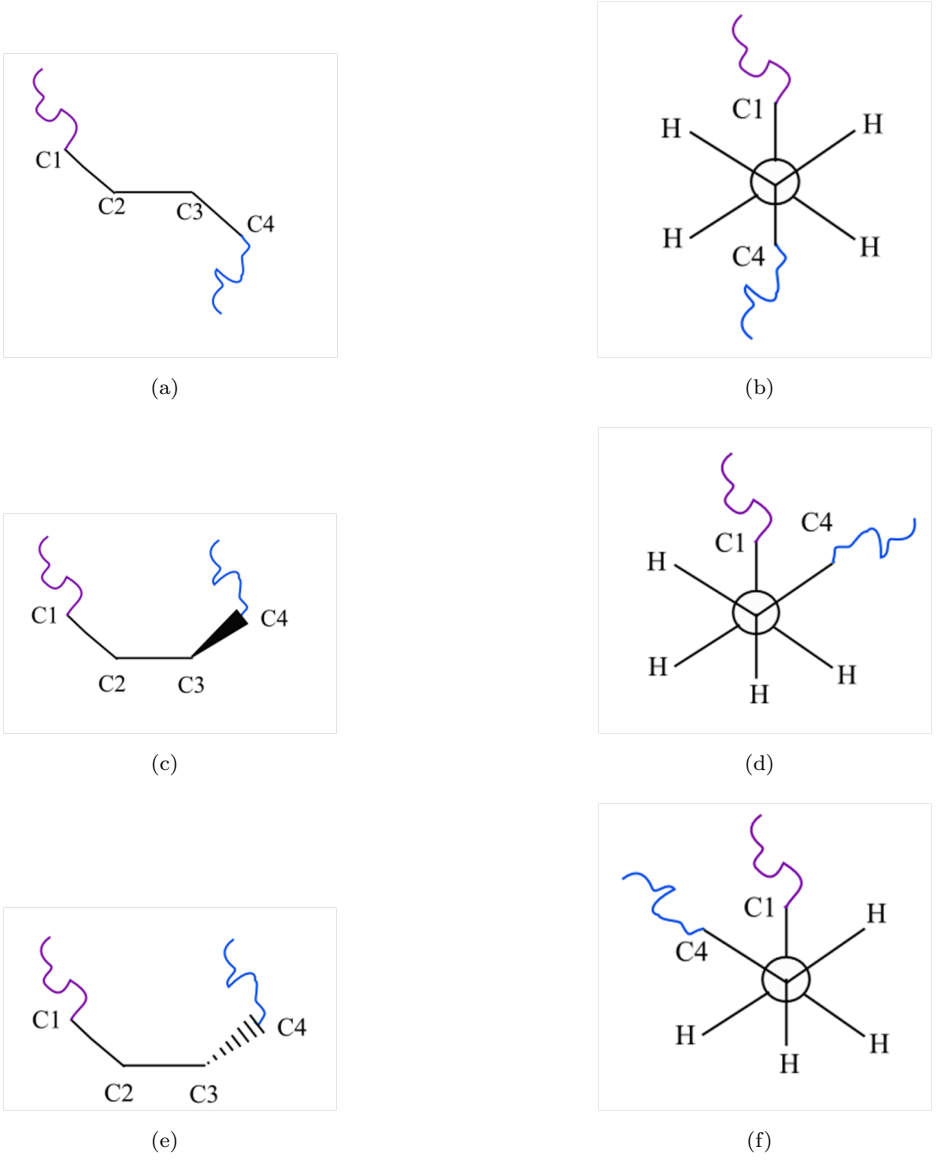

FIGURE 2.1: Diagram of the different conformations of a bond in a polyethylene chain. (a), (c) and (d) show a section of the polyethylene chain when the bonds that connect C_2 and C_3 is in a trans, gauche(-) and gauche(+) conformation. (b), (b) and (e) show the the projection of the trans, gauche (-) and gauche (+) conformation

- There is no restriction on the bond angles (the direction of the bonds are not correlated).
- No energy is required to change the torsional angle
- The interactions between monomers that are far apart in the chain are neglected

Figure 2.2 shows the diagram of a freely jointed chain of 10 monomers. The end-end distance of a chain is calculated by adding all the bond vectors, $\vec{r_n}$. The end-end distance

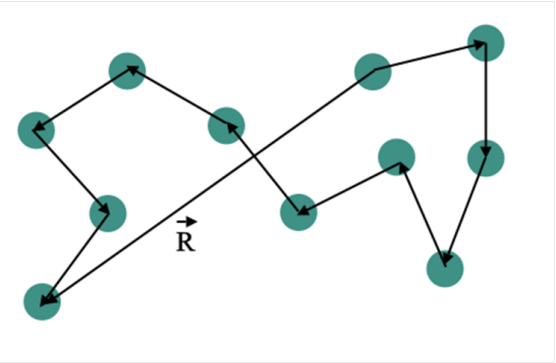

FIGURE 2.2: Diagram of a polymer chain with 10 bonds. The end-end distance is equal to the sum of all the bond vectors

is expressed as

$$\vec{R_n} = \sum_{n=0}^{n=1} \vec{r_n} \tag{2.1}$$

Due to the isotropic distribution of the bond directions, the end-end distance is equal to zero. The mean-square average is used to describe the configuration of polymer chains.

$$< \vec{R_n^2} >=< \vec{R_n} \cdot \vec{R_n} >= \sum_{i=0}^{n} \sum_{j=0}^{n} < \vec{r_i} \cdot \vec{r_j} >= l^2 \sum_{i=0}^{n} \sum_{j=0}^{n} < \cos\theta_{ij} > \tag{2.2}$$

It is assumed that there is no correlation between the direction of the bonds; the mean square average end-end distance is equal to

$$< \vec{R_n^2} >= n_b l^2 \tag{2.3}$$

2.1.1.3 Equivalent freely-jointed chain

The equivalent freely-jointed chain accounts for the interactions between the monomers. It also assumes that all the bonds are equal to an effective length a called the Kuhn length. The equivalent freely-jointed chain has the same mean square average end-end distance and the same maximum end-end distance as the freely-jointed chain such that it has

$$N = \frac{R_{max}^2}{C_\infty n_b l^2} \tag{2.4}$$

equivalents bonds of length equal

$$a = \frac{C_\infty n_b l^2}{R_{max}}. \tag{2.5}$$

In Equation 2.5, C_∞ is the characteristic ratio which represents the correlations between the different bonds of the polymer chain due to the steric hindrance and the restricted bond angles. The conformation of a polymer chain can also be described by the radius of gyration which is the average square distance between the monomers and the centre of mass of the polymer chain. The radius of gyration is related to the end-end distance by the following equation

$$< R_g^2 >= \frac{< \vec{R_n^2} >}{6}. \tag{2.6}$$

This is a moment, and it represents the fact that the mass of the chain is distributed nearer to the centre of the chain than to the edges.

2.1.1.4 Conformation in polymer solutions

The conformation that a polymer chain takes in the presence of a solvent depends on the interaction between the monomers and the solvent molecules. The interaction energy quantifies the energy cost to bring two monomers within a distance r. The interaction energy always contains a repulsive hard-sphere barrier due to the steric repulsion between the two monomers (the volume inaccessible to a monomer as a result of the presence of another monomer). The interaction energy also depends on the interaction between the monomer and the solvent molecule.

- If the solvent and the monomer are chemically identical the interaction energy will contain only the hard-sphere repulsion, in this special case the solvent is called athermal
- If monomer-monomer contacts are favoured compared to the contact with the solvent molecule, the interaction energy will have an attractive well.
- If contacts between monomers and solvent molecules are favoured, the interaction energy will have extra repulsions.

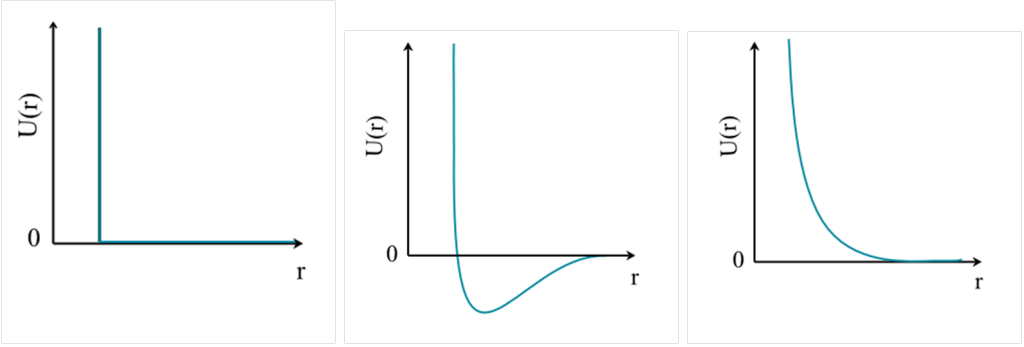

(a) (b) (c)

FIGURE 2.3: Interaction energy describing the energy cost required to bring two monomer within a distance r. (a) Plot of interaction energy as a function of the distance in a polymer solution where only the hard-sphere repulsion exists. (b) Interaction energy as a function of distance between the monomer with an attractive well (monomer-monomer contact favoured). (c) Interaction energy as a function of the distance between monomer with extra repulsion (monomer-solvent contact favoured)

The interaction energies which illustrates these cases are plotted in Figure 2.3. The volume inaccessible to a monomer due to the interaction energy is called the excluded volume and it is expressed as

$$v = (1 - 2\chi)a^3, \tag{2.7}$$

with χ being the interaction parameter of the solvent polymer system. When $\chi < 1/2$, $v > 0$ the interaction energy is dominated by the repulsive interaction. The monomer-solvent contacts are favoured and the polymer chains swell. When $\chi > 1/2$,$v < 0$ the interaction energy is dominated by the attractive interactions. The contacts between the monomers are favoured and the polymer chains collapse. When $\chi = 1/2$,$v = 0$ the repulsive forces and attractive forces cancel out; in this case the solvent is called theta solvent and the chains behave like ideal chains. When $\chi = 0$,$v = a^3$ the interaction energy only contains hard-sphere repulsion. In this case the solvent is called athermal and it is a particularly good solvent. Table 2.1 reports the end-end distance of a polymer chain in a solution as a function of the solvent quality. Note that the end-end distance decreases when the quality of the solvent deteriorates.

2.1.2 Flory-Huggins theory

Irrespective of the numerous pre-existing polymers, industries still seek to combine desirable properties from several polymers by creating new blends. Two polymers A

Solvent quality	Polymer size
Good solvent	$\sqrt{<\vec{R_n^2}>} \approx N^{0.6}$
Poor solvent	$\sqrt{<\vec{R_n^2}>} \approx N^{0.33}$
Thetha solvent	$\sqrt{<\vec{R_n^2}>} \approx N^{0.5}$
Athermal solvent	$\sqrt{<\vec{R_n^2}>} \approx N^{0.6}$

TABLE 2.1: Table reporting the dimension of polymer chain as a function of the solvent quality

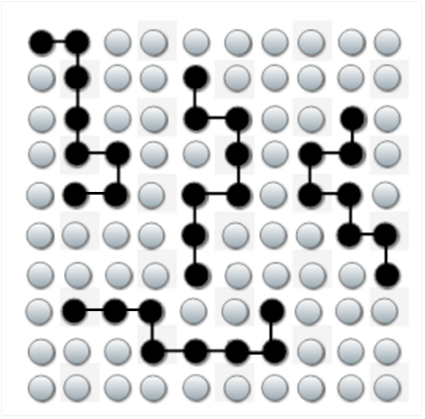

FIGURE 2.4: lattice for a polymer-solvent mixture. Black sites are the polymer monomers, grey sites are the solvent molecules

and B will only mix if the energy of mixing, $\triangle G_{\text{mix}}$, is negative. $\triangle G_{\text{mix}}$ is equal to the free energy of the mixture, $G_{\text{A+B}}$ subtracted from the free energy of the two species G_{A} and G_{B}. The free energy of mixing can be expressed as a function of the entropy of mixing and the enthalpy of mixing as follows

$$\triangle G_{\text{mix}} = G_{\text{A+B}} - G_{\text{A}} - G_{\text{B}} = \triangle H_{\text{mix}} - T\triangle S_{\text{mix}}. \tag{2.8}$$

The Flory Huggins mean field theory uses the lattice chain model to calculate the entropy and the enthalpy upon mixing. Let us consider the mixing of a polymer A with a degree of polymerization N_{A} with a solvent. In this model a polymer chain is assimilated to N_{A} beads linked by $N_{\text{A}} - 1$ strings. The monomers and the solvent molecules are randomly disposed on the lattice until the lattice is full. We note ϕ_{A} and ϕ_{S} the volume fraction of polymer A and the volume fraction of the solvent. $\triangle S_{\text{mix}}$ is calculated by counting the different arrangements possible for the polymer chain A and the polymer chain B in the lattice and is given by

$$\triangle S_{\text{mix}} = -k_{\text{B}}(\frac{\phi_{\text{A}}}{N_{\text{A}}} \ln \phi_{\text{A}} + \phi_{\text{S}} \ln \phi_{\text{S}}). \tag{2.9}$$

Note that the number of arrangements of the n_{p} polymer chains is reduced by N_{A} to represent the fact that the monomers in one chain cannot move independently. $\triangle H_{\mathrm{mix}}$ takes the interaction between the neighbouring sites in to account and is equal to

$$\triangle H_{\mathrm{mix}} = k_{\mathrm{B}} T \chi_{\mathrm{AS}} \phi_{\mathrm{A}} \phi_{\mathrm{S}}. \tag{2.10}$$

In this equation χ_{AS} is the Flory-Huggins interaction parameter which is an empirical and dimensionless quantity and is expressed as

$$\frac{x}{2} \frac{2\varepsilon_{\mathrm{AS}} - \varepsilon_{\mathrm{AA}} - \epsilon_{\mathrm{SS}}}{k_{\mathrm{B}} T}, \tag{2.11}$$

where ε_{AA} is the energy of interaction between two neighbouring monomers A, ε_{SS} is the energy of interaction between two neighbouring solvent molecules, $\varepsilon_{\mathrm{AS}}$ is the energy of interaction between a solvent molecule and a polymer monomer and x is the number of nearest neighbour in the lattice ($x = 4$ in a 2D lattice and $x = 6$ in a 3D lattice). χ_{AS} represents the change in energy when a monomer A is removed from an environment where it is only surrounded by monomers A; to an environment where it is only surrounded by solvent molecules S. Positive Flory-Huggins parameters are not desirable as they symbolise the repulsive interaction between the polymer monomers and the solvent molecule. Theoretically χ depends on the temperature via the following equation

$$\chi = A + \frac{B}{T}, \tag{2.12}$$

where A and B are parameters referred as the entropic part and the enthalpy part respectively. Experimental measurements have shown that χ also depends on the degree of polymerization. Substituting Equation 5.3 and 2.39 in 2.8 yields

$$\frac{\triangle G_{\mathrm{mix}}(\phi_{\mathrm{A}} \phi_{\mathrm{B}})}{k_{\mathrm{B}} T} = \frac{\phi_{\mathrm{A}}}{N_{\mathrm{A}}} \ln \phi_{\mathrm{A}} + \phi_{\mathrm{S}} \ln \phi_{\mathrm{S}} + \chi_{\mathrm{AS}} \phi_{\mathrm{A}} \phi_{\mathrm{S}}. \tag{2.13}$$

The free energy of mixing of polymer A and a polymer B, with degree of polymerisation N_{A} and N_{B}, is expressed as

$$\frac{\triangle G_{mix}(\phi_{\mathrm{A}} \phi_{\mathrm{B}})}{k_{\mathrm{B}} T} = \frac{\phi_{\mathrm{A}}}{N_{\mathrm{A}}} \ln \phi_{\mathrm{A}} + \frac{\phi_{\mathrm{B}}}{N_{\mathrm{B}}} \ln \phi_{\mathrm{B}} + \chi_{\mathrm{AB}} \phi_{\mathrm{A}} \phi_{\mathrm{B}} \tag{2.14}$$

In the case of a ternary mixture of a polymer A, a polymer B and a solvent S, the free energy of mixing is equal to:

$$\begin{aligned}\frac{\triangle G_{mix}(\phi_{\mathrm{A}},\phi_{\mathrm{B}},\phi_{\mathrm{S}})}{k_{\mathrm{B}}T} &= \frac{\phi_{\mathrm{A}}}{N_{\mathrm{A}}}\ln\phi_{\mathrm{A}}+\frac{\phi_{\mathrm{B}}}{N_{\mathrm{B}}}\ln\phi_{\mathrm{B}}+\phi_{\mathrm{S}}\ln\phi_{\mathrm{S}} \\ &\quad +\chi_{\mathrm{AB}}\phi_{\mathrm{A}}\phi_{\mathrm{B}}+\chi_{\mathrm{AS}}\phi_{\mathrm{A}}\phi_{\mathrm{S}}+\chi_{\mathrm{BS}}\phi_{\mathrm{B}}\phi_{\mathrm{S}} \end{aligned} \tag{2.15}$$

The entropy of mixing is always negative and therefore always promotes mixing. However N_{A} and N_{B} tend to be very large resulting in low entropy of mixing. Consequently more often than not polymers are immiscible. The most efficient way to obtain polymer mixture is to dissolve them in a common solvent or by heating them above their melting point

2.1.2.1 Stability and phase diagram

Phase separation can be induced via polymerization, temperature quenching or solvent quenching. During solvent quenching, the solvent evaporates and the repulsive interactions between the two polymers increase until the system phase separates. Let us consider a symmetric binary mixture of polymer A and B with an initial volume fraction $\phi_{\mathrm{A}}=\phi$ and $\phi_{\mathrm{B}}=1-\phi$ and $N_{\mathrm{A}}=N_{\mathrm{B}}=N$. Using Equation 2.14 we plot the free energy of mixing as a function of ϕ for different values of the interactions parameters (see Figure 2.5 (a)). This graph shows that the mixture undergoes a transition as the χ increases. At a low value of χ, $\triangle G_{\mathrm{mix}}$ has one single minimum at $\phi=0.5$ and the mixture is miscible for all the composition. As χ increases we see two local minima at ϕ_α and ϕ_β with a maximum at $\phi=0.5$ (see Figure 2.5 (b)). In this case the total energy is minimised when the mixture phase separates in two phases: phase α with a volume V_α and a volume fraction of polymer A equal to ϕ_α and a phase β with a volume V_β and a fraction of polymer A equal to ϕ_β.

In the χN vs ϕ plot the binodal line is the locus of points where

$$\left(\frac{dG_{\mathrm{mix}}}{d\phi}\right)_{\phi=\phi_\alpha}=\left(\frac{dG_{\mathrm{mix}}}{d\phi}\right)_{\phi=\phi_\beta} \tag{2.16}$$

and represents the limit at which a homogeneous polymer mixture will phase separate. Because we have a symmetric mixture $\left(\frac{dG_{\mathrm{mix}}}{d\phi}\right)_{\phi=\phi_\alpha}=\left(\frac{dG_{\mathrm{mix}}}{d\phi}\right)_{\phi=\phi_\beta}=0$. This can be seen graphically in Figure 2.5 where the tangent at the two local minima are horizontal.

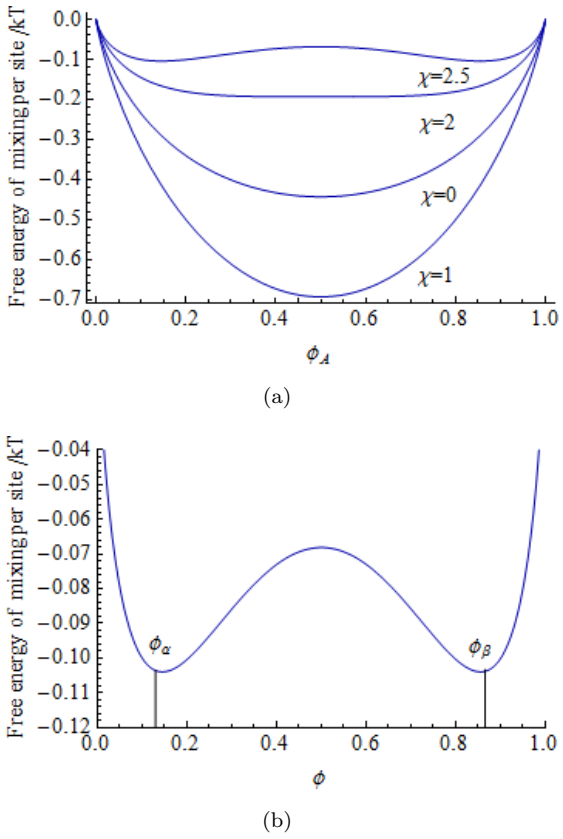

FIGURE 2.5: (a) Free energy of mixing for a symmetric binary mixture for various value for χ. (b) Free energy of mixing for a symmetric binary mixture for various value for $\chi = 2.5$

Within the two phase region a composition can either be stable or unstable with respect to a small composition fluctuation. The spinodal line is the locus of points satisfying the following equation

$$\frac{d^2 G_{\text{mix}}}{d\phi^2} = 0. \tag{2.17}$$

The spinodal line sets the limit between the stable and metastable compositions within the two phase region. The intersection of the spinodal and binodal lines is the critical point and is calculated by solving

$$\frac{d^3 G_{\text{mix}}}{d^3\phi} = 0. \tag{2.18}$$

Solving Equation 2.16, Equation 2.17 and Equation 2.18 for χ allows to plot the phase diagram in the χ and composition space (see Figure 2.6). Below the binodal line the mixture is miscible. Between the binodal line and the spinodal line the mixture is said to be unstable. Above the spinodal line the mixture is phase separated. The

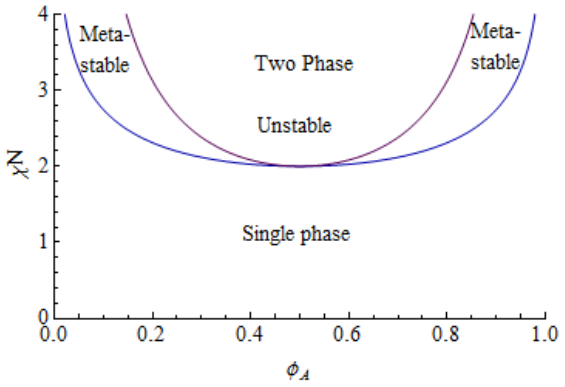

(a)

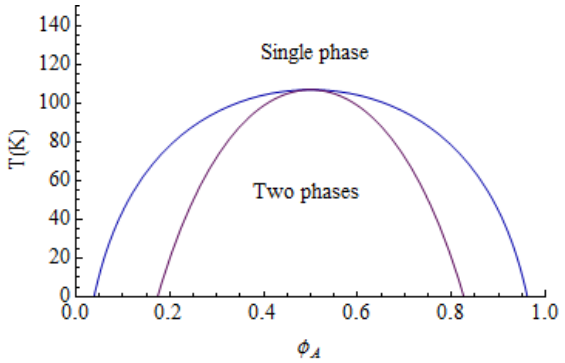

(b)

FIGURE 2.6: (a) phase diagram for a symmetric binary mixture. The binodal line is the blue curve and the spinodal line is purple. (b) Phase diagram for a binary mixture of hydrogenated polybutadiene (88 % vinyl) and deuterated polybutadienne (78% vinyl) for$N_{\mathrm{A}} = N_{\mathrm{B}} = 2000$. The binodal line is the blue curve and the spinodal line is purple

value of χ for which the mixture enter the two phase region is referred as the critical interaction parameter and note as χ_{c}. Equation 2.12 is used to calculate the binodal and the spinodal curve in the temperature and composition space. Here we plot the phase diagram for a binary mixture of hydrogenated polybutadiene (88 % vinyl) and deuterated polybutadienne (78% vinyl) for$N_{\mathrm{A}} = N_{\mathrm{B}} = 2000$ with $\chi = -9.2010^{-4} + \frac{0.0722}{T}$. The value of T for which the mixture enter the two phase region is referred as the critical temperature and note as T_{c}. Note that in the example illustrated T_{c} corresponds to the maximum of the binodal line. This is referred to as upper critical solution temperature (UCTS). If the critical temperature corresponds with the minimum on the binodal line we would speak of lower critical solution temperature (LCST).

Experimentally, phase separation is determined by observing the turbidity of a polymer solution. As the blend polymer phase separates the microscopic heterogeneity in the solution leads to light scattering and the solution becomes cloudy. The temperature at

which a mixture get cloudy is called the cloud point. The cloud point can be observed with the naked eye. For more precision, however, photodetectors are used to monitor the light transmitted through the polymer solution. In this experiment a solution is placed in a cuvette and a laser light is directed to the mixture at an angle of $90°C$. The mixture is first brought in to a single phase by heating then cooling slowly while recording the transmittance.

2.1.2.2 Mechanism of phase separation

Phase separation can occur via nucleation and growth (NG) or spinodal decomposition (SD) depending on whether the system is quenched in a metastable or unstable composition within the co-existence curve. The sign of mutual diffusion D_{mu} which describes the relative motion of polymer chains in the presence of a chemical composition gradient in a polymer mixture dictates the process through which phase separation will arise[46]. The mutual diffusion is given by

$$D_{\mathrm{mu}} = D_o(1-\phi)\frac{d^2G_{\mathrm{mix}}}{d\phi^2}. \tag{2.19}$$

In this expression D_o is always positive, therefore the sign of the D_{mu} is ordered by the sign of $\frac{d^2G_{\mathrm{mix}}}{d\phi^2}$. In the stable composition of the two phase region D_{mu} is positive; material moves from a high concentration phase to a low concentration phase. Phase separation occurs via NG. Only large composition fluctuations will lead to phase separation. The Gibbs theory on NG gives a good understanding of this process: small spherical clusters which can grow or reduce by one or several polymer chains are continuously formed and destroyed. The rate of growth of a cluster depends exponentially on Gibbs free energy, $\triangle G_r$, needed to create of cluster of radius r

$$\triangle G(r) = \frac{4}{3}\pi\triangle G_V r + 4\pi\sigma r^2, \tag{2.20}$$

in this equation $\triangle G_V$ is the Gibbs free energy change per unit of volume and is always negative and σ is the surface tension. The volume term is the amount of which the free energy is reduced when an embryo of radius r is created. The surface term is the increase in the free energy due to the creation of a new interface. The surface and volume term being of opposite signs compete with each other. It is only when the nucleus has reached

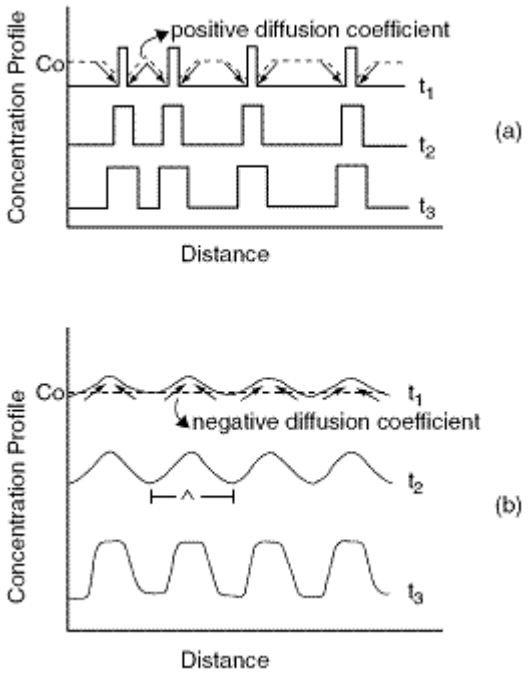

FIGURE 2.7: Illustration of the two mechanisms (a) nucleation and growth and(b) spinodal decomposition. In (a) the positive diffusion coefficient gives rise to the domain of growing size with a constant concentration. In (b) the negative diffusion coefficient leads spontaneous phase separation with a characteristic length scale. Taken from Introduction to Physical Polymer Science, S.H. Sperling, John Wiley & Sons (2005) 160, with permission from John Wiley & Sons.

critical radius r_C, or overcome an energy barrier corresponding to the maximum of the free energy, that growth will become spontaneous. In the metastable composition of the two phase region, D_{mu} is negative; material moves from a region of low concentration to a region of high concentration and small composition fluctuations will lead to a spontaneous phase separation through SD. Phase separation trough and SD is isotropic and is characterised by one length scale called the spinodal wavelength.

2.1.3 Free energy of mixing of a non-homogeneous system

The Flory-Huggins theory is based on the following assumptions:

- Incompressibility: A lattice point can only be occupied by one monomer and monomers A and B are of equal volume and no lattice point are vacant.
- There is no extra volume due to the repulsion between two monomers.

- It is assumed that a monomer is located in a lattice point, therefore ignoring the different configurations on a monomer scale which results in the reduction of the entropy of mixing.
- The Flory Huggins theory ignores the large concentration fluctuation in the vicinity of the critical point.

If none of these assumptions are valid, the volume per monomer of the two polymers is not equal. Concentration fluctuation affect the phase boundaries. The squared gradient theory aims to improve the Flory-Huggins theory by taking into account the spatial composition fluctuation through a square gradient term[14]. The expression for the free energy of mixing per site is given by

$$\triangle G = \int \triangle G_{\text{mix}}(\phi) + \kappa(\phi)(\nabla\phi)^2 dV. \tag{2.21}$$

Here $\triangle G_{\text{mix}}$ is the Flory Huggins energy of mixing, $\kappa(\phi)$ is the square gradient term which is the energy cost for having a the composition gradient. The expression for $\kappa(\phi)$ depends on the number of component in the mixture.

2.1.4 Glass transition

During spin coating, as the solvent evaporates and the viscosity increases the solution changes to a glass. The film becomes glassy at the glass transition temperature, which is usually referred to as T_{g}. Experimentally the glass transition is often determined by thermal analysis techniques but optical techniques can sometimes be used for thin film systems. The Flory-Fox equation expresses the glass transition of a mixture as a function of the glass transition temperature of the component and their concentration. It is expressed as

$$\frac{1}{T_g} = \frac{w_1}{T_{\text{g},1}} + \frac{w_2}{T_{\text{g},2}} \tag{2.22}$$

in which T_{g1} and T_{g2} refer to the glass transition of the two components and w_1 and w_1 are the corresponding weight fractions [15]. The process of creating a glass transition by supercooling is called vitrification. Figure 2.8 show a phase diagram in the temperature composition space and the the glass transition temperature. If the binodal and the glass transition curves intercept the point of interception is called the

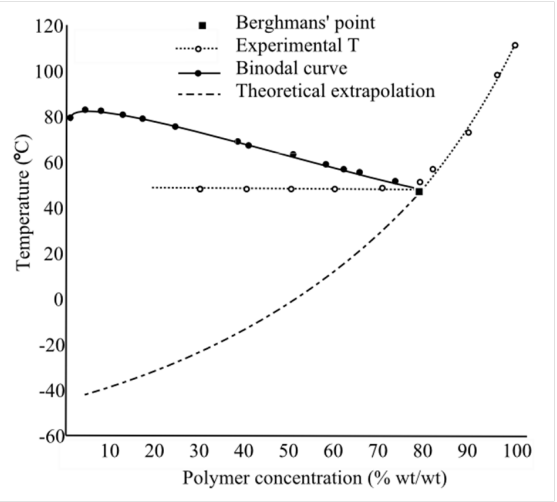

(a)

FIGURE 2.8: Experimental and theoretical glass transition for a mixture of PS and cyclohexane. The dot-dashed line is a theoretical prediction. The open circles are the experimental glass transitions and the dotted line is the fit to the data. The black circles are the cloud point measuments and the solid line is the fit to the binodal. The square dot is the Bergnmans point. Reprinted from R. M. Hikmet, S. Callister, and A. Keller, Polymer, **29**, 1378-1388, (1988) with permission from Elsevier

Berghmans point [16] (see Figure 2.8). The Berghmans point is particularly important in thermally-induced phase separation. If a polymer solvent mixture is quenched in the two phase region by decreasing the temperature, the polymer-rich phase will vitrify at the Berghmans temperature. This is illustrated in Figure 2.8, which compares the theoretical glass transition for a mixture of PS and cyclohexane to the experimental glass transition of the same mixture when during thermally induced phase separation. Above the Berghmans concentration, the experimental glass transition is in agreement with the theoretical predictions and they are both concentration dependent. Below the Berghmans concentration, the glass transition temperature is independent on the polymer concentration and is equal to the Berghmans temperature. Vitrification stops the ripening of the phase-separated domains and compositional changes i.e the composition in the polymer in the two phases is not equal to the polymer composition at the extremities of the tie lines [17]. Vitrification creates a new class of metastable composition. Although the system will vitrify at the Berghmans point, a wide range of morphologies can be obtained by changing the ratio of the components. If a mixture is quenched at the temperature below the Berghmans point by evaporative cooling, vitrification will take place when the polymer concentration intercepts the glass transition curve.

2.1.5 The ternary mixture PS, PMMA, and toluene

Due to the difficulties involved in studying ternary systems, the number of publications on polymer-polymer-solvent mixtures are limited. Ternary phase diagrams are tricky to represent since there are five variables involved: the volume fraction of the component A, ϕ_A , the volume fraction of component B, ϕ_B, the volume fraction of component C, ϕ_C, the temperature and the pressure. The phase diagram is a three dimensional plot. Figure 2.9 (a) shows the free energy of mixing for a ternary mixture. Since the mixture is partially miscible, there are two compositions for which the tangent plane to the free energy coincide.

The surfaces A′C′E′ and its projection ABCDE on the triangle base are binodal. In the same way the curves K′C′L′ and its projection KCL are spinodals. In Figure 2.9 (b), the loci of the binodal and spinodal at a constant pressure while temperature T changes give the binodal surface KLAC and the spinodal surface which is hatched. On Figure 2.9 (b), the plan TSX intercept the binodal surface on the cloud point curve. On Figure 2.9 (a) and (b), the points C and C′ are critical points and are also called plait points. In order to simplify this representation, it is common to represent the isothermal case i.e. the projection on the triangle base.

Lau *et al.* [18] measured $\chi_{\text{ps/pmma}}$, $\chi_{\text{ps/to}}$ and $\chi_{\text{ps/pmma}}$. Solutions of PS and PMMA dissolved in toluene were left to phase separate, gel permeation chromatography was used to identify the composition of the two phases. The top phase was always richer in PS whereas the bottom phase was richer in PMMA. He drew several conclusions from this study. The $\chi_{\text{ps/pmma}}$ increases as the molecular weight of the two polymers increases. He explained this by the fact that low molecular weight lead to higher mobility of the polymer chains. At a given value of the molecular weight of the two polymers the $\chi_{\text{ps/pmma}}$ decreases with increasing polymer concentration. This is counter intuitive but similar results were also reported by Berek *et al* [19]. Looking at the similitude between his work and Narasimhan *et al* [20], Lau explain this by the fact that the two polymers are competing for space in a limited volume and since they are intrinsically incompatible the random coils of the two polymers tend to withdraw from each other. For all the mixtures studied $\chi_{\text{ps/to}}$ was lower than $\chi_{\text{pmma/to}}$. This is in agreement with the experimental observation; toluene is a better solvent for PS than PMMA. Later; Lau *et al.* [21] plotted the phase diagrams of the same mixtures and reported the $\chi_{\text{ps/pmma}}$ at

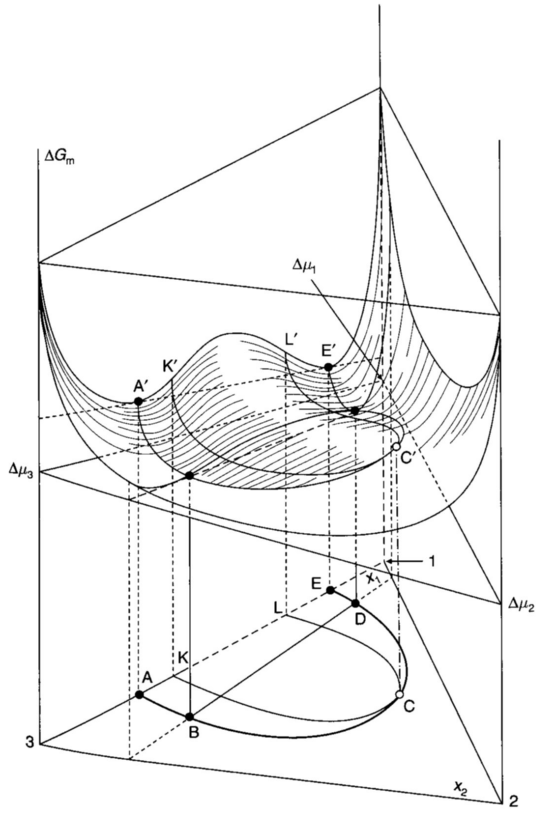

(a)

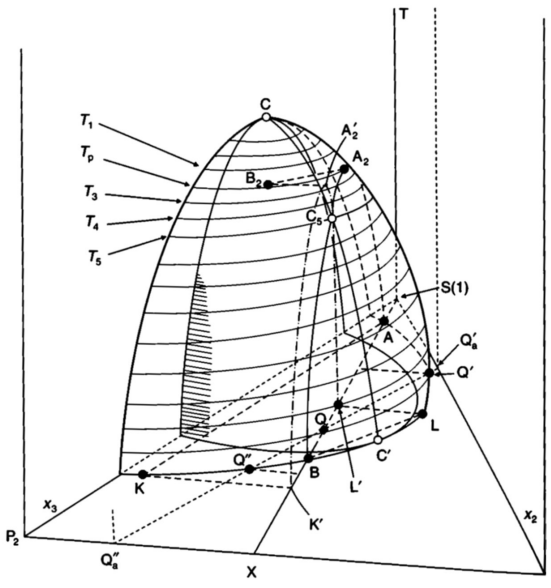

(b)

FIGURE 2.9: (a) Free energy-of-mixing surface for a partially miscible ternary system at a constant P and T. (b) Miscibility gap for a ternary system at a constant pressure. Taken from Polymer Phase diagram: A texbook, R. Koningsveld, W. H. Stockmayer, and E. Nies, pages 81-82 (2001), with permission from Oxford University Press

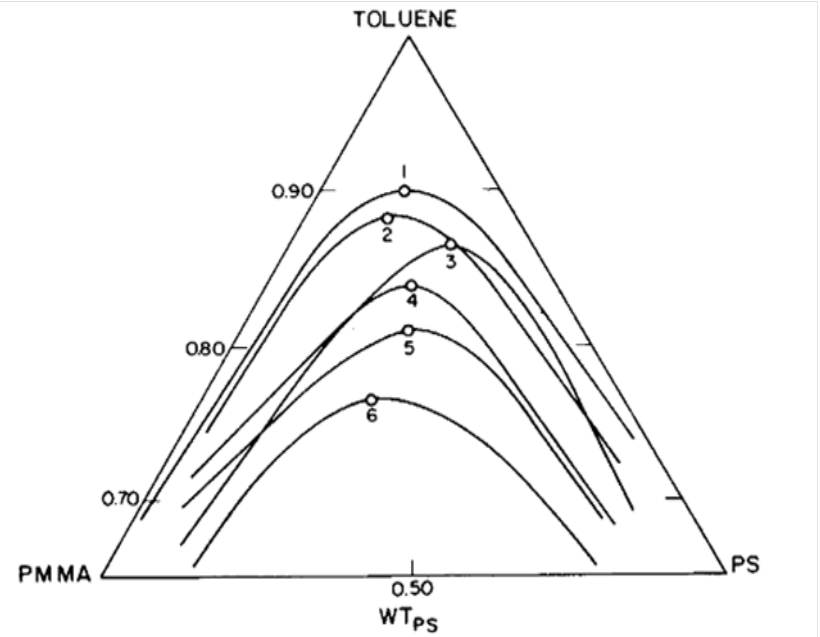

FIGURE 2.10: Phase diagram and the plait point for the ternary mixture PS/PMMA/toluene,.(1) PS100K/PMMA180K/toluene,(2) PS100K/PMMA69K/toluene, (3) PS37K/PMMA69K/toluene,(4) PS37K/PMMA69K/toluene, (5) PS100K/PMMA29K/toluene, (6) PS37K/PMMA29K/toluene. Here 1K=1 kg mol^{-1}. Reprinted from W. W. Y. Lau, C. M. Burns and R. Y. M. Huang *J. Appl. Poly. Sci.* **23** 37 (1987) with permission from John Wiley and Sons

the plait point. Figure 2.10 shows the phase diagram for the different molecular weights studied.

Notice that as the molecular weights of the two polymers decrease, the binodal line moves away from the apex of the toluene. In other terms at low molecular weights a blend of PS, PMMA and toluene is in a single phase for lower solvent volume fraction. Han and Mozer [88] studied the conformation of dPS-PMMA diblock copolymer in toluene and its dPS precursor in toluene using SANS and light scattering experiments. The radius of gyration of the PMMA block was significantly smaller than that of PMMA in toluene whereas the dPS block was only slightly expanded compared to its precursor in toluene. The dPS-PMMA block has a core and shell mode. The PMMA block act as a core to reduce the interaction with the PS block and the dPS block act as the shell. This configuration could be explained by the fact that toluene is a better solvent for PS than PMMA.

We will be working with PS and PMMA with molecular weights of 96 Kg mol^{-1} and 106 Kg mol^{-1}, respectively. Although none of the phase diagrams above correspond to

the system that we are studying, these diagrams give us an idea of the miscibility of the system.

2.2 Phase separation at the vicinity of a surface

2.2.1 Surface tension

Molecules at the surface of a liquid will exercise cohesive forces, which will resist to external forces trying to break the surface. Surface tension σ, is defined as the force per unit of length or energy per unit of density that a surface experiences. The surface tension is related to the Helmholtz free energy and the surface area A by

$$\sigma = \frac{dF}{dA}. \tag{2.23}$$

Surface tension determines the nature of the interaction at the substrate/polymer, the air/polymer and the polymer/polymer interfaces.

2.2.2 Surface segregation

When a multicomponent system is exposed to an interface, the concentration profile at the vicinity of the interface differs from that of the bulk. The component with the lowest surface energy is absorbed at the surface to lower the total energy of the system. The free energy can be written as

$$\frac{\triangle G}{k_{\mathrm{B}T}} = f_s(\phi) + \int_0^\infty \left[\triangle G_{\mathrm{mix}}(\phi) - \phi\triangle\mu_\infty + \frac{a^2}{24\phi(1-\phi)}\left(\frac{d\phi}{dz}\right)^2\right]dz, \tag{2.24}$$

where the f_s represent the benefit of having the component with the lowest surface energy segregated at the surface. $\triangle G_{\mathrm{mix}}(\phi)$ is the Flory-Huggins free energy, $\triangle\mu_\infty$ is the chemical potential of the bulk system. $G_{\mathrm{mix}}(\phi) - \triangle\mu_\infty$ represents the penalty for having the composition at the surface different from the composition in the bulk. The last term in Equation 2.24 is the energy cost in having a composition gradient in the film, in this term a is the Kuhn length. In a binary miscible blend in which component A has a surface energy lower than component B, the composition profile $\phi(z)$ which describes the changes in the composition from the surface to the bulk, decays continuously from

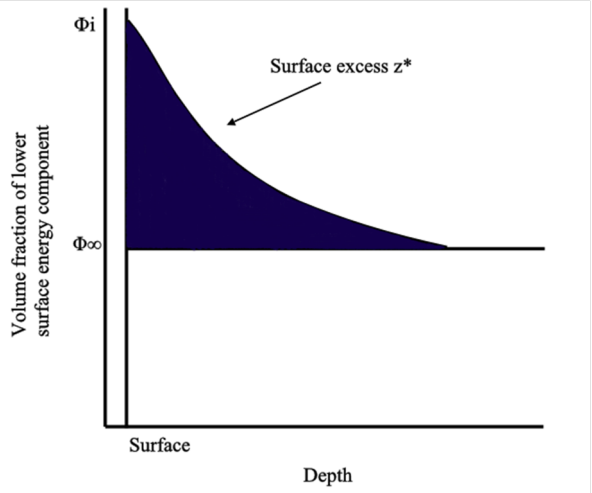

FIGURE 2.11: Diagram illustrating surface excess: the volume fraction/depth profile.

the composition $\phi(A)$ to the bulk composition ϕ_∞ over a length scale λ, see Figure 2.11. The excess amount of polymer segregated at the surface is the surface excess, Z^* which has a dimension of mass per unit area and is expressed as

$$Z^* = \int (\phi(z) - \phi_\infty)\, dz. \tag{2.25}$$

Jones and Kramer studied the dependence of Z^* on χ. As the interaction parameter increases i.e as we approached the critical temperature the amount of polymer A absorbed at the surface increases.

2.2.3 Wetting and wetting transition

When an immiscible polymer blend is in contact with a surface two situations occur, depending on the the interaction between the two components and their interaction with the surface. Either the component with the lower surface energy forms a macroscopic layer at the surface, separating the second component from the surface. Or the two components are in contact with a finite contact angle. The Young's modulus equation dictates which one of theses two conformations exist at equilibrium,

$$\cos\theta = \frac{\sigma_B - \sigma_{AB}}{\sigma_A}. \tag{2.26}$$

where σ_A, σ_B are the surface energy of the two phase A and B, and σ_{AB} is the interfacial energy. When $\theta = 0$, we speak of complete wetting. The situation where $\theta =< 90$ is

referred to as partial wetting. No value of θ will satisfy Equation 2.26 unless the values of $\cos\theta$ range between 0 and 1. This leads to the following inequality

$$\sigma_{\mathrm{B}} - \sigma_{\mathrm{A}} < \sigma_{\mathrm{AB}} \tag{2.27}$$

When this inequality is not fulfilled the complete wetting occurs. Cahn indicated that as the critical point is approached σ_{AB} to decays to zero faster than $\sigma_{\mathrm{B}} - \sigma_{\mathrm{A}}$, therefore there will always be a transition from partial wetting to complete wetting. The temperature at which this transition occurs is called the wetting temperature $\mathrm{T_w}$. The transition can either be a first order or second order transition.

2.2.4 Marangoni instabilities

Marangoni effects are the convective flow caused by temperature or concentration gradients. These instabilities were first observed by Bénard [22] reporting the formation of hexagonal pattern on a liquid heated from below. Similar observations were reported by Carlo Marangoni [23]. Bénard [22] initially assumed that the surface tension at the top layer plays an important role in this phenomenon but abandoned this idea after Lord Rayleigh [24] explained that this phenomenon was due to buoyancy forces. Block [25] experimental work finally corrected this misinterpretation by demonstrating that the Bénard cells were due to temperature dependent surface tension. The Marangoni effect is sometimes referred to as the Bénard-Marangoni in recognition of Bénard's work. Pearson [26] performed a theoretical study on the subject using linear analysis; he defined the Marangoni number as being equal to

$$\mathrm{Ma} = \frac{\left(\frac{\partial\sigma}{\partial T}\right) h \triangle T}{\mu a}, \tag{2.28}$$

where σ is the surface tension, h is the thickness of the layer, $\triangle T$ the temperature difference between the bottom and the top of the liquid, μ the viscosity and the thermal diffusivity. The authors also reported that the Marangoni cells were observed when this number reached the critical value of 80. In spin coating; temperature differences and solvent gradient can both be induced by the solvent evaporation. As the solvent evaporate the upper layer of the film is cooled, this is often referred to as evaporative cooling. The losses of solvent at the air/liquid interface leads to a solvent concentration

gradient in the radial direction of the film which creates a surface tension gradient. This creates a flow from the region of low surface tension to the region of high surface tension. This motion creates convection cells, called Marangoni cells. Because the solvent only evaporates from the top layer of the film, evaporative cooling will only be experienced for a certain fraction of the film thickness and the temperature gradient near the surface will be stronger than the one experienced in the bulk. Currie [27], and Vidal and Acrivos [28] introduce the parameter d which is the penetration depth; and represents the thickness over which the temperature drop is experienced in the film. Using this definition Haas *et al.* [29] proposed the following expression of the Marangoni number

$$\mathrm{Ma} = \frac{\left(\frac{\partial\sigma}{\partial T}\right) h^2 \triangle T}{\mu a d}. \tag{2.29}$$

Birnie [30] speculated that since the Marangoni number is proportional to the square of the film thickness once the film has reached 10 % percent of its initial thickness, Marangoni effects driven by temperature gradients will be negligible compared to those driven by the concentration gradient. He proposed the following expression to calculate the Marangoni number

$$\mathrm{Ma} = \frac{\left(\frac{\partial\sigma}{\partial C}\right) h^2 \nabla C}{\mu D}, \tag{2.30}$$

where C is the relevant composition variable and D is the diffusion rate of the component driving the composition dependent surface tension. The Marangoni effect can be suppressed by reducing the evaporation rate. Luo *et al.* [31] studied the morphology of film of PS and PMMA films coated from good and bad solvents in the presence of solvent vapour. Striations were suppressed when films were cast in the presence of vapour independently of the quality of the solvent. Mokarian-Tabari *et al.* [11] report similar result when studying the morphology of PS and PMMA films cast at different vapour pressure. The higher the vapour pressure in the chamber the smoother the surface and the less pronounced the phase separation. This is due to the fact that low evaporation rates reduced solvent concentration gradients therefore reducing the Marangoni effect.

2.2.5 Surface directed spinodal decomposition

In 1981; Cohen and Reich [32] investigated the influence of a confining surface on the phase separation of thin films obtained via dip coating. They reported that besides

the polymer-polymer interactions, phase separation in a confined space is influenced by the nature of the polymer-surface interactions and the geometrical constrains on the chain conformation due to the presence of boundaries. These influences were reported to be stronger as the film thickness decreased. In 1989, Jones *et al.* [33] observed the segregation of d-PS at the surface investigating the phase separation of the isotopic blend PS/d-PS. The preferential attraction of d-PS at the surface is believed to be driven by the difference in the surface energy of PS and d-PS due to the difference of length and polarizability of the C-H and C-D bonds. Figure 2.12 shows the results of the experiment. The depth concentration of dPS in the as cast film is constant, however the annealed sample show a higher volume fraction of dPS at the surface of the film. In 1990, Ball *et al.* [34] studied the effect of boundary conditions at the surface of a phase separating blend via spinodal decomposition. This was the first time that it was suggested that the presence of a surface breaks the translational and rotational symmetry of the spinodal decomposition, therefore leading to a one dimensional ordering. Bruder and Brenn [35] studied late stage spinodal decomposition as a function of the surface energy; by altering the substrate, they concluded that bilayers can be formed only if there is complete wetting at the substrate and the vacuum surface. The following year Jones *et al.* [36] observed perpendicular spinodal waves propagating from the surface during the phase separation of a thin film: this type of phase separation is called surface directed phase separation[11]. Puri *et al.* [37] revisited the Cahn-Hillard equation by adding adequate boundary conditions to imitate the preferential attraction of the component to the surface. They reported an anisotropic phase separation due to the presence of the surface as observed by Jones *et al.* [36].

In 1993, Krausch [10] used nuclear reaction analysis and time of flight forward recoil spectroscopy to investigate phase separation in poly(ethylenepropy1ene) (PEP) and perdeuterated poly(ethylenepropy1ene) (dPEP). The hydrogenated polymer is know to have a higher surface energy than the deuterated polymer. This mixture exhibit a UCST with $T_{\mathrm{w}} = 365$ K. Film of different thickness were obtained by coating solutions with different solvent content. The films were annealed at 321 K, under vacuum. The results of this work are shown in Figure 2.13, the authors observed the propagation of two spinodal waves: one from the interface between the subtract and the polymer and another from the interface between the polymer film and the vacuum. The solid line are the fit to the data, the equation used to fit the data comprise three term, one that

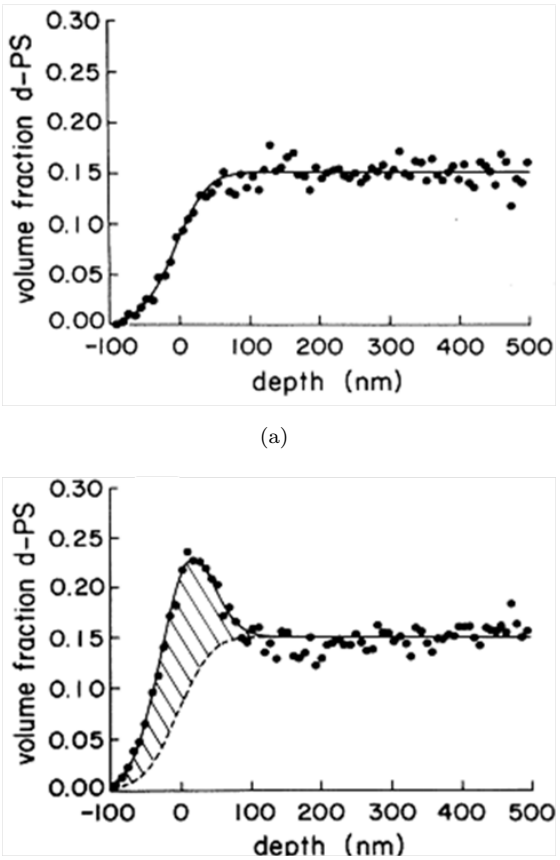

FIGURE 2.12: Depth profile of d-PS in a blend with PS with an initial volume fraction d-PS of 0,15, (a) before and (b) after annealing at 184C for 4 days. The dots are the experimental data obtained forward-recoil spectrometry (FRES) and the solid lines are the fits to the data. Reprinted with permission from R. A. L. Jones, E. J. Kramer, M. H. Rafailovich, J. Sokolov, and S. A. Schwarz *Phys. Rev. Lett.* **62** 280 (1989). Copyright (1989) by the American Physical Society.

represent the average value of dPEP in the polymer blend film (0.5), the two other terms were, one positive and one negative damped cosine waves to represent the segregation of dPEP at the surface and the segregation of hPEP at the substrate. These two waves were in and out of phase, leading to the observation of destructive and constructive interferences as the film thickness was reduced. When the thickness of the film was comparable or thinner than the length of the spinodal wave, the film was in a bilayer structure (see Figure 2.13). These results were confirmed with a simulation. Geoghegan *et al.* [38] studied the structure of dPS and polybutadiene (PB) films cast from toluene on silicon substrate. The volume fraction of dPS was changes, however it never exceed the critical value for which the blend phase separate. They observed a three-layer lamellar structure with a PB layer intercalated between two PS layers. The interfaces of the

polymer-polymer layer were reported to be sharper as the volume fraction of dPS was reduced. The authors observed a wetting transition as the volume fraction of PS is increased

In 1996 Walheim *et al.* [39, 40] investigated the morphology of PS and PMMA blend cast from different solvents on substrates with various surface energy. The solvent was depleted faster in the domains made of the less soluble polymer. As a result these were thicker than the domains of the more soluble polymer. The surface directed spinodal decomposition might at first create a bilayer structure and the top layer will then dewet and create small clusters of polymer. In 1997, Dalnoki *et al.* [41] studied the morphology of PS and polyisopropene (PI) films cast from toluene and the morphology of PS and PMMA blend cast from methyl ethyl ketone (MEK) as a function of PS volume fraction. They showed the existence of a critical value of PS volume fraction for which the structure evolved from islands of PS in a matrix of PMMA or PI to a bi-continuous layer. Further increase of the PS content led to a morphology with PMMA or PI rich phases in a PS matrix. In 2005, Jukes *et al.* [9] demonstrated a device which associates specular reflectivity and off-specular scattering to allow *in situ* evolution of phase separation polymer thin films (optospinometer). The reflectivity data revealed the existence of two phases during spin casting: a stage of rapid thinning due the centrifugal forces followed by a regime with a constant evaporation. The same year Heriot *et al.* [42] demonstrated that a blend of two polymers undergoes at first a vertical stratification and then layers break due to the instability of the transient wetting layer at the surface and at the substrate due to the solvent gradient in the film (Marangoni effect).

In 2004 Clarke *et al.*[43] developed the first theoretical framework which combines phase separation and dewetting. This model however, is restricted, as only concentration fluctuations parallel to the substrate are taken into account. In 2005, Clarke *et al.* reported the time composition dependence for film which has undergone dewetting followed by phase separation compared with that of a film which went simultaneously through phase separation and dewetting, on this latter the percolation path present on the former disappeared [44]. More recently Mokarian-Tabari *et al.* [11] showed how different morphologies could be achieved by a quantitative control of the evaporation rate. The evaporation rate was controlled by using a bubbler to set the solvent vapour pressure in an environment cell. As the evaporation rate was reduced the Marangoni

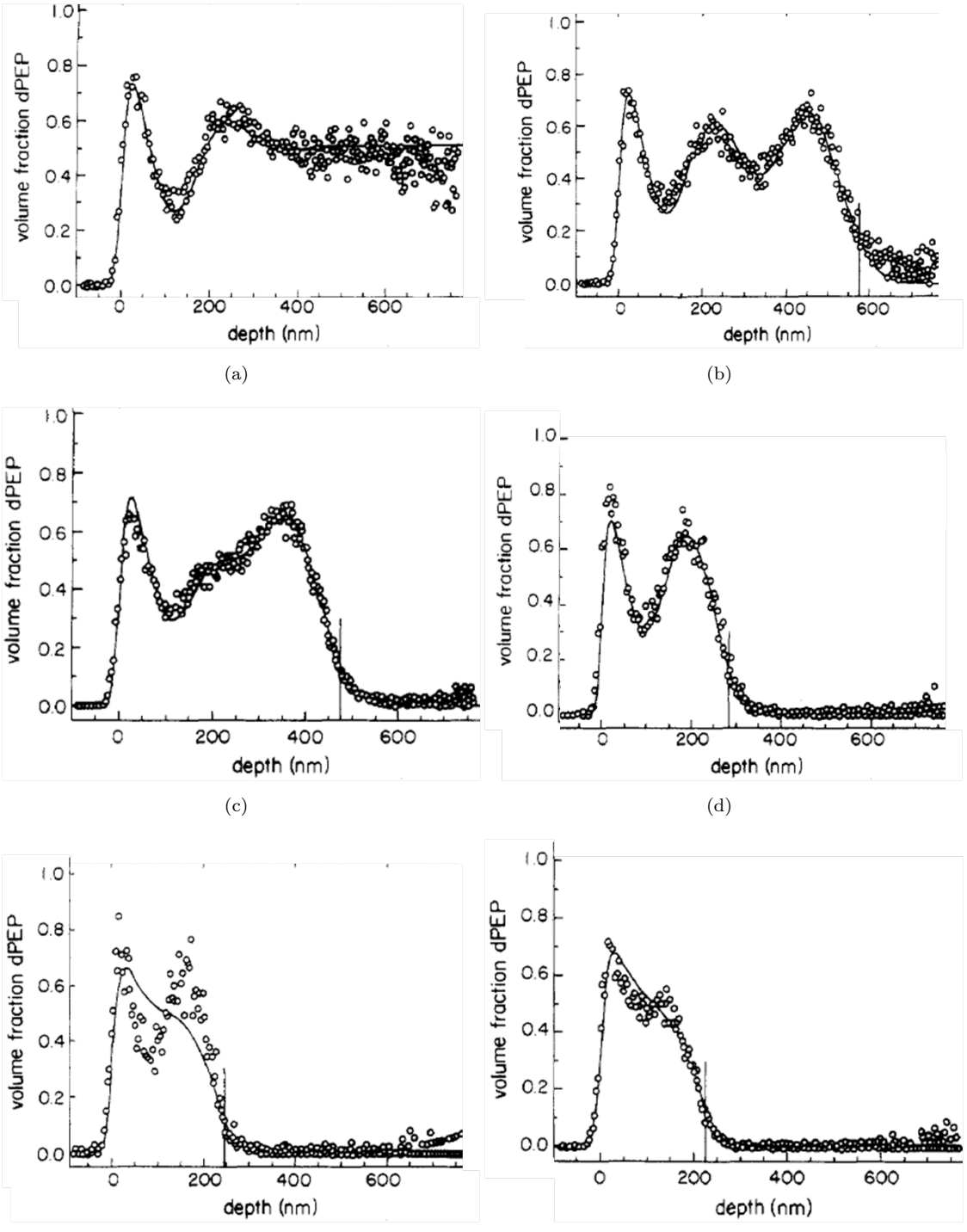

FIGURE 2.13: Depth profile of the volume fraction of dPEP, (a) $h_f > 1000$ nm, (b)$h_f = 574$ nm, (c) $h_f = 474$nm, (d) $h_f = 282$ nm, (e) $h_f = 240$ nm, (f) $h_f = 220$ nm. The data are the data, the solid lines are the fit obtain by accounting for the two spinodale wave. Reprinted from G. Krausch *Mat. Sci. Eng: R.* **14** 5566 (1995) with permision from Elsevier

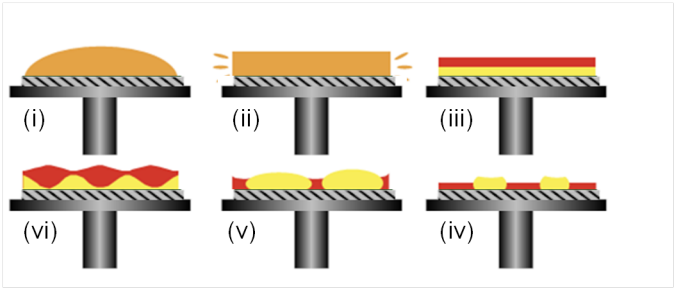

FIGURE 2.14: A schematic model describing the film formation during the spin casting process and the film formation during the spin casting process, and the final morphology. After the initial spin-off stage where both polymer and solvent are removed (i), (ii) the film separates into two layers (iii) and the film thins owing to solvent evaporation only. The interface between the polymers destabilized (iv) and the film phase-separates laterally (v), (vi). Reprinted from S. Y. Heriot and R. A. L. Jones *Nat. Mater* **4** 782 (2005) with permission from Nature Publishing Group.

effect did not initiate lateral phase separation and bilayered structures were obtained. Dunbar *et al.* [6] investigated phase separation as a function of solvent concentration. They observed a more pronounced phase separation as the concentration of solvent was decreased. Souche *et al.* [45] carried out a linear analysis of the Marangoni instabilities on a deformable liquid /liquid interface; they reaffirmed the existence of a transiently bilayered structure during the phase separation of a thin film. They also used the mean field Flory-Huggins-de Gennes theory to predict the structure of a polymer blend confined within asymmetric walls as a function of the temperature [46]. In this study the solvent gradient is not taken into account. Various morphologies were obtained, from bilayer to lateral phase separated as the system evolved from a one phase region to the two phase region of the phase diagram. Souche *et al.* pursued their investigation of polymer blends by studying the influence of the solvent concentration. They calculated the concentration profile of a mixture polymer A/polymer B/solvent confined between two asymmetric walls with respect to the two polymers. Here again various structures were achieved from monolayer in the one phase region to bilayer or laterally phase separated in the two phase region depending on the temperature [47].

2.3 Dynamics of spin coating

2.3.1 Emslie Bonner and Peck's Model

In 1958 EBP [1] investigated the mathematical modelling of spin coating by considering the symmetric flow of a non-volatile Newtonian liquid rotating on an infinite plate. Working in cylindrical polar coordinates (r, θ, z) they defined the velocity vector $\overrightarrow{u}$, the angular velocity $\overrightarrow{\omega}$ and the radial vector $\overrightarrow{r}$ as being equal to $\overrightarrow{u} = (u_r, u_\theta, u_z)$, $\overrightarrow{\omega} = (0, 0, \omega)$ and $\overrightarrow{r} = (r, 0, 0)$, respectively. Their calculations where based on the following assumptions:

- the plane is infinite
- the plate is horizontal therefore the gravitational force can be neglected
- Coriolis forces are negligible
- the flow is Newtonian: the viscosity is independent of the shear rate and $\tau = \eta\dot{\gamma}$. Here τ is the shear stress and $\dot{\gamma}$ is the shear rate i.e. the velocity gradient in the fluid.
- the shearing forces are appreciable only in the horizontal planes (see $u(z)$ in Figure 2.15)

The relative velocity between the substrate and the fluid adjacent to the substrate is equal to zero, $\overrightarrow{u(0)} = 0$. The flow is Newtonian, therefore, $\tau = \eta\frac{\partial u_r}{\partial z}$. The thinning of the film is exclusively due to the centrifugal and the viscous forces which balance each other out,

$$-\overrightarrow{f_{ce}} = \overrightarrow{f_{vis}}. \tag{2.31}$$

Note that these two forces exert only in the radial direction. The centrifugal forces are equal to:

$$\overrightarrow{f_{ce}} = \rho\overrightarrow{\omega} \times (\overrightarrow{\omega} \times \overrightarrow{r}) = (\rho r\omega^2, 0, 0). \tag{2.32}$$

The viscous forces are equal to the viscosity multiplied by the Laplacian of the velocity vector,

$$\overrightarrow{f_{vis}} = \eta\nabla^2\overrightarrow{u}. \tag{2.33}$$

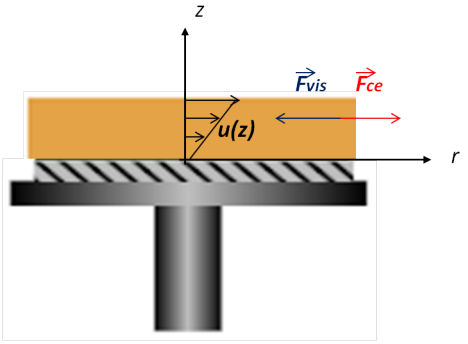

FIGURE 2.15: Diagram of a rotating polymer film in cylindrical coordinates

In cylindrical coordinates the Laplacian of the velocity vector is equal to,

$$\nabla^2\overrightarrow{u} = \left(\triangle u_r - \frac{u_r}{r^2} - \frac{2}{r^2}\frac{\partial u_r}{\partial\theta}\right)\vec{r} + \left(\triangle u_\theta - \frac{u_\theta}{r^2} - \frac{2}{r^2}\frac{\partial u_\theta}{\partial\theta}\right)\vec{\theta} + \triangle u_z\vec{z}. \tag{2.34}$$

Because the centrifugal forces only act on the radial direction, we focus on the radial component of Equation 2.34 , in which $\triangle u_r$ is the laplacian of the radial component of the velocity vector which is equal to

$$\triangle u_r = \frac{1}{r}\frac{\partial}{\partial r}\left(r\frac{\partial u_r}{\partial r}\right) + \frac{1}{r^2}\frac{\partial^2 u_r}{\partial\theta^2} + \frac{\partial^2 u_r}{\partial z^2}. \tag{2.35}$$

Therefore the viscous forces are equal to

$$F_{vis} = \frac{\partial^2 u_r}{\partial z^2} + \frac{1}{r}\frac{\partial}{\partial r}\left(r\frac{\partial u_r}{\partial r}\right) + \frac{1}{r^2}\frac{\partial^2 u_r}{\partial\theta^2} - \frac{u_r}{r^2} - \frac{2}{r^2}\frac{\partial u_r}{\partial\theta} \tag{2.36}$$

As we consider the special case of an infinite plate $\frac{1}{r} \simeq 0$, the balance between the centrifugal forces and the viscous forces leads to the equality

$$\frac{\partial^2 u_r}{\partial z^2} = -\rho\omega^2 r. \tag{2.37}$$

In this equation ρ is the fluid density and ω is the spin speed. The viscosity η is constant throughout the process because the fluid is made of a single non-volatile component. We define the kinematic viscosity as being equal to $\nu = \frac{\eta}{\rho}$. The integration of Equation 2.37 with the boundary condition ($z = h, \frac{\partial u_r}{\partial z} = 0$) gives

$$\frac{\partial u_r}{\partial z} = \frac{\omega^2 r z}{\nu} + \frac{\omega^2 r h}{\nu}. \tag{2.38}$$

Integrating this equation with the boundary condition ($z = 0, u_r = 0$) yields a radial velocity equal to

$$u_r = \frac{\omega^2 r z^2}{\nu} + \frac{\omega^2 r h z}{\nu} \tag{2.39}$$

EBP used the continuity equation to express the thinning rate:

$$\frac{\partial h}{\partial t} = -\frac{1}{r}\frac{\partial (rq)}{\partial r}. \tag{2.40}$$

In this equation h is the film thickness and q is the radial flow per unit of circumference which is equal to

$$q = \int_0^h u_r = \frac{\omega^2 r h^3}{3\nu}. \tag{2.41}$$

Substituting Equation 2.41 into equation Equation 2.40 gives a thinning rate equal to

$$\frac{\partial h}{\partial t} = -\frac{1}{r}\frac{\omega^2}{3\nu}\frac{\partial (r^2 h^3)}{\partial r}. \tag{2.42}$$

The EBP model is said to be one–dimensional as they considered a uniform thickness distribution. This translates mathematically into $\frac{\partial h}{\partial r} = 0$, i.e. the thickness does not depend on the radial position. In this case Equation 2.42 become:

$$\frac{\partial h}{\partial t} = -\frac{2\omega^2 h^3}{3\nu}. \tag{2.43}$$

Equation 2.43 is a first order differential equation which give the thickness profile when solved for $h(t)$. Multiplying both side by $\frac{\partial t}{h^3}$ gives

$$\frac{\frac{\partial h}{\partial t}}{h^3}\partial t = -\frac{2\omega^2}{3\nu}\partial t. \tag{2.44}$$

Integrating both sides with respect to t yields

$$-\frac{1}{2h^2} = -\frac{4\omega^2}{3\nu}t + c. \tag{2.45}$$

In this equation c is a constant of integration which can be calculated by applying the initial conditions ($t = 0, h = h_o$),

$$h(t) = h_o \left(\frac{t 4 h_o^2 \omega^2}{3\nu} + 1\right)^{-1/2}.$$

EBP used this model to predict the uniformity of the dry film for films with an initially rough radial profile and for films for which the radial profile follows a Gaussian distribution. Their results showed that the dry film is radically uniform independently of the initial profile.

2.3.2 Model proposed by Meyerhofer

The EBP model does not give an accurate modelling of spin coating since it doesn't account for the changes in viscosity and solvent evaporation. Similar to EBP [1], Meyerhofer [2], neglected the gravitational forces and the Coriolis forces, and so the radial velocity term is identical to the one calculated by EBP [1]. He assumed a constant evaporation rate e and expressed the thinning rate of spin coated films by

$$\frac{\partial h}{\partial t} = -\frac{2\omega^2 h^3}{3\nu} - e. \tag{2.46}$$

In order to solve Equation 2.46, Meyerhofer assumed that the thickness of the film is equal the thickness of the solute plus the thickness of the solvent. He defined the solid concentration $c(t)$ and the film thickness $h(t)$ as being equal to

$$c(t) = \frac{S}{S+L} \tag{2.47}$$

and

$$h(t) = S + L. \tag{2.48}$$

In these equations S is the volume of solid and L is the volume of liquid. The solute layer only thins due to the radial convection. In addition to this the liquid layer also thins due to the solvent evaporation. These assumptions lead to the differential equations

$$\frac{\partial S}{\partial t} = -c\frac{2\omega^2 S^3}{3\nu} \tag{2.49}$$

and

$$\frac{\partial L}{\partial t} = -(1-c)\frac{2\omega^2 L^3}{3\nu} - e. \tag{2.50}$$

In Equation 2.50; e is a constant evaporation rate driven by the difference in solvent concentration at the free surface. Meyerhofer expressed the time dependent viscosity as

equal to

$$\eta = \eta_s + \eta_{sol} c^{\gamma}, \tag{2.51}$$

where η_s is the viscosity of the solvent, η_{sol} is the viscosity of the solid and γ is a fitting parameter. For the solution studied Meyerhofer found $\gamma = 2.5$. Since Equation 2.50 and Equation 4.10 cannot be solved analytically, Meyerhofer simplified the mathematics by breaking down the process into two regimes. In the first one the film only thins due to radial outflow. In the second regime the thinning of the film is exclusively due to the solvent evaporation. The transition between these two regimes is defined as the time when the losses due to convection are equal to those due to the mass transfer i.e. when the two terms on the right in Equation 2.50 are equal. Therefore the thickness of the liquid layer at the transition time L_t is obtained by solving

$$-(1-c)\frac{2\omega^2 L_t^3}{3\nu} = e. \tag{2.52}$$

Solving Equation 2.52 for L_t gives

$$L_t = \left[\frac{3e\nu}{2(1-c)\omega^2}\right]^{1/3}. \tag{2.53}$$

Meyerhofer assumed that at t_t most of the thinning is achieved; therefore the final film thickness can be expressed as

$$h_f = c\left[\frac{3e\nu}{2(1-c)\omega^2}\right]^{1/3}. \tag{2.54}$$

Meyerhofer used Equation 2.54 to predict the final thickness for films coated at different spin speed.

2.3.3 Model proposed by Reisfeld

2.3.3.1 Governing equations

The governing equations are a set of differential equations that describe the motion of a fluid. They comprise of the Navier-Stokes equations, the continuity equation and the boundary conditions. RBD [3] studied the flow of an axisymmetric, incompressible Newtonian liquid. They aimed to give a more accurate description of the early stage of

the process, where the inertia forces are important. Working in cylindrical coordinates (r, θ, z), the fluid velocity vector $\overrightarrow{u}$, the angular velocity $\overrightarrow{\omega}$ and the radial vector $\overrightarrow{r}$ are defined by (u_r,u_θ,u_z), (0,0,ω) and (r,0,0), respectively. The unit normal vector $\overrightarrow{n}$ and the unit tangent vectors $\overrightarrow{t_r}$ and $\overrightarrow{t_\theta}$ are equal to

$$\overrightarrow{n} = (\frac{\partial h}{\partial r}, 0, 1)\left(1 + \left(\frac{\partial h}{\partial r}\right)^2\right)^{-1/2}, \tag{2.55}$$

$$\overrightarrow{t_r} = (1, 0, \frac{\partial h}{\partial r})\left(1 + \left(\frac{\partial h}{\partial r}\right)^2\right)^{-1/2}, \tag{2.56}$$

and

$$\overrightarrow{t_\theta} = (0, 1, 0). \tag{2.57}$$

The Navier-Stokes equation and the continuity equation

For an incompressible Newtonian fluid the Navier-Stokes equation in the vector form is expressed as

$$\rho\left[\frac{\partial \overrightarrow{u}}{\partial t} + \overrightarrow{u}.\nabla\overrightarrow{u}\right] = -\nabla P + \rho\overrightarrow{g} + \nabla.T + \overrightarrow{f}. \tag{2.58}$$

Equation 2.58 has a r, θ and z components which are also called radial, azimuthal and vertical components. Expanding Equation 2.58 in the cylindrical coordinates gives a radial component equal to,

$$\begin{aligned}\rho\left[\frac{\partial u_r}{\partial t} + u_r\frac{\partial u_r}{\partial r} - \frac{u_\theta^2}{r} + u_z\frac{\partial u_r}{\partial z}\right] &= -\frac{\partial P}{\partial r} + \mu\left[\frac{1}{r}\frac{\partial}{\partial r}\left(r\frac{\partial u_r}{\partial r}\right) - \frac{u_r}{r^2} + \frac{\partial^2 u_r}{\partial z^2}\right] \\ &\quad +\rho g_r + f_r.\end{aligned} \tag{2.59}$$

The azimuthal component of Equation 2.58 is expressed as

$$\rho\left[\frac{\partial u_\theta}{\partial t} + u_r\frac{\partial u_\theta}{\partial r} + \frac{u_r u_\theta}{r} + u_z\frac{\partial u_\theta}{\partial z}\right] = \mu\left[\frac{1}{r}\frac{\partial}{\partial r}\left(r\frac{\partial u_\theta}{\partial r}\right) - \frac{u_\theta}{r^2} + \frac{\partial^2 u_\theta}{\partial z^2}\right] + \rho g_\theta + f_\theta. \tag{2.60}$$

The axial component of Equation 2.58 is given by

$$\rho\left[\frac{\partial u_z}{\partial t} + u_r\frac{\partial u_z}{\partial r} + u_z\frac{\partial u_z}{\partial z}\right] = -\frac{\partial P}{\partial z} + \mu\left[\frac{1}{r}\frac{\partial}{\partial r}\left(r\frac{\partial u_z}{\partial r}\right) + \frac{\partial^2 u_z}{\partial z^2}\right] + \rho g_z + f_z. \tag{2.61}$$

In these equations P is the pressure, T is the viscous tensor, $\overrightarrow{g}$ is the gravitational vector defined as $(0, 0, g)$, and $\overrightarrow{f}$ represents the non-viscous forces exerted on the fluid.

When applying the Navier-Stokes equation the first step is to identify $\overrightarrow{f}$. RBD took in account two forces: the centrifugal forces $\overrightarrow{f_{ce}}$ and the Coriolis forces $\overrightarrow{f_{co}}$. These are expressed by the following equations

$$\overrightarrow{f_{co}} = \rho 2\overrightarrow{\omega} \times \overrightarrow{u} = (-2\rho\omega u_\theta, -2\rho\omega u_r, 0) \tag{2.62}$$

and

$$\overrightarrow{f_{ce}} = \rho\overrightarrow{\omega} \times (\overrightarrow{\omega} \times \overrightarrow{r}) = (\rho r\omega^2, 0, 0). \tag{2.63}$$

Substituting Equation 2.62 and Equation 2.63 into Equation 2.59, the radial component of the Navier-Stokes equation is equal to

$$\begin{aligned}\rho\left[\frac{\partial u_r}{\partial t} + u_r\frac{\partial u_r}{\partial r} - \frac{u_\theta^2}{r} + u_z\frac{\partial u_r}{\partial z}\right] &= -\frac{\partial P}{\partial r} + \mu\left[\frac{1}{r}\frac{\partial}{\partial r}\left(r\frac{\partial u_r}{\partial r}\right) - \frac{u_r}{r^2} + \frac{\partial^2 u_r}{\partial z^2}\right] \\ &\quad +2\rho\omega u_\theta + \rho r\omega^2.\end{aligned} \tag{2.64}$$

The azimuthal component of the Navier-Stokes equation is given by

$$\rho\left[\frac{\partial u_\theta}{\partial t} + u_r\frac{\partial u_\theta}{\partial r} + \frac{u_r u_\theta}{r} + u_z\frac{\partial u_\theta}{\partial z}\right] = \mu\left[\frac{1}{r}\frac{\partial}{\partial r}\left(r\frac{\partial u_\theta}{\partial r}\right) - \frac{u_\theta}{r^2} + \frac{\partial^2 u_\theta}{\partial z^2}\right] - 2\rho\omega u_r, \tag{2.65}$$

which is equivalent to

$$\rho\left[\frac{\partial u_\theta}{\partial t} + u_r\frac{\partial u_\theta}{\partial r} + \frac{u_r u_\theta}{r} + u_z\frac{\partial u_\theta}{\partial z}\right] = \mu\left[\frac{1}{r^2}\frac{\partial}{\partial r}\left(r^3\frac{\partial}{\partial r}\left(\frac{u_\theta}{r}\right)\right) + \frac{\partial^2 u_\theta}{\partial z^2}\right] - 2\rho\omega u_r. \tag{2.66}$$

The axial component of the Navier-Stokes equation is given by

$$\rho\left[\frac{\partial u_z}{\partial t} + u_r\frac{\partial u_z}{\partial r} + u_z\frac{\partial u_z}{\partial z}\right] = -\frac{\partial P}{\partial z} + \mu\left[\frac{1}{r}\frac{\partial}{\partial r}\left(r\frac{\partial u_z}{\partial r}\right) + \frac{\partial^2 u_z}{\partial z^2}\right] - \rho g, \tag{2.67}$$

which is equivalent to

$$\rho\left[\frac{\partial u_z}{\partial t} + u_r\frac{\partial u_z}{\partial r} + u_z\frac{\partial u_z}{\partial z}\right] = -\frac{\partial P}{\partial z} + \mu\left[\frac{1}{r}\frac{\partial u_z}{\partial r} + \frac{\partial^2 u_z}{\partial r^2} + \frac{\partial^2 u_z}{\partial z^2}\right] - \rho g. \tag{2.68}$$

The continuity equation given by

$$\frac{1}{r}\frac{\partial}{\partial r}(ru_r) + \frac{\partial u_z}{\partial z} = 0. \tag{2.69}$$

Boundary conditions

The boundary conditions are a set of conditions that describe the behaviour of a fluid at its boundaries. When studying the flow of a rotating fluid, there are two boundaries: the air/film boundary and the substrate/film boundary. The substrate is impenetrable and the film spins at the same speed as the substrate. This condition is called the no-slip condition i.e.

$$u_r(0) = 0, \tag{2.70}$$

$$u_\theta(0) = 0, \tag{2.71}$$

and

$$u_z(0) = 0.. \tag{2.72}$$

The boundary conditions at a free surface are described by the kinematic boundary condition and the dynamic boundary condition. The kinematic boundary condition relates the motion of the air/film interface to the velocities of the fluid at the free surface. Taking into account the mass transfer, the kinematic boundary condition at the free surface can be expressed as

$$(\overrightarrow{u} - \overrightarrow{u_{in}}).\overrightarrow{n} = J. \tag{2.73}$$

In this equation J is the mass transfer, $\overrightarrow{u_{in}}$ is velocity at the interface and $\overrightarrow{u_{in}}.\overrightarrow{n} = \frac{\partial h}{\partial t}\left(1 + \left(\frac{\partial h}{\partial r}\right)^2\right)^{-1/2}$. Developing Equation 2.73 yields to

$$\left(-\frac{\partial h}{\partial t} - u_r\frac{\partial h}{\partial r} + u_z\right)\left(1 + \left(\frac{\partial h}{\partial r}\right)^2\right)^{-1/2} = J. \tag{2.74}$$

The dynamic boundary conditions describe the forces exerted on the interface. They are made of three differential equations, describing the normal stress and the tangential stresses at the interface. The normal stress at the free surface is equal to the mean curvature $\nabla.\overrightarrow{n}$. This yields

$$\overrightarrow{n}.\overrightarrow{T}.\overrightarrow{n} = \sigma\nabla.\overrightarrow{n}, \tag{2.75}$$

in which σ is the surface tension and $\overrightarrow{T}$ is the viscous stress tensor. For the flow of an axisymmetric incompressible Newtonian liquid T is given by

$$T = \begin{bmatrix} -P + 2\mu\frac{\partial u_r}{\partial r} & \mu\frac{\partial u_\theta}{\partial r} & \mu(\frac{\partial u_r}{\partial z} + \frac{\partial u_z}{\partial r}) \\ \mu\frac{\partial u_\theta}{\partial r} & -P & \mu\frac{\partial u_\theta}{\partial z} \\ \mu(\frac{\partial u_r}{\partial z} + \frac{\partial u_z}{\partial r}) & \mu\frac{\partial u_\theta}{\partial z} & -P + 2\mu\frac{\partial u_z}{\partial z} \end{bmatrix}.$$

Developing Equation 2.75 yields

$$\frac{2\mu\left(\left(\frac{\partial h}{\partial r}\right)^2\frac{\partial u_r}{\partial r} - \frac{\partial u_r}{\partial z}\frac{\partial h}{\partial r} - \frac{\partial h}{\partial r}\frac{\partial u_z}{\partial r} + \frac{\partial u_z}{\partial z}\right)}{1 + \left(\frac{\partial h}{\partial r}\right)^2} = \frac{\frac{\sigma}{r}\left(r\frac{\partial^2 h}{\partial r^2} + \frac{\partial h}{\partial r}\right) + \frac{\sigma}{r}\left(\frac{\partial h}{\partial r}\right)^3}{\sqrt{1 + \left(\frac{\partial h}{\partial r}\right)^2}} + P \tag{2.76}$$

RBD assumed that there are no shear forces at the surface of the film; this mathematically translates to

$$\overrightarrow{n}.\overrightarrow{T}.\overrightarrow{t_r} = 0 \tag{2.77}$$

and

$$\overrightarrow{n}.\overrightarrow{T}.\overrightarrow{t_\theta} = 0. \tag{2.78}$$

Developing Equation 2.77 and Equation 2.78 yields

$$-2\mu\left(\frac{\partial h}{\partial r}\frac{\partial u_r}{\partial r} + \frac{\partial h}{\partial r}\frac{\partial u_z}{\partial z}\right)\left(1 + \left(\frac{\partial h}{\partial r}\right)^2\right)^{-1} + \mu\left(\frac{\partial u_r}{\partial z} + \frac{\partial u_z}{\partial r}\right) = 0 \tag{2.79}$$

and

$$-\frac{\partial h}{\partial r}\frac{\partial u_\theta}{\partial r} + \frac{\partial u_\theta}{\partial z} = 0. \tag{2.80}$$

2.3.3.2 Lubrication theory

The analytical resolution of the Navier-Stokes equations is complicated. In order to simplify the calculations RBD applied a lubrication theory; this theory is applicable when studying the flow of a fluid in a geometry in which one dimension is significantly smaller than the others. The flow in the z axis is significantly smaller than the flow in the radial axis. Applying the lubrication theory involves non-dimensionalising the Navier-Stokes equations and rewriting them as a function of the aspect ratio ε which is

equal to

$$\varepsilon = h_o/R \tag{2.81}$$

In this equation h_o is the initial thickness of the film and R is the radius of the substrate. A lubrication theory reveals which forces are dominant and which ones are negligible by highlighting their relative magnitude.

Dimensionless variables

To non-dimensionalise the governing equations we need to define new velocity scales and length scales. The radius of the substrate and the initial film thickness are used to scale the flow in the radial direction and in the vertical direction. We define

$$r = Rr^*, \qquad \theta = \theta^*, \qquad z = h_o z^*, \qquad h = h_o h^* \text{ and} \qquad t = T_o t^*, \tag{2.82}$$

where $T_o = R/U$, is the time scale, U the radial velocity scale and * denotes the dimensionless variables. The balance between the centrifugal forces and the viscous forces suggests a radial velocity scale U equal to $\frac{\omega^2 L h_0}{\nu}$. Therefore the radial velocity is expressed as

$$u_r = U u_r^* = \frac{\omega^2 R h_o}{\nu} u_r^*. \tag{2.83}$$

Similarly we define the azimuthal velocity scale, V, the axial velocity scale, W and the pressure scale P_o such as

$$u_\theta = V u_\theta^*, \quad u_z = W u_z^*, \text{and} \quad P = P_o P^*. \tag{2.84}$$

The scaling parameters P_o and V are deducted from the non-dimensionalisation of the radial component and the azimuthal component of the Navier-Stokes equations. The axial velocity scale W, will be deduced from the non- dimensionalisation of the continuity equation.

Non-dimensionalisation of the continuity equation

Using the defined length scales and the velocity scales Equation 2.69 can be rewritten as

$$\frac{1}{Rr^*}\frac{\partial}{\partial(Rr^*)}(Rr^*Uu_r^*) + \frac{\partial Wu_z^*}{\partial(h_o z^*)} = 0. \tag{2.85}$$

In order to respect Equation 2.85, the axial W velocity scale has to be equal to $W = \frac{h_o U}{R}$. The continuity equation can thus be rewritten as

$$\frac{1}{r^*}\frac{\partial}{\partial r^*}(r^*u_r^*) + \frac{\partial u_z^*}{\partial z^*} = 0. \tag{2.86}$$

Non-dimensionalisation of the radial component of the Navier-Stokes equation

Using the defined length scales and the velocity scales Equation 2.64 can be rewritten as

$$\begin{aligned}\rho\left[\frac{U^2}{R}\frac{\partial u_r^*}{\partial t^*} + \frac{U^2}{R}u_r^*\frac{\partial u_r^*}{\partial r^*} - \frac{V^2}{R}\frac{u_\theta^{*2}}{r^*} + \frac{WU}{h_o}u_z^*\frac{\partial u_r^*}{\partial z^*}\right] &= \mu\left[\frac{U}{R^2}\left(\frac{1}{r^*}\frac{\partial}{\partial r^*}\left(r^*\frac{\partial u_r^*}{\partial r^*}\right) - \frac{u_r^*}{r^{*2}}\right)\right] \\ &+\frac{\mu U}{h_o^2}\frac{\partial^2 u_r^*}{\partial z^{*2}} - \frac{P_o}{R}\frac{\partial P^*}{\partial r^*} \\ &+2\rho\omega V u_\theta^* + \rho R r^*\omega^2. \end{aligned} \tag{2.87}$$

In order to balance the pressure term in Equation 2.87, the pressure scale P_o is defined as

$$P_o = \frac{\mu U R}{h_o^2} \tag{2.88}$$

and the azimuthal velocity scale is equal to

$$V = \frac{U\omega h_o^2}{\nu}. \tag{2.89}$$

Equation 2.89 will become obvious in the non-dimensionalisation of the azimuthal component. Substituting P_o and V into Equation 2.87 and multiplying through with $\frac{h_o^2}{\mu U}$ yields,

$$\begin{aligned}\frac{Uh_o^2}{\nu R}\left[\frac{\partial u_r^*}{\partial t^*} + u_r^*\frac{\partial u_r^*}{\partial r^*} + u_z^*\frac{\partial u_r^*}{\partial z^*}\right] &= -\frac{\partial P^*}{\partial r^*} + \frac{h_o^2}{R^2}\left(\frac{1}{r^*}\frac{\partial}{\partial r^*}\left(r^*\frac{\partial u_r^*}{\partial r^*}\right) - \frac{u_r^*}{r^{*2}}\right) \\ &+\frac{\partial^2 u_r^*}{\partial z^{*2}} + \frac{U^2 h_o^4}{\nu^2 R^2}\frac{u_\theta^{*2}}{r^*} + 2\frac{\omega^2 h_o^4}{\nu^2}u_\theta^* + r^*. \end{aligned} \tag{2.90}$$

The Reynolds number Re which compares the inertial forces to the viscous forces is given by

$$\mathrm{Re} = \frac{U h_o}{\nu}. \tag{2.91}$$

Factorising Equation 2.90 with Re yields,

$$\begin{aligned} \epsilon \mathrm{Re}\left[\frac{\partial u_r^*}{\partial t^*} + u_r^*\frac{\partial u_r^*}{\partial r^*} + u_z^*\frac{\partial u_r^*}{\partial z^*}\right] &= -\frac{\partial P^*}{\partial r^*} + \epsilon^2\left(\frac{1}{r^*}\frac{\partial}{\partial r^*}\left(r^*\frac{\partial u_r^*}{\partial r^*}\right) - \frac{u_r^*}{r^{*2}}\right) \\ &\quad + \frac{\partial^2 u_r^*}{\partial z^{*2}} + \epsilon^2 \mathrm{Re}^2\frac{u_\theta^{*2}}{r^*} + 2\epsilon \mathrm{Re} u_\theta^* + r^*. \end{aligned} \tag{2.92}$$

.

Non-dimensionalisation of the azimuthal component of the Navier-Stokes equation

Using the characteristic length scales and the velocity scales. Equation 2.66 can be rewritten as

$$\begin{aligned} \rho\left[\frac{V}{\tau}\frac{\partial u_\theta^*}{\partial t^*} + \frac{VU}{R}u_r^*\frac{\partial u_\theta^*}{\partial r^*} + \frac{VU}{R}\frac{u_r^* u_\theta^*}{r^*} + \frac{WV}{h_o}u_z^*\frac{\partial u_\theta^*}{\partial z}\right] &= \frac{\mu V}{R^2}\frac{1}{r^{*2}}\frac{\partial}{\partial r^*}\left(r^{*3}\frac{\partial}{\partial r^*}\left(\frac{u_\theta^*}{r^*}\right)\right) \\ &\quad + \frac{\mu V}{h_o^2}\frac{\partial^2 u_\theta^*}{\partial z^{*2}} - 2\rho\omega U u_r^*. \end{aligned} \tag{2.93}$$

Multiplying both sides of Equation 2.93 by $\frac{1}{\omega U \rho}$ yields

$$\begin{aligned} \epsilon \mathrm{Re}\left[\frac{\partial u_\theta^*}{\partial t^*} + u_r^*\frac{\partial u_\theta^*}{\partial r^*} + \frac{u_r^* u_\theta^*}{r^*} + u_z^*\frac{\partial u_\theta^*}{\partial z^*}\right] &= \epsilon^2\frac{1}{r^{*2}}\frac{\partial}{\partial r^*}\left(r^{*3}\frac{\partial}{\partial r^*}\left(\frac{u_\theta^*}{r^*}\right)\right) \\ &\quad + \frac{\partial^2 u_\theta^*}{\partial z^{*2}} - 2u_r^*. \end{aligned} \tag{2.94}$$

The azimuthal velocity scale V is determined by balancing the last term of Equation 2.93.

Non-dimensionalisation of the axial component of the Navier-Stokes equation

After substituting the velocity scales and the length scales, Equation 2.68 gives

$$\rho\left[\frac{W}{\tau}\frac{\partial u_z^*}{\partial t^*}+\frac{UW}{R}u_r^*\frac{\partial u_z^*}{\partial r^*}+\frac{W^2}{h_o}u_z^*\frac{\partial u_z^*}{\partial z^*}\right] = -\frac{P_o}{h_o}\frac{\partial P^*}{\partial z^*}+\mu\frac{W}{R^2}\frac{1}{r^*}\frac{\partial u_z^*}{\partial r^*}+\frac{\mu W}{R^2}\frac{\partial^2 u_z^*}{\partial r^{*2}} +\frac{\mu W}{h_o^2}\frac{\partial^2 u_z^*}{\partial z^{*2}}-\rho g. \tag{2.95}$$

Multiplying both sides of Equation 2.95 by $\frac{h_o^3}{RU\mu}$ yields,

$$\epsilon^3\mathrm{Re}\left[\frac{\partial u_z^*}{\partial t^*}+u_r^*\frac{\partial u_z^*}{\partial r^*}+u_z^*\frac{\partial u_z^*}{\partial z^*}\right] = -\frac{\partial P^*}{\partial z^*}+\epsilon^4\left[\frac{1}{r^*}\frac{\partial u_z^*}{\partial r^*}+\frac{\partial^2 u_z^*}{\partial r^{*2}}\right]+\epsilon^2\frac{\partial^2 u_z^*}{\partial z^{*2}} -\epsilon\mathrm{Re}F^{-2}. \tag{2.96}$$

In Equation 2.96, F is the Froude number which is expressed as

$$F=\sqrt{\frac{U}{gh_o}^2}. \tag{2.97}$$

The Froude number is a dimensionless number which compares the inertial and the gravitational forces.

Non-dimensionalisation of the boundary conditions at the free surface

Introducing the scaled variables into the kinematic boundary condition 2.74, gives

$$\left(\frac{\partial h}{\partial t}+u_r\frac{\partial h}{\partial r}-u_z\right)\left(1+\left(\epsilon\frac{\partial h}{\partial r}\right)^2\right)^{-1/2}=-\frac{3E}{2}. \tag{2.98}$$

In this equation E is the dimensionless evaporation rate and is equal to $\frac{3J}{2\epsilon U}$.

Using the scaled variables and dividing both sides by $\rho\omega^2 R^2$, Equation 2.76, which expresses the normal stress at the film/air interface can be rewritten as:

$$-\frac{P_o P^*}{\rho\omega^2 R^2} = \frac{-2\mu\frac{U_o}{\rho\omega^2 R^3}\left(\left(\frac{h_o}{R}\frac{\partial h^*}{\partial r^*}\right)^2\frac{\partial u_r^*}{\partial r^*} - \frac{\partial h}{\partial r}\frac{\partial u_r^*}{\partial z^*} - \left(\frac{h_o}{R}\right)^2\frac{\partial h^*}{\partial r^*}\frac{\partial u_z^*}{\partial r^*} + \frac{\partial u_z^*}{\partial z^*}\right)}{1+\left(\frac{h_o}{R}\frac{\partial h^*}{\partial r^*}\right)^2} + \frac{\frac{\sigma}{r^*}\frac{h_o}{\rho\omega^2 R^4}\left(r^*\frac{\partial^2 h^*}{\partial r^{*2}} + \frac{\partial h^*}{\partial r^*} + \left(\frac{h_o}{R}\right)^2\left(\frac{\partial h^*}{\partial r^*}\right)^3\right)}{\sqrt{1+\left(\frac{h_o}{R}\frac{\partial h^*}{\partial r^*}\right)^2}}. \tag{2.99}$$

the previous equation is equivalent to

$$-P = \frac{-2\epsilon^2\left(\left(\epsilon\frac{\partial h^*}{\partial r^*}\right)^2\frac{\partial u_r^*}{\partial r^*} - \frac{\partial h}{\partial r}\frac{\partial u_r^*}{\partial z^*} - \epsilon^2\frac{\partial h^*}{\partial r^*}\frac{\partial u_z^*}{\partial r^*} + \frac{\partial u_z^*}{\partial z^*}\right)}{1+\epsilon^2\left(\frac{\partial h^*}{\partial r^*}\right)^2} + \frac{\epsilon^3\frac{\kappa}{r^*}\left(r^*\frac{\partial^2 h^*}{\partial r^{*2}} + \frac{\partial h^*}{\partial r^*} + \epsilon^2\left(\frac{\partial h^*}{\partial r^*}\right)^3\right)}{\sqrt{1+\epsilon^2\left(\frac{\partial h^*}{\partial r^*}\right)^2}}. \tag{2.100}$$

In Equation 2.100, κ is the Weber number and is equal to

$$\kappa = \frac{\sigma}{\rho\omega^2 R h_o^2}. \tag{2.101}$$

The Weber number is a dimensionless number which compares the relative magnitude of the inertial forces to the surface tension forces.

After introducing the scaled variables, Equation 2.79 which represents the radial shear stress at the free surface can be rewritten as:

$$\frac{2\mu\frac{h_o U_o}{R^2}\frac{\partial h^*}{\partial r^*}\left(\frac{\partial u_z^*}{\partial z^*} - \frac{\partial u_r^*}{\partial r^*}\right)}{1+\left(\frac{h_o}{R}\frac{\partial h^*}{\partial r^*}\right)^2} + \mu\left(\frac{U_o}{h_o}\frac{\partial u_r^*}{\partial z^*} + \frac{h_o U_o}{R^2}\frac{\partial u_z^*}{\partial r^*}\right) = 0. \tag{2.102}$$

Multiplying Equation 2.102 through with $h_o[1+[\frac{\partial h^*}{\partial r^*}]^2]$ and eliminating μU_o we obtain

$$2\epsilon^2\frac{\partial h^*}{\partial r^*}\left(\frac{\partial u_z^*}{\partial z^*}-\frac{\partial u_r^*}{\partial r^*}\right)+\left(\frac{\partial u_r^*}{\partial z^*}+\epsilon^2\frac{\partial u_z^*}{\partial r^*}\right)\left(1+\left(\epsilon^2\frac{\partial h^*}{\partial r^*}\right)^2\right)=0. \tag{2.103}$$

Substituting the scaled variables and multiplying both sides by h_o, Equation 2.80 which expresses the azimuthal shear forces becomes

$$-\epsilon^2\frac{\partial h^*}{\partial r^*}\frac{\partial u_\theta^*}{\partial r^*}+\frac{\partial u_\theta^*}{\partial z^*}=0. \tag{2.104}$$

Equations 2.86, 2.92, 2.94 and 2.96 form the governing equations rewritten in terms of the scaled variables. Equations 2.98, 2.100, 2.103 and 2.104 are the scaled boundary conditions.

2.3.3.3 Perturbation theory

To study the flow at the early stage of the coating where the Reynolds number is low and the flow laminar, the variables in the scaled governing equations and the scaled boundary conditions are expanded into powers of ϵ,

$$\overrightarrow{u}^* = (u_r^{*(0)}+\epsilon u_r^{*(1)}, u_\theta^{*(0)}+\epsilon u_\theta^{*(1)}, u_z^{*(0)}+\epsilon u_z^{*(1)}) \tag{2.105}$$

$$\overrightarrow{P}^* = (0,0,P^{*(0)}+\epsilon P^{*(1)}). \tag{2.106}$$

A system of equations is then formed by expressing the lowest order and the ϵ order of the scaled governing equations and the scaled boundary conditions.

Expanding all the variables in power of ϵ, and taking the lowest order of the scaled form of continuity equation (2.86) we obtain

$$\frac{1}{r^*}\frac{\partial}{\partial r^*}(r^*u_r^{*(0)})+\frac{\partial u_z^{*(0)}}{\partial z^*}=0. \tag{2.107}$$

Expanding all the variables in powers of ϵ, and taking the lowest order of the scaled radial component (Equation 2.92), the scaled azimuthal component (Equation 2.94) and the scaled axial component (Equation 2.96), the Navier-Stokes equations can be rewritten as

$$-\frac{\partial P^{*(0)}}{\partial r^*}+\frac{\partial^2 u_r^{*(0)}}{\partial z^{*2}}+r^*=0, \tag{2.108}$$

$$\frac{\partial^2 u_\theta^{*(0)}}{\partial z^{*2}} - 2u_r^{*(0)} = 0, \tag{2.109}$$

and

$$\frac{\partial P^{*(0)}}{\partial z^*} = 0. \tag{2.110}$$

Similarly the lowest order of no-slip condition (equations 2.70, 2.71 and 2.72) gives

$$u_r^{*(0)} = 0, \tag{2.111}$$

$$u_\theta^{*(0)} = 0, \tag{2.112}$$

and

$$u_z^{*(0)} = 0. \tag{2.113}$$

The lowest order of the scaled kinematic boundary condition (Equation 2.98) at the free surface gives

$$\frac{\partial h^*}{\partial t^*} + u_r^{*(0)}\frac{\partial h^*}{\partial r^*} - u_z^{*(0)} = -\frac{3E}{2}, \tag{2.114}$$

Expanding all the variables in power of ϵ, and taking the lowest order, the scaled dynamic boundary conditions (equations 2.100, 2.103 and 2.104) at the free surface can be rewritten as

$$P^{*(0)} = 0, \tag{2.115}$$

$$\frac{\partial u_r^{*(0)}}{\partial z} = 0 \tag{2.116}$$

and

$$\frac{\partial u_\theta^{*(0)}}{\partial z} = 0. \tag{2.117}$$

Expanding all the variables in powers of ϵ, and taking the ϵ order of the scaled continuity equation (2.86) gives

$$\frac{1}{r^*}\frac{\partial}{\partial r^*}(r^* u_r^{*(1)}) + \frac{\partial u_z^{*(1)}}{\partial z^*} = 0. \tag{2.118}$$

Similarly the ϵ order of the radial component (Equation 2.92), the azimuthal component (Equation 2.94) and the axial component (Equation 2.96) of the Navier-Stokes equations can be rewritten as

$$\mathrm{Re}\left[\frac{\partial u_r^{*(0)}}{\partial t^*} + u_r^{*(0)}\frac{\partial u_r^{*(0)}}{\partial r^*} + u_z^{*(0)}\frac{\partial u_r^{*(0)}}{\partial z^*}\right] = -\frac{\partial P^{*(1)}}{\partial r^*} + \frac{\partial^2 u_r^{*(1)}}{\partial z^{*2}} + 2\mathrm{Re}u_\theta^{*(0)}, \tag{2.119}$$

$$\mathrm{Re}\left[\frac{\partial u_\theta^{*(0)}}{\partial t^*} + u_r^{*(0)}\frac{\partial u_\theta^{*(0)}}{\partial r^*} + \frac{u_r^{*(0)}u_\theta^{*(0)}}{r^*} + u_z^{*(0)}\frac{\partial u_\theta^{*(0)}}{\partial z^*}\right] = \frac{\partial^2 u_\theta^{*(1)}}{\partial z^{*2}} - 2u_r^{*(1)}, \tag{2.120}$$

and

$$\frac{\partial P^{*(1)}}{\partial z^*} + \mathrm{Re}F^{-2} = 0. \tag{2.121}$$

The ϵ order of the no-slip boundary condition (equations 2.70, 2.71 and 2.72) gives

$$u_r^{*(1)} = 0, \tag{2.122}$$

$$u_\theta^{*(1)} = 0, \tag{2.123}$$

and

$$u_z^{*(1)} = 0. \tag{2.124}$$

The ϵ order of the scaled kinematic boundary conditions (Equation 2.98) gives

$$u_r^{*(0)}\frac{\partial h^*}{\partial r^*} - u_z^{*(0)} = 0. \tag{2.125}$$

The ϵ order of the scaled dynamic boundary conditions (equations 2.100, 2.103 and 2.104) are expressed as

$$P^{*(1)} = \frac{\kappa}{r}\left(r\frac{\partial^2 h^*}{\partial r^{*2}} + \frac{\partial h^*}{\partial r^*}\right), \tag{2.126}$$

$$\frac{\partial u_r^{*(1)}}{\partial z} = 0, \tag{2.127}$$

and

$$\frac{\partial u_\theta^{*(1)}}{\partial z} = 0. \tag{2.128}$$

Equations 2.107 to 2.128 are solved for $u_r^{*(0)}$, $u_r^{*(1)}$, $u_\theta^{*(0)}$, $u_\theta^{*(1)}$, $u^{*(0)}$, $u_r^{*(1)}$,$P^{*(0)}$ and $P^{*(1)}$. Equation 2.110 is solved subject to condition 2.115 giving a pressure equal to

$$P^{*(0)} = 0. \tag{2.129}$$

We substitute Equation 2.129 in Equation 2.108. The latter is then solved for $u_r^{*(0)}$ subject to conditions 2.111 and 2.116. The lowest order of the radial velocity is equal to:

$$u_r^{*(0)} = \frac{1}{2}r^*z^*(2h^* - z^*). \tag{2.130}$$

Equation 2.130 is substituted in Equation 2.109, which is solved for $u_\theta^{*(0)}$ subject to conditions 2.112 and 2.117. This calculation leads to

$$u_\theta^{*(0)} = \frac{1}{12} r^* z^* (4z^{*2} - z^{*3} - 8h^{*3}). \tag{2.131}$$

Equation 2.130 is substituted in Equation 2.107 which is solved for $u_z^{*(0)}$ subject to conditions 2.113. The lowest order of the axial velocity is expressed as

$$u_z^{*(0)} = \frac{1}{6} z^{*2} (2z^* - 3r^* \frac{\partial h^*}{\partial r^*} - 6h^*). \tag{2.132}$$

Equation 2.121 is solved for the $P^{*(1)}$, subject to condition 2.126. The ϵ order of the pressure is equal to

$$P^{*(1)} = \mathrm{Re} F^{-2} (h^* - z^*) - \frac{T}{r^*} \left(r^* \frac{\partial^2 h^*}{\partial z^{*2}} - \frac{\partial h^*}{\partial r^*} \right). \tag{2.133}$$

Equation 2.133 is substituted into Equation 2.119; which is solved for $u_r^{*(1)}$ subject to condition 2.127, and 2.122 gives

$$\begin{aligned} u_r^{(1)} \quad = \quad & \mathrm{Re} \Bigg[-z^* \left(\frac{3}{5} r^* h^{*5} + \frac{1}{2} r^* h^{*2} \frac{\partial h^*}{\partial t^*} + \frac{1}{6} r^{*2} h^{*4} \frac{\partial h^*}{\partial r^*} + F^{-2} h^* \frac{\partial h^*}{\partial r^*} - T \mathrm{Re}^{-1} h^* \left[\frac{\partial^3 h^*}{\partial r^{*3}} \right. \right. \\ & \left. + r^{*-2} \left(r \frac{\partial^2 h^*}{\partial h^{*2}} - \frac{\partial h^*}{\partial r^*} \right) \right] \Bigg) + z^{*2} \left(\frac{1}{2} F^{-2} \frac{\partial h^*}{\partial r^*} - \frac{1}{2} T \mathrm{Re}^{-1} \left[\frac{\partial^3 h^*}{\partial r^{*3}} + r^{*-2} \left(r \frac{\partial^2 h^*}{\partial r^{*2}} \right. \right. \right. \\ & \left. \left. \left. - \frac{\partial h^*}{\partial r^*} \right) \right] \right) + z^{*3} \left(\frac{1}{6} r^* \frac{\partial h^*}{\partial t^*} + \frac{2}{9} r^* h^{*3} \right) + \frac{1}{360} r^* z^{*6} - \frac{1}{60} r^* z^{*5} h^* \\ & \left. + \frac{1}{24} r^{*2} z^{*4} h^* \frac{\partial h^*}{\partial r^*} \right]. \end{aligned} \tag{2.134}$$

Equation 2.134 is substituted in Equation 2.120. This latter equation is then solved for $u_\theta^{*(1)}$ subject to condition 2.127 and 2.123. This yields

$$\begin{aligned} u_\theta^{(1)} &= \mathrm{Re}\Bigg[z\left(\frac{68}{105}r^*h^{*7}+\frac{4}{3}r^*h^{*4}\frac{\partial h^*}{\partial t^*}+\frac{22}{45}r^*h^{*6}\frac{\partial h^*}{\partial r^*}+\frac{2}{3}F^{-2}h^{*3}\frac{\partial h^*}{\partial r^*}-\frac{2}{3}T\mathrm{Re}^{-1}h^*\right. \\ &\left.\left[\frac{\partial^3 h^*}{\partial r^*}+r^{*-2}\left(r\frac{\partial^2 h^*}{\partial r^{*2}}-\frac{\partial h^*}{\partial r^*}\right)\right]\right)-z^{*3}\left(\frac{1}{5}h^{*5}+\frac{1}{2}h^{*2}\frac{\partial h^*}{\partial t^*}+\frac{1}{18}r^{*2}h^{*4}\frac{\partial h^*}{\partial r^*}\right. \\ &+\frac{1}{3}F^{-2}h^*\frac{\partial h^*}{\partial r^*}-\frac{1}{3}T\mathrm{Re}^{-1}h^*\left[\frac{\partial^3 h^*}{\partial r^{*3}}+r^{*-2}\left(r\frac{\partial^2 h^*}{\partial r^{*2}}-\frac{\partial h^*}{\partial r^*}\right)\right]\Bigg)-z^{*5}\left(\frac{1}{30}r^*\frac{\partial h^*}{\partial t^*}\right. \\ &\left.+\frac{1}{20}r^{*2}h^{*2}\frac{\partial h^*}{\partial r^*}\right)-z^{*6}\left(\frac{1}{90}r^*h^{*2}+\frac{1}{360}r^{*2}h^*\frac{\partial h^*}{\partial r^*}\right)-\frac{1}{2520}r^*z^{*8} \\ &\left.-\frac{1}{315}r^*z^{*7}h^*\right]. \end{aligned} \tag{2.135}$$

Equation 2.118 is solved for $u_z^{*(1)}$ subject to condition 2.124. This give rise to the following expression of the ϵ order of the axial velocity

$$\begin{aligned} u_z^{(1)} &= \mathrm{Re}\Bigg[z^{*2}\left(\frac{3}{5}h^{*5}+\frac{1}{2F}\frac{\partial h}{\partial r^*}^{*2}+\frac{1}{2}h^{*2}\frac{\partial h^*}{\partial t^*}+\frac{1}{F^{-2}2r^*}h^*\frac{\partial h^*}{\partial r^*}+\frac{1}{4}r^*h^{*2}\frac{\partial^2 h^*}{\partial r^*\partial t^*}\right. \\ &+\frac{7}{4}r^*h^{*4}\frac{\partial h^*}{\partial r^*}+\frac{1}{3}r^{*2}h^{*3}\frac{\partial h}{\partial r^*}^{*2}+\frac{1}{12}r^{*2}h^{*4}\frac{\partial^2 h^*}{\partial r^{*2}}+\frac{1}{2F^{-2}}h\frac{\partial^2 h^*}{\partial r^{*2}}+\frac{1}{2}h^*\frac{\partial h^*}{\partial r^*}\frac{\partial h^*}{\partial t^*} \\ &-\frac{T}{\mathrm{Re}}\left(\frac{1}{2r^*}h^*\frac{\partial^3 h^*}{\partial r^{*3}}+\frac{1}{2}\frac{\partial h^*}{\partial r^*}\frac{\partial^4 h^*}{\partial r^{*4}}+\frac{1}{2}h^*\frac{\partial^3 h^*}{\partial r^{*3}}+\frac{1}{2r^{*2}}\left(r^*\frac{\partial^2 h^*}{\partial r^{*2}}-\frac{\partial h^*}{\partial r^*}\right)\frac{\partial h^*}{\partial r^*}\right. \\ &\left.+\frac{1}{2r^{*3}}h^*\left(r^{*2}\frac{\partial^3 h^*}{\partial r^{*3}}-r^*\frac{\partial^2 h^*}{\partial r^{*2}}+\frac{\partial h^*}{\partial h}\right)\right)-z^3\left(\frac{1}{F^{-2}}\left(\frac{1}{6}\frac{\partial h}{\partial r}+\frac{1}{6}\frac{\partial^2 h^*}{\partial r^{*2}}\right)-\frac{T}{\mathrm{Re}^{-1}}\right. \\ &\left.\left(\frac{1}{6r}\frac{\partial^3 h^*}{\partial r^{*3}}+\frac{1}{6}\frac{\partial^4 h^*}{\partial r^{*4}}+\frac{1}{6r^{-3}}\left(r^{*2}\frac{\partial^3 h^*}{\partial r^{*3}}-r\frac{\partial^2 h^*}{\partial r^{*2}}+\frac{\partial h^*}{\partial r^*}\right)\right)\right)-z^4\left(\frac{1}{12}\frac{\partial h^*}{\partial t^*}+\frac{1}{9}h^{*3}\right. \\ &+\frac{1}{24}r^*\frac{\partial^2 h^*}{\partial r^*\partial t^*}+\frac{1}{6}r^*h^{*2}\frac{\partial h^*}{\partial r^*}\Bigg)-z^5\left(\frac{1}{120}r^{*2}\frac{\partial^2 h^*}{\partial r^{*2}}+\frac{1}{40}r^*h^*\frac{\partial h^*}{\partial r^*}\right. \\ &\left.+\frac{1}{120}r^{*2}h\frac{\partial^2 h^*}{\partial^2 r^*}\right)+z^6\left(\frac{1}{180}h+\frac{1}{360}r\frac{\partial h}{\partial r}\right)-\frac{1}{1260}z^7\Bigg]. \end{aligned} \tag{2.136}$$

The equation of motion of spin coating is obtained by using the expanded kinematic boundary condition at the film/air interface ($z=h$)

$$\left(\frac{\partial h^*}{\partial t^*}+(u_r^{*(0)}+\epsilon u_r^{*(1)})\frac{\partial h}{\partial r}-(u_z^{*(0)}+\epsilon u_z^{*(1)})\right)\left(1+\left(\epsilon\frac{\partial h}{\partial r}\right)^2\right)^{-1/2}=-\frac{3E}{2}. \tag{2.137}$$

RBD assumed that the thickness of the film is independent of the radial position r. As a consequence, Equation 2.137 can be rewritten as

$$\frac{\partial h^*}{\partial t^*} - (u_z^{*(0)} + \epsilon u_z^{*(1)}) = \frac{3E}{2}. \tag{2.138}$$

Note that equation of motion depends only on the axial velocity of the fluid (Equation 2.132) and its ϵ order (Equation 2.136). RBD assumed that the Weber number W and the Froude number F are very small and therefore negligible. As a consequence the lowest order of the axial velocity and the corresponding ϵ order are equal to

$$u_z^{(0)}(h) = -\frac{2}{3}h^{*3}, \tag{2.139}$$

and

$$u_z^{(1)}(h) = \mathrm{Re}\left[\frac{3}{5}h^{*7} + \frac{1}{2}h^{*4}\frac{\partial h^*}{\partial t^*} - h^4\frac{1}{12}\frac{\partial h^*}{\partial t^*} - \frac{1}{9}h^{*7} + \frac{1}{180}h^7 - \frac{1}{1260}h^7\right]. \tag{2.140}$$

The equation of motion is obtained by substituting Equation 2.139 and Equation 2.140 in Equation 2.138

$$\frac{\partial h^*}{\partial t^*} + \frac{2}{3}E + \frac{2}{3}h^{*3} + \epsilon\mathrm{Re}\left[-\frac{5}{12}h^{*4}\frac{\partial h^*}{\partial t^*} - \frac{622}{1260}h^{*7}\right] = 0. \tag{2.141}$$

The time derivative of the thickness is then replaced with the first leading order of Equation 2.141: $\frac{\partial h^*}{\partial t^*} = -\frac{2}{3}E - \frac{2}{3}h^{*3}$. The thinning rate of the film is then given

$$\frac{\partial h^*}{\partial t^*} + \frac{2}{3}\left(E + h^{*3} + \epsilon\mathrm{Re}\left[\frac{5E}{12}h^{*4} - \frac{34}{105}h^{*7}\right]\right) = 0. \tag{2.142}$$

Note that this equation is identical to the equation proposed by Meyerhofer with the exception of the ϵ term. The extra term is a velocity term which account for the effect of the inertia forces.

2.3.4 Rheology of polymer solutions

2.3.4.1 Concentration dependence of the viscosity

We saw that the dimension of polymer chains is a function of the quality of the solvent. Other factors such as the molecular weight, the temperature and the concentration can lead to a change in chain dimension. The chain dimension and the distance between the chains changes the viscosity. First let's introduce the viscosity terms necessary to characterise the viscosity of a polymer solution η. The viscosity of the solvent is noted η_s. The relative viscosity compares the viscosity of the solvent to the viscosity of a polymer solution and is expressed as

$$\eta_r = \frac{\eta}{\eta_s}. \tag{2.143}$$

The specific viscosity expressed as

$$\eta_{sp} = \eta_r - 1 \tag{2.144}$$

quantifies the increment in the viscosity due to the presence of the polymer. The reduced viscosity η_{red} is a measure of the specific capacity of the polymer to increase the relative viscosity and is expressed as

$$\eta_{red} = \frac{\eta_{sp}}{c}. \tag{2.145}$$

The limit of the specific viscosity as the concentration tends to zero is the intrinsic viscosity

$$[\eta] = \lim_{c \to \infty} \quad \eta_{red}. \tag{2.146}$$

The intrinsic viscosity measures the ability of the polymer chain to increase the viscosity in a solution with no intermolecular interactions. The intrinsics viscosity is related to the molecular weight by the Mark-Houwink equation

$$[\eta] = KM^z \tag{2.147}$$

K and z are constant called the Mark-Houwink parameters. They have specific values for a given polymer solvent mixture. Equation 2.147 is used to determine the molecular weight of polymers.

(a) (b) (c)

FIGURE 2.16: Diagram showing the chain conformation as the concentration of the polymer increases. (a) shows the chain's conformation in the dilute regime when the chains don't interact. (b) shows the chain's conformation at the starts of the dilueted regim where the chain start to overlap. (c) shows the conformation of the chain in the concentrated regime where the chains interpenate

In a good solvent the excluded volume is positive and the polymer chains act like independent coils with no interaction between them (see Figure 2.16 (a)). The solution is said to be in the dilute regime. Each chain contributes to the increase in the viscosity and the viscosity changes linearly with the polymer concentration. In the dilute regime the relative viscosity is expressed as

$$\eta_{sp} = [\eta]\, c. \tag{2.148}$$

As the polymer concentration increases at a given concentration called the overlap concentration c^* the polymer coil starts to overlap despite the positive excluded volume. c^* is the volume fraction of a single polymer chain inside its pervaded volume and is expressed as

$$c^* = \frac{3M}{4\pi Rg^3 N_A} \tag{2.149}$$

When the $c > c^*$ the solution is said to be in the semidilute regime. In a semidiluted solution the polymer chains still have some degree of freedom but the increase in density leads to a reduction in the mobility of the chains and some of the polymer chains interpenetrate. In this regime the specific viscosity is expressed as

$$\eta_{sp} = [\eta]\, c + k_h\, [\eta]^2\, c^2. \tag{2.150}$$

Once the concentration of the solution reaches a concentration c^{**} the solution is in the

concentrated regime. In this regime the concentration of the solution is so high that the excluded volume is screened and the polymer chains behave like ideal chains. The relative viscosity depends on the polymer concentration given by the equation following equation

$$\eta = kc^{\alpha} M_w^{\beta}, \tag{2.151}$$

where k, α and β are constants.

2.3.4.2 Newtonian and Non-Newtonian behavior during spin coating

Highly concentrated polymer solutions can exhibit non-Newtonian behaviour i.e.the viscosity is not linearly dependent on the shear rate. Ostwald [48] was the first to correlate mathematically the shear rate and the viscosity of non-Newtonian solutions with the expression

$$\eta = K\dot{\gamma}^{n-1}, \tag{2.152}$$

in which $\dot{\gamma}$ is the shear rate, K is a constant and n is the power law index, which is a dimensionless quantity that measures the deviation of the flow from a Newtonian solution. In recognition of Ostwald's work Equation 2.152 is called the Ostwald power law. For $n = 1$ the flow is Newtonian. For $n < 1$ the viscosity of the fluid decreases with increasing shear rate; this is referred to as shear thinning. For $n > 1$ the viscosity increases with increasing shear rate; this is referred to as shear thickening. Spin coating of non-Newtonian fluid has been investigated by numerous groups. In 1960 Acrivos *et al.* [49] studied the thickness changes in the radial direction during the spin coating of a non-Newtonian fluid. They used the equation motion proposed by EBP (Equation 2.43) combined with the Ostwald power law. The results predicted a radial profile with a spike at the centre. This is in contradiction with the flat film obtained experimentally. Two decades later Jenekhe [50] carried a similar investigation, studying the effect of the initial radial thickness profile on the uniformity of the dry film. He examine the thinning of a non-Newtonian fluid with an initially uniform, sinusoidal (periodically wavy surface) and a Gaussian radial profile. Two viscosity laws were examined, the Ostwald power law and the the Carreau model [51], this latter relates the viscosity and the shear rate by the following equation:

$$\eta = \eta_o \left[1 + \left(\lambda\dot{\gamma}\right)^2\right]^{\frac{n-1}{2}}. \tag{2.153}$$

Here λ is a characteristic time constant and n is the power law index. Figure 2.17 shows Jenerke's results for films with initial radial profile describe by a sinusoidal (see Figure 2.17 (a) and (b)) and a Gaussian (see Figure 2.17 (c) and (d)). The radial profiles are plotted for $n = 0.20$ and $n = 0.60$. In this figure h^* is the normalised thickness and r^* is the normalised radial position. r^*=0 is defined as the center of the film. The predicted thickness profiles obtained using the power law are similar to those reported by Acrivos *et al.* [49]. This is explained by the fact that the shear rate increases when moving outward from the centre of the wafer and the power law predicts infinite viscosity at low shear rates; the film therefore does not thin in the centre and this results in a spike. Nonetheless the width of the spike decreases when the power law index is closer to 1. Regardless of the power law index, the radial thickness profiles predicted with the Carreau model are uniform. The Carreau model predicts Newtonian behaviour at low shear rates and power law at high shear rates.

The Carreau model [51] is more appropriate to describe the viscosity of non-Newtonian fluids. Jenekhe [50] measured the viscosity of highly viscous polymer solutions as a function of the shear rate. He showed that beyond a certain value of the shear rate the viscosity decreases with increasing shear rate. On the contrary, Lai[52] studied the rheology of highly diluted polymer solutions and did not observe non-Newtonian behaviour. To perform an accurate study of the spin coating of a highly concentrated polymer solutions, it is necessary to use one of the non-Newtonian viscosity laws. The Meyerhofer model and the Reisfeld model are applicable when spin coating diluted polymer solutions.

2.3.5 A review of the modelling of spin coating

As previously mentioned the first model describing spin casting was proposed by EBP [1]. Using this model they showed that the profile of the dry film is uniform regardless of the initial thickness profile. Meyerhofer [2] used his model to predict the final thickness of films cast from solutions of different polymer concentrations at different spin speeds. Figure 2.18 shows that the modelled thicknesses are in excellent agreement with the experimental thicknesses. He also proposed the following equation to relate the final thickness to the spin speed $h_f \propto w^{-0.5}$.

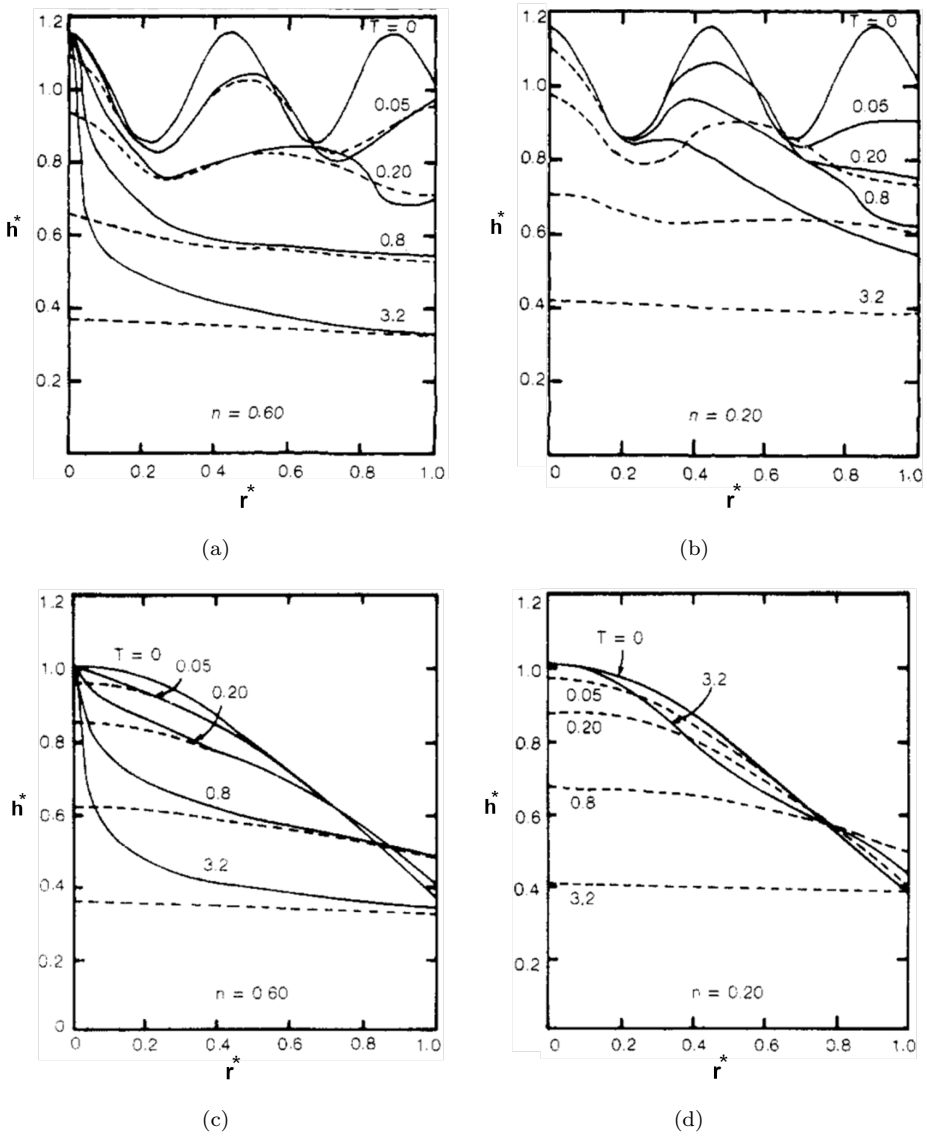

FIGURE 2.17: (a) and (b) show the Nnormalised film radial profiles for non-Newtonian fluid with an initial sinusoidal profile for n=0.20 and n=0.60. Figure (c) and (d) show the normalised film thickness profiles for non-Newtonian fluid with an initial Gaussian profile for n=0.20, and n=0.60. The dashed lines are the simulations obtained with the Carreau model and the plain line asre those obtianed with the Ostwald power law. Note that the case n=1 the flow is Newtonian. Adapted with permission from Coating flow of non-Newtonian fluids on a flat rotating disk, S. A. Jenekhe and S. B. Schuldt *Ind & Eng Chem. Fund.* **23** 432 (1984). Copyright (1984) American Chemical Society.

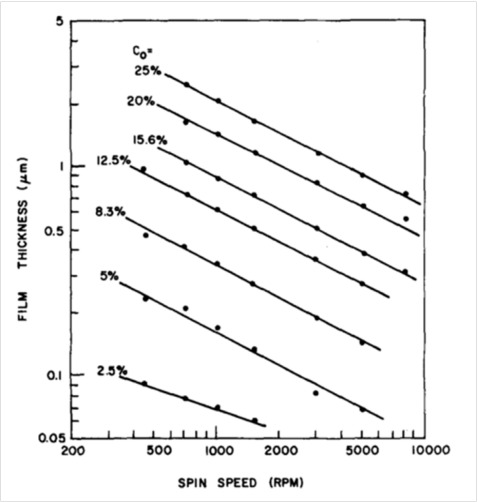

FIGURE 2.18: Measured film thicknesses as a function of the spin speed and the solute concentration. The fits to the experimental data were obtained using Equation 2.54. Reprinted from D. Meyerhofer, *J. Appl. Phys.* **43** 3393 (1978), with permission from AIP Publishing LLC

Washo [53] studied the flow of a non-volatile polymer solution rotating on a flat disk. The rheology study performed reported no non-Newtonian behaviour for the solutions studied. According to Washo, the rheology of a spun film is characterized by two regimes. Upon acceleration of the substrate the excess of material is thrown out of the surface and the volumetric flow decreases rapidly. This is the first regime which is followed by a regime where the changes in the average film thickness are negligible. This is an unrealistic model. Washo proposes the following relation to express the final thickness and to the spin speed $h_f \propto w^{-0.67}$. Lai [52] studied the morphology of thin film cast from different solvents. Prior to coating, the viscosities of the solutions were reported as a function of the shear rate and no non-Newtonian behaviour was observed. Lai was the first to report the observation of the orange peel skin for films coated from low boiling point solvents. He attributed the orange skin to the rapid evaporation of the solvent. He addressed this problem by enclosing the spin coater in a plastic box with a paper towel soaked in solvent. The orange skin could not be reduced as the chamber was not sealed properly, therefore not providing a sufficient reduction of the solvent evaporation rate. In agreement with Meyerhofer, he relates the dry film thickness to the spin speed by the following equation $h_f \propto w^{-0.50}$. Daugthon [54] showed that the film thickness is independent of the amount of solution dispensed on the substrate, on the speed of dispensation, and on the acceleration spin speed. However, the final thickness and its uniformity are strongly dependent on the final spin speed, the total spin time

and the viscosity. For the blends studied the authors find that the thickness uniformity was optimised when the solution was deposited via static dispense i.e. the substrate is immobile during the deposition of the solution.

Daugthon *et al.* reported the following dependence of the final thickness on the spin speed: $h_{\mathrm{f}} \propto w^{-0.5}$ for photoresists and $h_{\mathrm{f}} \propto w^{-0.87}$ for polyimide. In 1983 Chen *et al.* [55] carried out a study to determine the influence of the solvent evaporation on the film thickness, by coating from different solvents. This study focused on the spin coating of polymers from organic and aqueous solutions. The authors recalled that the evaporation of the solvent depends on the external conditions and on the physical properties of the solvent. The external factors include: the relative humidity, the temperature, the heat transfer (convective, conductive or radiation) and the air flow above the interface. The physical properties include relation between the vapour pressure and temperature, the thermal conductivity, the latent heat and the specific heat. The external properties were kept constant during this study, therefore observable changes on the dry film are due to the changes in the physical properties of the solvent. Thicker films were obtained by coating from solvents with high volatility. For films cast from an organic solvent the final thickness of the film can be expressed as

$$h = K_o \mu^{0.36} \omega^{-0.50} (e\lambda / C_p)^{0.60}, \tag{2.154}$$

whereas the final thickness of film cast from aqueous solutions is express as

$$h = K_o \mu^{0.36} \omega^{-0.50} (1 - R_H)^{0.60}. \tag{2.155}$$

In these equations K_o is a constant, e is the evaporation rate, C_p is the solvent specific heat capacity and R_H the relative humidity. Flacks *et al.* [56] investigated the flow of a non-Newtonian fluid taking into account the dependence of the viscosity and the diffusivity on the polymer concentration. An error in the calculation led to a radial velocity inversely proportional to the radius. This results is in disagreement with all the previous calculations; which reported a linear dependence. Jenerkhe *et al.* [57] studied the effect of the mass transfer on the rheology of a Newtonian fluid. The authors assumed a constant evaporation rate and the changes in the viscosity were modelled by the following equation,

$$\eta = \eta_s \left[\frac{h_o}{h(t)} \right]^{\alpha}. \tag{2.156}$$

When αincreases the viscosity increases at a faster rate. However, the radial outflow is inversely proportional to the viscosity, therefore, high α leads to slower radial outflow. Note that in the previous equation $\frac{h_o}{h(t)}$ is the dimensionless thickness. Jenerkhe make the distinction between the normalised thickness of the as cast film h_{f}^* and the normalised thickness once the film has been annealed h_{a}^*. Jenerkhe predicted the following dependence of h_{a}^* on the spin speed,

$$h_{\mathrm{a}}^* \sim \omega^{-p}, \tag{2.157}$$

in this equation $p = \frac{2}{2+\alpha}$. All the previous relations relating the final thickness to the spin speed, agreed on the fact that the former is inversely proportional to a power of the latter, but never agreed on the exponent: Washo (0.681-0.69), Chen (0.5) Meyerhofer (0.4-0.5), Lai (0.5-063), Daugthon and Givens (0.51-0.82) and Wu (0.43). With his expression Jenerkhe *et al.* eliminates the apparent disagreements: for $\alpha = 2$, $p = 0.5$; for $\alpha = 1$, $p = \frac{2}{3}$ and for $\alpha = 0$, $p = 1$. Regh *et al.* [58] examined the effect of the inertial forces and the interfacial shear forces induced by an overlaying gas. They applied a finite difference method and plotted the contribution of the radial, azimuthal and axial velocity components. They showed that when the overlaying phase is a gas the interfacial shear increases the thinning rate. RBD *et al.* [3] used the Navier-Stokes equation to study the early stage of the thinning of an incompressible viscous liquid. They then study the radial profile when there is no mass transfer, evaporation or absorption at the surface. Bornside *et al.* [59] proposed a model which included the solvent concentration gradient in the film, the viscosity changes and a concentration dependent binary diffusivity. They approximated the evaporation rate to the mass transfer and obtained the following equality

$$e = k(x\mid_{z-h} - x\mid_{z=\infty}), \tag{2.158}$$

where k is the mass transfer coefficient, $x\mid_{z-h}$ is the solvent mass fraction at the surface of the film and $x\mid_{z=\infty}$ is the solvent mass fraction in the coating liquid that would be in equilibrium with the mass fraction of solvent in the bulk. Using this expression Bornside *et al.* studied thinning rate changes when a film is coated in the presence of solvent vapour. They compared their model with the EBP model by studying the case for which the thinning is only due to the convective flow i.e. $e = 0$. They compared their model to Meyerhofer's one looking at the case where the film thins due to convective

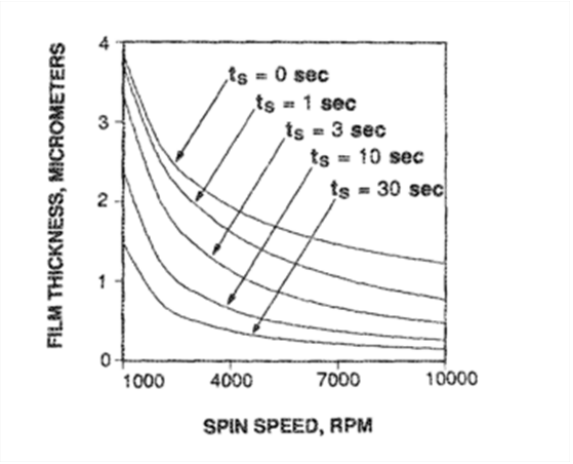

FIGURE 2.19: Film thickness as a function of the spin speed. The films are coated in the presence of solvent vapour, after t_s seconds the overlaying atmosphere is rapidly changed to solvent free as the disk continues to spin. Reprinted from D. E. Bornside, C. W. Macosko, L. E. Scriven, *J. Appl. Phys.* **66** 5185 (1989), with permission from AIP Publishing LLC

outflow and the solvent evaporates with no internal resistance (the diffusivity does not oppose the mass transfer). Their model agreed well with Meyerhofer's and the EBP model. The films were spun in an environment where the solvent concentration above them was equal to the solvent concentration in the bulk solution. After t_s seconds the air above the film was rapidly depleted of solvent vapour. Figure 2.19, shows that the film thickness decreases with t_s this is due to the fact that there is less solvent trapped in the film. They also reported that saturating the air above the film with solvent vapour leads to longer drying times.

Bornside *et al.* [7] then investigated how the gas convection above the film affects the thinning rate. They first recalled Von Kármán's theory [60]: the flow an otherwise quiescent semi-infinite fluid induced by an infinite rotating disk is incompressible, laminar and asymmetric. In these conditions the Navier-Stokes equations can be reduced to a set of ordinary differential equations in the axial axis. They then recalled how Kreith and Sparrow applied Von Kármán's theory to show that the solvent concentration and its gradient in the film are independent of the radial position. This results in a constant evaporation rate throughout the entire interface. However, the conditions referred to in Von Kármán's theory [60] are ideal. In reality the wafer has a finite size and the flow above the film is restricted with a coating bowl used to confine solvent splattering and an exhaust flow designed to reduce solvent evaporation in the room. Using numerical analysis and simulation, Bornside *et al.* predicted that the flow above the film is

laminar for an exhaust flow of 100 l/min and a spin speed of 2000 rpm. At these conditions the evaporation rate should be independent of the radius and the film should be free uniform. This was not confirmed by their experiments which show thickness non-uniformities for films cast in the above conditions. To justify the discrepancy between the simulation of the experimental observation; Bornside *et al.* raised the question of the hydrodynamic instabilities in the air flow. They used laser Doppler velocimetry and hot wire anemometry to study the flow behaviour of the air flow above a spin coater. The hot wire anemometry experiment revealed the existence of Eckman spirals near the surface of the spinning wafer. The Eckman spirals are three dimensional spiral vortices. There are three flow fields above a rotating disk which are delimitated by two critical radii. Below the first critical radius the flow is laminar, asymmetric and steady. Beyond the second critical radius the evaporation rate increases linearly with the radius. Between the two critical radii, Eckman spirals are observed and the evaporation rate is not constant. There are two types of Eckman spirals and they are differentiated by their Reynolds numbers. Bornside showed that the type II layers (Re ranging from 2000-2500) disturb the air flow above the film. The Eckman layer type I which has Reynolds number lower than 2000 promote a constant evaporation rate. Bornside filed a patent for a device that eliminated the type II Eckman layers by coating in the presence of a gas.

2.4 *In-situ* monitoring of dynamic and phase separation in spin coated films: a review

Because spin coating is a rapid process most of the studies done on its dynamics are theoretical studies which aimed to predict the final thickness as a function of the spin speed and the concentration of the solution. This is due to the lack of *in-situ* techniques to monitor the film thickness. In 1993, Horowitz *et al.* [61] used light reflectometry to follow the thickness changes during the spin coating of a sol-gel. The reflectance versus time plots are called optospinograms. The authors identified four different phases on the optospinograms. Stage one takes place prior to spinning; here the changes in reflectivity are due to the deflection of the laser. In the second stage, the convective forces lead to a rapid thickness change and the time for a full reflectance cycle is too small in comparison to the sampling period; the minima and maxima in the reflectance cannot

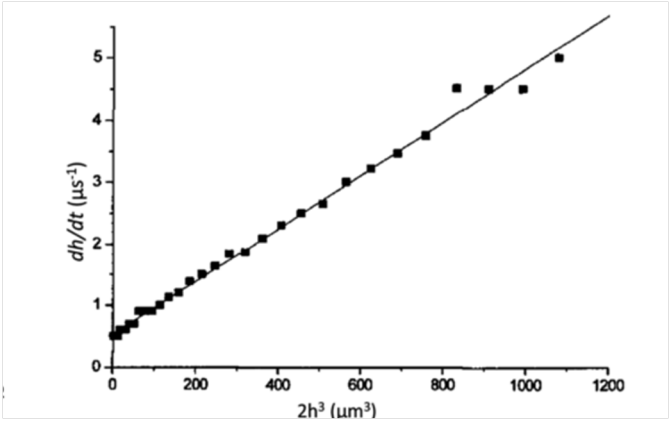

FIGURE 2.20: Thinning behaviour (Meyerhofer plot) for pure butanol thinning at 2000 rpm. The line is the linear regression fit to the data. Reprinted from D. P. Birnie *J. Non-Cryst. Solids* **218** 174, with permission of Elsevier

be distinguished. In the third phase the time for full reflectance increases and the peaks can be resolved. In the fourth stage there is no constructive or destructive interference, but the reflectance increases or decreases gradually due to low solvent evaporation. Once the film is dry, the reflectance reaches a constant value. He used the optospinogram to study the thinning rate of a solution made of silica and titania dissolved in ethanol, in the presence ethanol vapour. Regardless of the ethanol vapour above the film, stage one and two are identical. This implies that the first two stages are dominated by the radial out flow. The thinning rate during the third stage is higher for films cast in open air than for those coated in saturated vapour. In this stage the radial outflow is negligible but solvent evaporation still takes place. Horowitz showed that the radial out flow and the solvent evaporation take place simultaneously throughout the process. However the losses due to mass transfer are negligible at the beginning of the process and those due to convective forces are negligible at the end of the process.

Birnie *et al.* [12] used interferometry techniques to study the thinning of a solute free liquid. Meyerhofer 's model [2] was used to analyse the data. They plotted $\frac{dh}{dt}$ as a function of $2h^3$ (later referred as the Meyerhofer plot). They then applied a linear regression to this plot, the y intercept is equal to the evaporation rate and the slope of the line is equal to to $\frac{\rho}{3\eta}$ (see Figure 2.20). Using this method Birnie calculated the evaporation rate and the viscosity of methanol and butanol. Later Birnie *et al.* [12] studied the thinning of a mixture of these two solvents. The Meyerhofer plot revealed that unlike the case of a single solvent the thinning rate is not constant through out the process: there are two distinct phases. At the beginning of the process, the thinning rate

is determined by the viscosity and evaporation of the two solvents. Since methanol has a higher volatility, it dictates the thinning rate at the beginning of the process whereas the thinning rate at the end of the process is controlled by the viscosity and the evaporation rate of the less volatile solvent, butanol. The author defined two evaporation rates, one for the early stage of the process and another for the late stage.

In 2000 Hass *et al.* [62] used laser interferometry to investigate how the solvent evaporation affected the formation of striations in PMMA films cast from chlorobenzen (CB) and tetrahydrofuran (THF). He reported the absence of striations on the films cast from CB whereas striations were observed when coating from THF. He explained this by the lower volatility of CB which reduces the solvent gradient in the film and subsequently reduced the Marangoni effects which are thought to be at the origin of striations. The Meyerhofer plot was used to calculate the evaporation rate. In order to study the dependence of the evaporation rate on the spin speed the author expressed the evaporation rate as

$$e = C_e\sqrt{\omega}, \tag{2.159}$$

where C_e is the constant of evaporation which implicitly includes the effect of solvent vapour pressure above the film and solvent diffusion both to the film interface and in the overlaying layer. The square root dependence of the evaporation rate on the spin speed was first proposed by Meyerhofer. The evaporation constants calculated from the thinning of PMMA films were equal to those of the pure solvents. This means that in the early stage were the thinning is dominated by the radial out flow, the composition of the film does not differ much from that of a solvent layer. In agreement with Bornside *et al.* [59], high evaporation rates resulted in thicker films. Up to now the *in-situ* studies performed on the morphology of the films were based on the interpretation of the specular reflectivity.

In 2005 Jukes *et al.* [9] combined interferometry techniques with off-specular scattering. This enabled monitoring of the development of the lateral structure. The system studied was a polymer blend made of conjugated polymer poly(9,9-dioctylfluorene-co-benzothiadiazole) (F8BT) and poly(9,9-dioctylfluorene-co-bis-N,N'-(4-butylphenyl)-bis-N,N'-phenyl-1,4-phenylenediamine) (PFB). At the beginning of the process the off-specular scattering profile did not reveal any dominant length scale (see Figure 2.21). Later, the scattered light increased and at

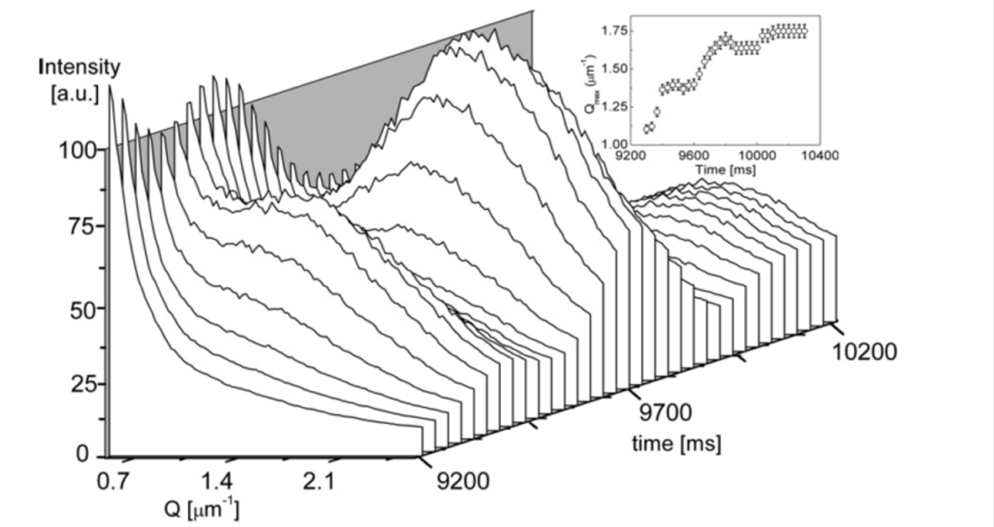

FIGURE 2.21: *In-situ* light scattering taken during the spin coating of F8BT/PFB blend from a 2% solution in oxylene spun at 2000 rpm. The data shown is for a portion of the spinning event from the cloud point to the point where the length scale stops evolving. Reprinted from P. C. Jukes, S. Y. Heriot, J. S. Sharp, and R. A. L. Jones *Macromolecules* **38** 2030 (2005) with permission from American Chemical Society

9700 ms a well-defined scattering peak was observed. The onset of the instability was found to be equal to the cloud point of the bulk solution.

During the spin coating of a transparent solution, the fluid reaches thickness values such that the interference leads to the appearance of distinct colours propagating from the centre of the substrate to its edge. These colours correlate directly to the film thickness. Birnie *et al.* [63] use this phenomenon and built a device to study the radial uniformity of the thickness during the process. Brinie *et al.* [64] combined this method with laser interferometry. The data revealed that the thickness of the film increased when moving outward from the centre

Heriot and Jones [42] studied the phase separation of a PS and PMMA film using the same technique as Jukes *et al.* [9]. They compared the visibility fringes for a film made of PMMA with those obtained for a blend of PS and PMMA. Unlike the visibility fringes for PMMA, those for PS and PMMA show modulations in the early stage follow by a decrease in the reflectivity at the cloud point. These results were interpreted as follows: in the early stage of the coating the PS and PMMA film is a bilayer. Later in the process, the film forms a single layer. In order to get a better insight of the structure of the film, the reflectivity data were modelled. Figure 2.22 shows the result of the simulation and the experimental data. Figure 2.22 (a) show the optospinogram of a PMMA film and Figure 2.22 (c) show the simulated reflectivity of a single layer. Similarly Figure 2.22(b)

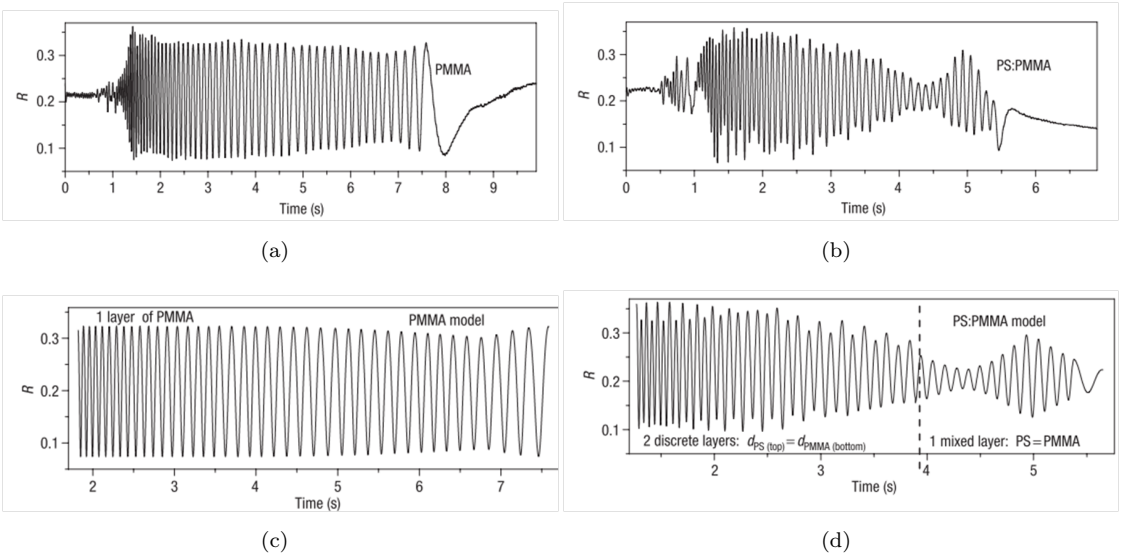

FIGURE 2.22: (a) Show the optospinogram for a homopolymer film of PMMA (b) for a blend of 50:50 PS and PMMA blend. (c) shows the simulated reflectivity for a monalayer with thins at the same thinning rate than (a). (d) Modelled reflectivity for PS and PMMA blend which thins at the same rate than (b), the film was modelled as a bilayer structure up to 3.9s, beyond this time the film is a monolayer. Adapted from S. Y. Heriot and R. A. L. Jones *Nat. Mater* **4** 782 (2005) with permission from Nature Publishing Group.

and (b) show the experimental and simulated reflectivity for a film made of PS and PMMA. The simulation assumed that the film is made of a bilayer with PS at the bottom and PMMA at the top; after 3.9 s the structure is changed to a monolayer. The resemblance between the recorded reflectivity and the modelled reflectivity for the PS and PMMA film suggests that the phase separation of PS and PMMA film transit via a bilayer structure. Heriot and Jones proposed a mechanism for the phase separation in polymer films: a bilayered structure is formed due to the of wetting layers driven by the difference in the interaction parameters and the different surface energies of the two polymers. Then the bilayer is broken due to capillary instabilities. They speculated that the instabilities were driven by the solvent gradient in the film; because the diffusion rate is slower that the rate of evaporation. The solvent concentration in the bulk is higher than the solvent concentration at the interface, therefore the surface is subject to Marangoni instabilities.

In order to verify whether the Marangoni instabilities are at the origin of the lateral phase separation, Mokarian-Tabari *et al.* [11] studied the morphology of PS and PMMA films cast from toluene in high and low vapour pressures of toluene. If the Marangoni effects are at the origin of the phase separation, coating in an environment with high vapour

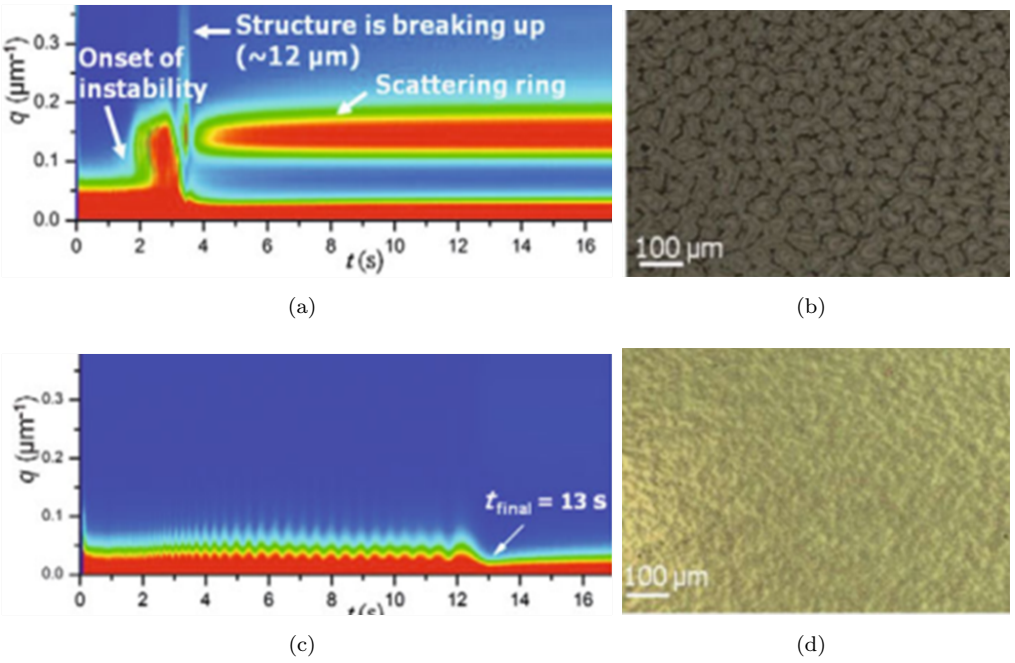

FIGURE 2.23: (a) and (d) off-specular scattering profile for a polymer blend of PS and PMMA, with solvent evaporation rates is equal to 3.15 νms^{-1} and 0.42 μms^{-1} . (c) and (d) show the corresponding microscopic images. Reprinted from P. Mokarian-Tabari1, M. Geoghegan, J.R.Howse, S.Y. Heriot, R.L. Thompson, and R.A.L. Jones *Eur. Phys. J. E. Soft Matter* **33** 283 (2010), with permission from Springer.

pressure will reduce the evaporation rate which will reduce the solvent concentration gradient and therefore reduce the Marangoni instabilities. As a consequence phase separation should be less pronounced or even eliminated. They upgraded the device previously used by Jukes *et al.* by fitting an environmental cell to control the solvent vapour during the coating. In order to check whether the cell fulfilled its purpose they first studied the evaporation of toluene at different vapour pressures. The late stages of the thinning of toluene layers were fitted with the Meyerhofer model and the evaporation rates retrieved. As expected, the evaporation rate decreased with increasing solvent vapour. They showed that the morphology of the film depends significantly on the vapour pressure. At low vapour pressure the off-specular data are characterised by two events. The onset of instabilities and the breaking up of the bilayer: a loss on the lateral structure followed by the appearance of a defined scattering peak (see Figure 2.23). At high vapour pressure there is no onset of phase separation and no scattering peak. The authors speculated that at the highest vapour pressure the film has a bilayer structure; this was confirmed using selective solvent washing and neutron scattering.

In 2011 Ebbens *et al.* [65] demonstrated a device based on stroboscopic interference

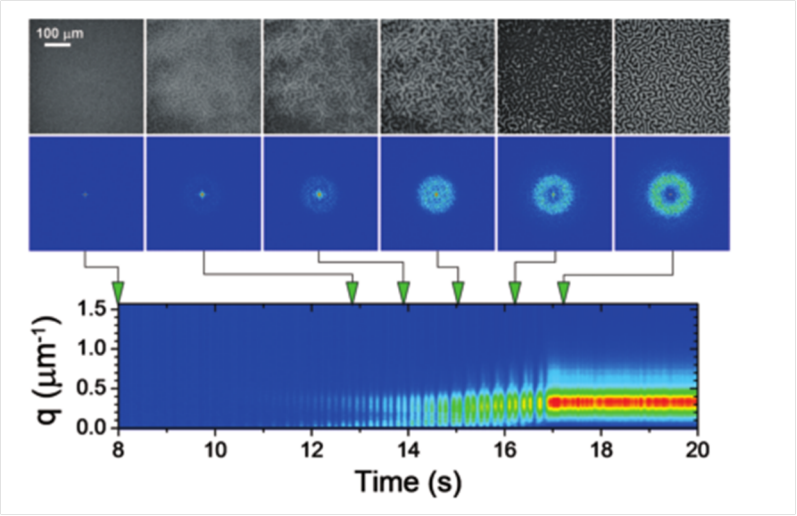

FIGURE 2.24: Stroboscopic optical reflectance images recorded during spin coating of a 1 : 1 blend of PS:PI (2 wt %) spun at 1500 rpm from o-xylene. The corresponding background- corrected 2D Fourier transforms are shown underneath each frame. The radial integral of the Fourier transform. Reprinted from S. Ebbens, R. Hodgkinson, A. J. Parnell, A. Dunbar, S. J. Martin, P. D. Topham, N. Clarke, and J. R. Howse *ACS Nano* **5** 5124 (2011), with permission from the American Chemical Society.

microscopy; this device allowed direct observations of the development of the bicontinuous morphology (see Figure 2.24). In addition, the device also monitored the specular and off-specular scattering. Using this method they studied the phase separation in PS and PI films. In the early stage of the process the images showed no contrast; as the processes evolved, fluctuation of 100 μm in the length scale were observed; these then decreased to approximately 20 μm. Phase separation took place via spinodale decomposition. The final structure shows a bi-continuous structure with dark and bright domains. Ebbens *et al.* studied the drying rate of the film. The optically dark domains dried at a slower rate and were thicker than the bright domains. Note that this is in contradiction with Bornside *et al.* [59] numerical analysis, and Mokarian-Tabari *et al.* [11] and Hass *et al.* [62] experimental observations; slow evaporation rates leads to thinner films as there is less solvent retention. Selective washing showed that the optically dark regions were made of PI.

In summary phase separation in spin coated films is a complex process which is not yet fully understood. It is dependent on several parameters such as the interaction between the components, the surface tension gradient caused by the gradient in the evaporation rate, and their interactions with the substrate. Phase separation in spin coated films is believed to take place according to the following mechanisms. Once the centrifugal force

has allowed the solution to spread the two polymers form a bilayer with the polymer with the lowest surface energy segregating to the top of the film. Instabilities at the interface of the bilayer lead to its deformation and eventually the bilayer breaks leaving a phase separated structure. Phase separation is less pronounced when coating with a solvent with a high boiling point rather than a low boiling point. The bilayer structure can be stabilised when coating in the presence of solvent vapour. The recently developed techniques in *in-situ* light scattering and stroboscopic microscopy enables monitoring of the evolution of phase separation during spin coating which shows two remarkable features. Initially the scattered light is low then followed by a significant increase in the light scattered. The second feature is a decrease in the light scattered followed by the appearance of a scattering ring. There is not full understanding of what is happening in the film at this time and understanding of these features requires an understanding of the thermodynamics. This requires *in-situ* knowledge of the film composition, which in turn requires modelling of the thinning rate of the film. The dynamics of spin coating has been the subject of numerous theoretical studies and several models have been proposed. The models proposed by [1], Meyerhofer [2] and RDB [3] account for centrifugal and the viscous forces. They differ to one another by accounting for one or several of the following parameters: the evaporation rate, the change in the viscosity, and the inertial forces. The models agree on the fact that the initial thinning is dictated by hydrodynamic forces. As the viscosity increases the fluidity of the film decreases and the thinning rate of the film is dictated by the evaporation rate. Although the dynamics affects the phase separation, most studies treat these problems separately. Here we study phase separation alongside the dynamics using an apparatus that uses light interferometry and light scattering to monitor the thickness and the scattered light as a function of time. After reviewing the experimental methods used in the next chapter we consider the dynamics of spin coating in chapter 4. In chapter 5 and 6 we will investigate the effect of the concentration and the interaction parameter on the phase separation.

Chapter 3

Experimental techniques

3.1 Optospinometer

The optospinometer is a light scattering instrument which combines specular and off-specular scattering to monitor the thinning rate and the development of a lateral structure during the spin coating of a polymer film (see Figure 3.1). A monochromatic He-Ne laser with a wavelength of 633 nm was mounted at 45° to a spin coater. The incident beam is focused at the centre of the rotating stage of the spin coater which can reach spin speeds up to 10 000 rpm. The incoming beam and the reflected beam are collected by two silicon photodiodes with a time resolution of 1 ms. The scattered light is recorded by a charge coupled device (CCD) camera with a time resolution of 30 ms. The off-specular scattering data are used to follow the development of a phase separation. The specular reflectivity data are used to obtain the thickness as a function of time. In the next three subsections we will see how the specular data are used to produce the thickness time profile. Then we will see how the the off specular data is analysed to obtain the off specular scattering profile. To finish we show how the optospinometer was modified to control the vapour pressure and the temperature during coating.

3.1.1 Thickness profile

As we previously mentioned specular reflection is used to monitor the thickness change during the coating. When an incoming beam is reflected from a surface and the angle of incidence is equal to the reflected angle we speak of specular reflections. Figure 3.2a)

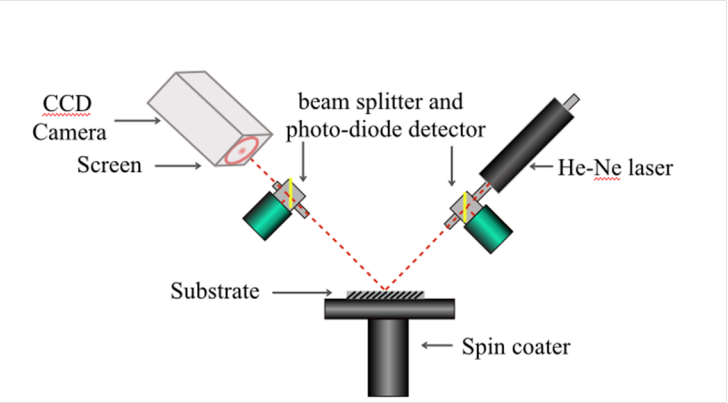

FIGURE 3.1: Optosinometer

shows a diagram of specular reflection. Figure 3.2b) is a diagram of diffuse scattering from a rough surface. We speak of diffuse scattering when the angle formed by the normal to the surface and the reflected light is not equal to the incident angle.

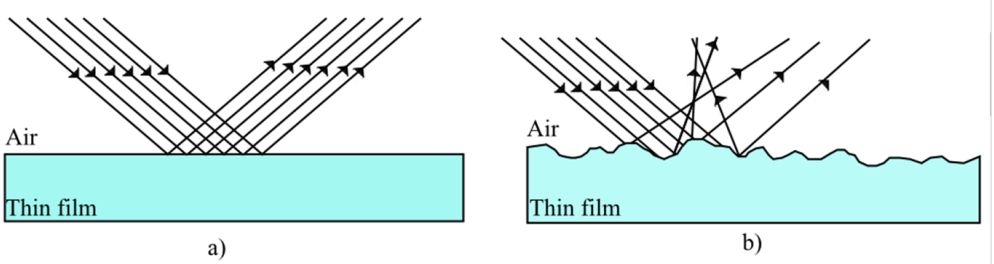

FIGURE 3.2: Diagram showing a) specular reflection and b) diffuse scattering

When a beam is passed through two media with different refractive indices two phenomena take place simultaneously: light reflection at the substrate/film interface and light refraction at the air/film interface (see Figure 3.3). A typical graph of the reflectivity versus time is shown on Figure 3.4. The curve exhibits a succession of peaks and troughs which illustrate constructive and destructive interferences. Constructive interference occurs when the Bragg's law is fulfilled, i.e. when the extra path travelled by the beam reflected at the film/substrate interface is a multiple of the wavelength of light λ.

In Figure 3.3, the extra path is equal to $AN + BN$. Therefore the Bragg's law can be expressed mathematically by

$$AN + BN = 2AN = \lambda m. \tag{3.1}$$

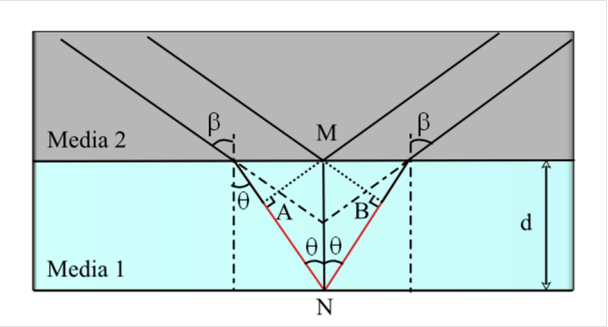

FIGURE 3.3: Reflection and refraction of the a beam passing though two media. β is the incident angle, θ is refracted angle, d is the thickness of the film at a given time

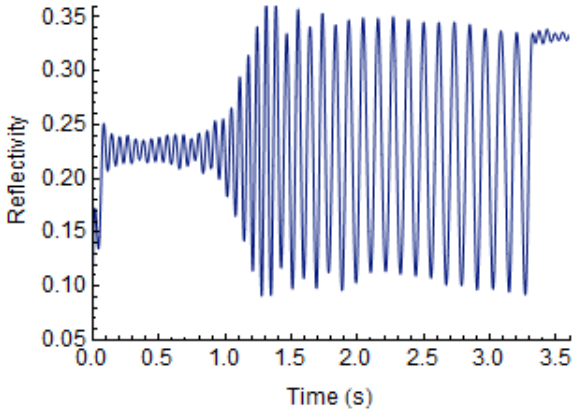

FIGURE 3.4: Typical reflectivity profile during the evaporation of a toluene layer.

Working in the right angle triangle AMN, AN can be expressed as

$$AN = 2d\cos(\theta) \tag{3.2}$$

Therefore Bragg's law is expressed by the following equality

$$\lambda m = 2d\cos\theta, \tag{3.3}$$

where θ is the internal angle and can be determined by applying Snell's law

$$n_1\sin(\beta) = n_2\sin(\theta). \tag{3.4}$$

Therefore θ can be expressed as $\theta = \arcsin(\frac{n_1\sin(\beta)}{n_2})$

Using equation 3.3 we can calculate the amount by which the thickness decreases between two successive peaks,

$$\triangle h = \frac{\lambda}{2n\cos\theta} \tag{3.5}$$

Once we know the final thickness we can count back the maxima on the reflectivity versus time curve and we obtain the thickness profile:

$$h(t) = h_f + (m-1)\triangle h. \tag{3.6}$$

In this equation m is an integer which takes a value between zero and the number of distinguishable peaks on the reflectivity profile curve. During the coating of a polymer solution, as the solvent evaporates, the refractive index changes due to the change of the volume fraction of the polymer A, polymer B and solvent S. In order to mimic this change we assume a linear dependence of the refractive index with time from the polymer solution to the solid thin film

$$n(t) = n_i + tg_n, \tag{3.7}$$

where g_n is the gradient and n_i is the initial refractive index of the ternary polymer solution made of polymer A, polymer B and solvent S. It can be expressed as

$$n_i = n_A\phi_{Ai} + n_B\phi_{Bi} + n_S\phi_{si}, \tag{3.8}$$

where n_A, n_B and n_s are the reflective indexes of polymer A, polymer B and the solvent. Note that when studying the evaporation of a solvent $g_n = 0$ and $n_i = n_s$. We assume that there is no solvent retention in the final film and the refractive index of the film is given by

$$n_f = n_{Af}\phi_A + n_B\phi_{Bf}. \tag{3.9}$$

Using the Equation 3.8 and Equation 3.9 we can express the gradient

$$g_n = \frac{n_f - n_i}{t_f}, \tag{3.10}$$

here t_f is the time necessary for the film to dry. Substituting equation 3.10 in equation 3.7 , equation 3.6 can be rewritten as

$$h(t) = h_f + \frac{(m-1)\lambda}{2(n_i + t\frac{n_f - n_i}{t_f})\cos\theta}. \tag{3.11}$$

3.2 Off specular scattering

When a beam is reflected on a rough surface, light is scattered at an angle which differs from the incident angle. The scattered light is used to monitor the development of lateral structure in the film. In analogy with phase separation in bulk solutions, the cloud point is defined as the time when the instabilities in the film start. Depending on the interaction between the polymer chains and the drying rate; phase separation can take place giving rise to a regular structure which leads to a maximum in the scattering intensity translated by a scattering ring. When using the optospinometer to coat a polymer film for 10 s, the device will record 300 grayscale images that must be analysed in order to monitor how the structure and the length scale evolves with time. Figure 3.5 show a diagram of the procedure used. We use a program written in LabVIEW 8.5. Each image is an intensity map in which a pixel is identified by a radial position y and an angle Θ. The user chooses the centre of the image then the program unwraps the image. The image is then radially averaged. This process is repeated for all the images acquired during the scan, and the radially averaged intensities are plotted as a function of time. These plots are calibrated using a 100 nm grid.

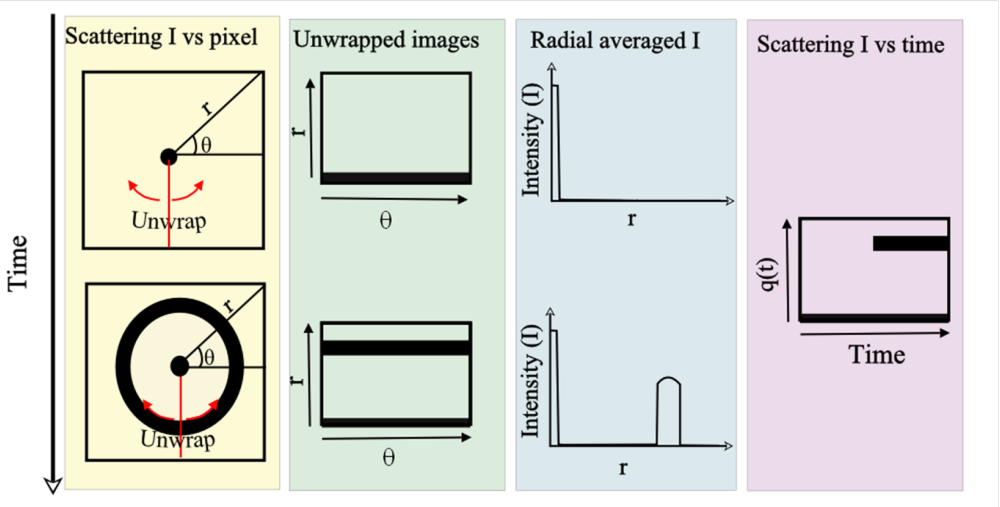

FIGURE 3.5: Diagram showing the procedure used to analyse the off specular data. The images acquired during the scan are unwrapped and the radial intensity is averaged. Repeating this process for all the pictures enables to plot the average intensity versus time.

3.2.1 Vapour pressure control

A custom made cell is used to control the solvent vapour pressure above the film (see Figure 3.6). The cell was fitted with two glass windows which allowed the reference beam to travel into the cell and the reflected beam out of the cell. The alignment of the reference beam, the centre of the substrate and the reflected beam is possible by adjusting the height of the spin coater. The cell has three outlets: the first one to deposit the polymer solution, the second one to allow in the toluene vapour and the third one to exhaust it. 3 $\mathrm{l\,min^{-1}}$ nitrogen flows in a bubbler filled with toluene. The bubbler is immersed in a water bath and precise control of the solvent vapour in the cell is possible by controlling the temperature of the bath. The solvent vapour in the cell is related to the bath temperature by the Clausius Clapeyron equation,

$$\frac{P(T)}{P(T_\mathrm{o})} = \exp\left(-\frac{\Delta H_\mathrm{v}}{R}\left(\frac{1}{T_\mathrm{b}} - \frac{1}{T}\right)\right), \tag{3.12}$$

where ΔH_v is the enthalpy of evaporation of the solvent, R is the gas constant, T_b is the boiling point of the solvent and $P(T_\mathrm{b})$ and $P(T)$ are the solvent vapour pressures at its boiling point and another (lower) absolute temperature, T, respectively. The procedure used was slightly different when spin coating a polymer solution and a solute free liquid. In the first case, the silicon is enclosed in the chamber and toluene vapour was allowed to flow in for a minute. The polymer solution was deposited through the outlet then spun. In the second case a substrate covered with toluene was enclosed in the cell for a minute prior to spin coating. Because the exposure to toluene alters the wetability of the silicon, the number of measurements performed with one substrate was limited to three.

3.2.2 Temperature control

A copper coil was glued to the wall of the environmental cell. Two pipes connect the coil to a circulator filled with 50 % water and 50% ethylene glycol. The pump of the circulator allowed a constant motion of the mixture in the coil (see Figure 3.7). The temperature in the cell, which is referred to as the coating temperature, was controlled by setting the temperature of the circulator and was monitored with a digital thermometer. The temperature of the solutions were controlled by immersing them in a beaker which

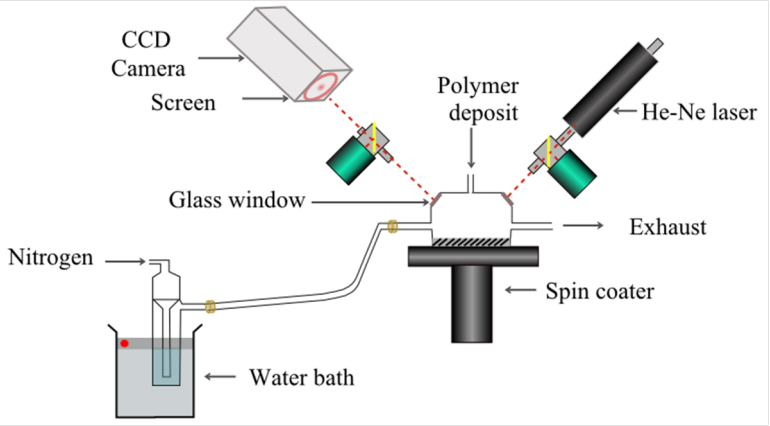

FIGURE 3.6: Experimental set up used to control solvent vapour pressure during the coating

in turn was immersed in a water bath. The temperature of the water bath was set to be equal to the coating temperature. Prior to coating, the silicon wafer was also allowed to reach the coating temperature by enclosing it in the cell. As the coating temperature was lowered to 7°C and 0°C; water and ice condensed on the window of the cell and reduced the intensity of the incoming beam. In order to overcome this problem the cell was blow dried with air prior to every measurement. The temperature of the circulator was always lower than the temperature in the cell; for example the temperature of the circulator was set to -12°C in order to reach a coating temperature of 0°C.

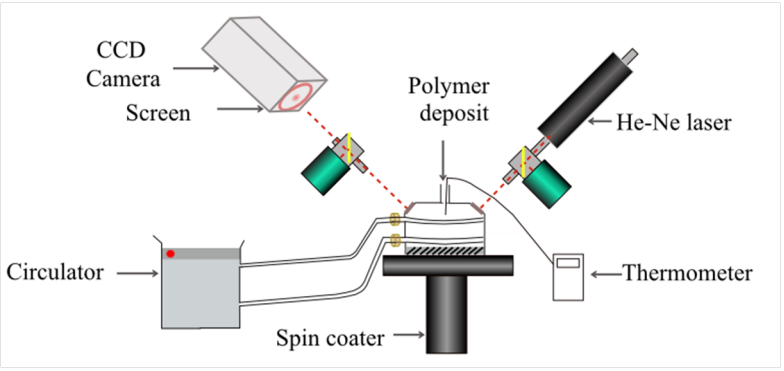

FIGURE 3.7: Experiemental set up used to control the temperature during the coating

3.3 Spectroscopic ellipsometry

Spectroscopic ellipsometry uses the interaction between light and a thin film to determine the optical properties and the thickness of a film. In order to understand ellipsometry it is necessary to describe light as an electrical wave in space and time. Light can be

separated as two independent orthogonal electrical fields: one that is parallel to the plane of incidence and one that is perpendicular to the plane of incidence. In Figure 3.8 which shows a diagram of spectroscopic ellipsometry, the incoming light and outgoing light are note as E_i and E_o. Their parallel components are noted as E_{ip} and E_{op}. Similarly their perpendicular components are noted as E_{is} and E_{os}. The two couples E_{is} and E_{os} and E_{ip} and E_{op} are related by the Fresnel reflection coefficients,

$$r_s = \frac{E_{os}}{E_{is}} = \frac{\tilde{n}_1 cos\beta - \tilde{n}_2 cos\theta}{\tilde{n}_1 cos\beta + \tilde{n}_2 cos\theta} \tag{3.13}$$

and

$$r_p = \frac{E_{op}}{E_{ip}} = \frac{\tilde{n}_1 cos\beta - \tilde{n}_2 cos\theta}{\tilde{n}_1 cos\theta + \tilde{n}_2 cos\beta}. \tag{3.14}$$

In these equations β and θ are the incident angle and the refracted angle, respectively. r_s and r_p are the reflection coefficient for light polarised in the perpendicular and the parallel plan to the incident plane. $\tilde{n}_1$ and $\tilde{n}_2$ are the complex refractive index of air (medium 1) and the complex refractive index of the polymer film (medium 2). There are expressed as

$$\tilde{n}_1 = n_1 - iK_1 \tag{3.15}$$

and

$$\tilde{n}_2 = n_2 - iK_2 \tag{3.16}$$

where n_1 and n_2 are the refractive index of the air and the refractive index of the polymer film and K_1 and K_2 are the imaginary part of the refractive index of the air and the film, they are called the extension coefficients. In spectroscopic ellisposmetry, polychromatic unpolarised light passes through a polariser which polarises the light linearly with a known polarisation. The light is then reflected and refracted by the film. The optical properties of the film and its thickness changes the polarisation of the light. The change in polarisation is measured by an analyser and is expressed as

$$\rho_p = \frac{r_p}{r_s} = \tan(\phi) e^{i\triangle}. \tag{3.17}$$

The analyser calculates ϕ and $\triangle$ in the range of wavelengths where the measurement was performed. Once the data are acquired a model is created to describe the sample investigated. The model describes the number of layers in the sample: film and substrate, the thickness of every layer and their refractive index to calculate ϕ and $\triangle$. The predicted

ϕ and $\triangle$ are then compared with the experimental ones. In order to express the refractive index of the film at all the wavelengths probed we use a dispersion equation. Here we used the Cauchy model, is expressed as

$$n = A + \frac{B}{\lambda^2} + \frac{C}{\lambda^4}, \tag{3.18}$$

where A, B and C are constants.

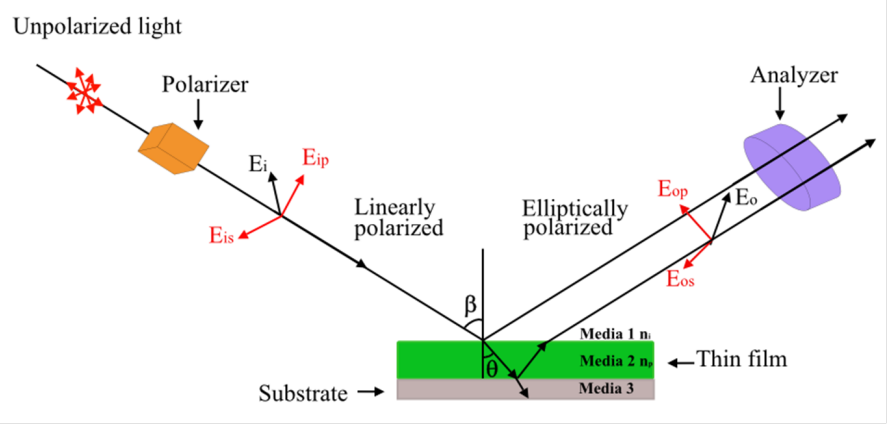

FIGURE 3.8: Diagram of spectroscopic ellispometry

3.4 UV-visible spectrometer

Two kinds of phenomena occur when light passes through a solution: absorption and scattering. Scattering includes reflection, refraction and diffraction of light. Because phase separated polymer solutions are turbid due to the existence of heterogeneity of polymers suspended in a solvent, light transmission is often used to monitor phase separation in bulk systems. The polymer solutions are brought into the single phase by heating. The temperature is decreased while the absorption is recorded. At the cloud point the solution becomes turbid and the light absorbed increases. By measuring light absorbed from polymer solutions with different solvent contents we can identify the cloud point (onset of phase separation). A Cary 300 UV-vis spectrophotometer was used to measure light absorption at a wavelength of 500 nm. The cell holder was equipped with a magnetic stirrer and a temperature control. The solutions were place in a 1 ml quartz cuvette with a path length of 10 mm. The solutions were first heated until they were clear; all the solutions studied were clear at 25 °C. The temperature was decreased at a rate of 0.1 °C per minute and data was acquired every 0.5 °C. During the data

acquisition the solutions were continuously stirred. The Beer-Lambert law relates the absorption A, with the solution concentration c, the length of solution that the light goes through and the molar absorptivity ϵ by the equation

$$A = lc\varepsilon = \log\left(\frac{E_o}{E_i}\right), \tag{3.19}$$

here E_o and E_i are the outcoming and incoming intensities. Note that absorption is a dimensionless quantity. The cloud point was defined as the temperature at which an inflection point is observed in the absorbance.

3.5 Substrate

The films were cast on silicon wafers with a surface area of 1cm^2. The silicon was cleaned using the RCA1 procedure. A mixture of water, hydrogen peroxide and ammonium hydroxide in the proportion of 5:1:1 was heated at 70°C. The silicon pieces were immersed in the mixture for ten minutes then rinsed with deionised water and blow dried with nitrogen

3.6 Polymer

The two polymers were purchased from Polymer Laboratories; their chemical structures are shown in Figure 3.9.

The weight average molecular weight (Mw), the number average molecular weight (Mn) and the polydisersity index (PDI) of the two polymers are reported in Table 3.1. We calculated the end to end distance of these two polymers in the presence of toluene. The Kuhn length is taken to be equal to 1.67 nm for PS and 1.36 nm for PMMA.

Name	Mw (Da)	Mn (Da)	PDI	$\sqrt{< R^2 >}$ (nm)
PMMA	99400	92100	1.08	14.49
PS	96000	92000	1.04	15.43

TABLE 3.1: Table reporting the weight average molecular weight (Mw), the number average molecular weight (Mn), the polydispersity (PDI) and the root-mean-square end-to-end distance.

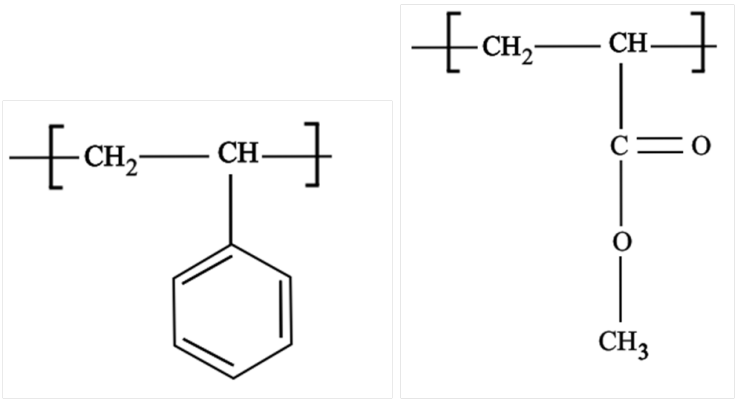

(a) (b)

FIGURE 3.9: (a) shows the chemical structure of PS. (b) shows the chemical structure of PMMA.

The overlap volume fraction is equal to 0.0513. The solutions studied here are at a higher polymer volume fraction than the overlap volume fraction, therefore they are in the semi-dilute regime.

3.7 Solvent

The toluene was obtained from the Department of Chemistry at the University of Sheffield. Toluene has a vapour pressure of 22 mm Hg at room temperature, a boiling point of 110.6°C and a melting temperature of -93°C .The chemical structure of toluene is shown on Figure 3.10.

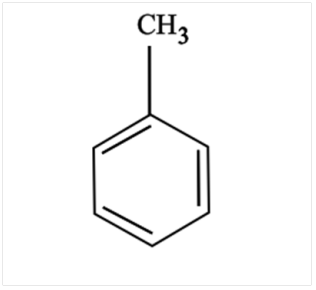

FIGURE 3.10: Shows the chemical formula of toluene

3.8 Deposition technique

The solution was deposited on the substrate via static deposition. The entire substrate is covered with the solution prior to spin coating.

Chapter 4

Dynamics of spin coating

In this chapter we will study the dynamics of spin coating. In section 4.1 we introduce the semi-empirical model. The RBD equation introduced in section 2.3 is a dimensionless equation; in order to fit the experimental data with this model it is necessary to re-dimensionalise this equation. In section 4.2 we will calculate the dimensionalised form of the RBD differential equation. The numerical methods used in this project will be reviewed in section 4.3. The RBD model and the semi-empirical model are solved using the fourth order Runge-Kutta method. In order to get an understanding of this method we will first review and derive the first and the second order Runge-Kutta methods. We will also review the change of variable methods used to solve the Meyerhofer model. Spin coating is a very fast process; in order to study experimentally the first stage of this process which lasts less than 2 s, it is necessary to verify that the ramping up speed of the optospinometer and its time resolution are fast enough to acquire accurate data; this will be done in section 4.4. Section 4.5 deals with the thinning of a toluene layer in different vapour pressures of toluene. We will compare and discuss the fits obtained with the RBD, the Meyerhofer and the semi empirical model. In section 4.6 we will study the thinning of homopolymer films of PS, PMMA and blends of these two polymers at different vapour pressures. We will also investigate how the vapour pressure affects the final film thickness, the time necessary for the film to dry and the evaporation rate. The work presented in this chapter is summarised in Y. Mouhamad, P. Mokarian-Tabari, N. Clarke, R. A. L Jones and M.Geoghegan *J. Appl. Phys.* **116**, 123513 (2014)

4.1 Semi-empirical model

As we have seen in section 2.3 the RBD model aims to propose an equation of motion which would give a better description of the early stage of spin coating, where the inertial forces are important. Calculations in section 2.3 showed that the extra term is a correction on the vertical velocity. Therefore the extra velocity term accounts for the effect of the inertial forces on the axial velocity. The differential equation that we propose to describe the of dynamics of spin coating is given by

$$\frac{\partial h}{\partial t} + e + \frac{2\omega^2 \rho h^3}{3\eta} + \frac{W_0}{\exp(U^{t/\tau})} = 0, \tag{4.1}$$

where W_0, U, and τ are fitting parameters. This equation is identical to the Meyerhofer equation aside from the fourth term which is a correction on the velocity term. Similar to the RBD model the correction term aims to give a better description of the early stage of spin coating. By comparing the semi-empirical model to the RBD model we deduce that the fitting parameter $W_0/exp[1]$ are the initial losses in the rate of thinning due to inertial forces and $U^{t/\tau}$ represent the rate at which the losses decrease.

4.2 Re-dimensionalisation of the RBD equation

The RBD equation is a dimensionless equation, but the experimental thickness profiles have a dimension of length versus time. To compare the data with the RBD model one can reduce the data or re-dimensionalise the RBD equation. Both of these methods are correct. However, we need to ensure that the chosen method will enable comparison with the semi-empirical model. As the scaled variables are unknown, the semi-empirical model equation cannot be reduced. For these reasons we decided to re-dimentionalise the RBD equation. The reduced RBD equation is given by

$$\frac{\partial h^*}{\partial t^*} + \frac{2}{3}\left(E + h^{*3} + \epsilon \mathrm{Re}\left[\frac{5E}{12}h^{*4} - \frac{34}{105}h^{*7}\right]\right) = 0, \tag{4.2}$$

where h^* and t^* are the dimensionless thickness and time. E is the dimensionless evaporation rate and ϵ is the aspect ratio. The scaled variables used to derive the

RBD model are defined as:

$$\epsilon = \frac{h_o}{L}, \quad h^* = \frac{h}{h_o}, \quad t^* = \frac{t}{T_o}, \quad \text{and} \quad \text{Re} = \frac{U_o h_o \rho}{\eta}, \tag{4.3}$$

where T_0 is the time unit defined as,

$$T_o = \frac{L}{U_o}, \tag{4.4}$$

and U_o is the radial velocity unit defined by,

$$U_o = \frac{\omega L h_o^2 \rho}{\eta}. \tag{4.5}$$

The re-dimensionalised RBD equation is given by

$$\frac{T_o \partial h}{h_o \partial t} + \frac{2}{3}\left(E + \frac{h^3}{h_o^3} + \epsilon\text{Re}\left[\frac{5E}{12}\frac{h^4}{h_o^4} - \frac{34}{105}\frac{h^7}{h_o^7}\right]\right) = 0. \tag{4.6}$$

We calculate E, T_o/h_o, and ϵRe

$$E = \frac{3e}{2\epsilon U_o} = \frac{3e}{2\epsilon(\frac{\omega L h_o^2 \rho}{\eta})} = \frac{3e\eta}{2h_o^3 \rho \omega^2}, \tag{4.7}$$

$$\frac{T_o}{h_o} = \frac{L\eta}{\rho\omega^2 L h_o^3} = \frac{\eta}{\rho\omega^2 h_o^3}, \tag{4.8}$$

and

$$\epsilon\text{Re} = \frac{h_o^4 \omega^2 \rho^2 L}{\eta^2 L} = \frac{h_o^4 \omega^2 \rho^2}{\eta^2}. \tag{4.9}$$

Equation 4.6 can be rewritten as

$$\frac{\eta}{\rho\omega^2 h_o^3}\frac{\partial h}{\partial t} + \frac{2}{3}\left(\frac{3e\eta}{2h_o^3\rho\omega^2} + \frac{h^3}{h_o^3} + \frac{h_o^4\omega^2\rho^2}{\eta^2}\left[\frac{15e\eta}{24h_o^3\rho\omega^2}\frac{h^4}{h_o^4} - \frac{34}{105}\frac{h^7}{h_o^7}\right]\right) = 0. \tag{4.10}$$

Multiplying Equation 4.10 through with $\frac{\rho\omega^2 h_o^3}{\eta}$ yields

$$\frac{\partial h}{\partial t} + e + \frac{2}{3}\left(\frac{\rho\omega^2}{\eta}h^3 + \frac{\omega^4\rho^3}{\eta^3}\left[\frac{15e\eta}{24\rho\omega^2}h^4 - \frac{34}{105}h^7\right]\right) = 0 \tag{4.11}$$

Equation 4.11 is the re-dimensionalised equation that we will solve.

4.3 Numerical modelling

4.3.1 Runge-Kutta methods

In the fields of physics, chemistry, biology and fluid dynamics differential equations are often used to describe the temporal evolution of phenomena. In many cases these equations cannot be solved analytically. Numerical modelling is used to approximate the solution. The Runge-Kutta methods are a family of iterative methods to solve first order differential equations. They are named after two German mathematicians: Carl David Tolme Runge and Martin Wilheim Kutta. Given a differential equation which can be written in the form

$$\frac{dy}{dt} = f(t, y) \tag{4.12}$$

in which f is a function dependable on y and t, y depends on t, which does not depend on any variable and the solution to the equation satisfy the initial conditions:

$$y(t_0) = y_o, \tag{4.13}$$

a time step size b is defined and the value of y at $t = t_o + b$ is approximated to

$$y_o + \triangle y. \tag{4.14}$$

In this expression $\triangle y$ is an increment and has a different expression for every Runge-Kutta method. These methods are only applicable for differential equations with an initial condition which are called initial value problems. The first-order Runge-Kutta method is also known as the Euler integration method. The more commonly used Runge-Kutta methods are the second and the fourth order methods which are often noted as RK2 and RK4. Here the experimental data was fitted using RK4. In order to acquire a better understanding of RK4 we will first review and derive the Euler integration method and RK2.

4.3.1.1 Euler's integration method

Euler's integration method states that solutions to the differential equation

$$\frac{dy}{dt} = f(t, y), \qquad y(t_0) = y_o \tag{4.15}$$

can be approximated by

$$y_{n+1} = y_n + bf(t_n, y_n). \tag{4.16}$$

In this equation y_{n+1} is the solution after $n+1$ step and is an approximation of $y(t_{n+1})$.

In order to estimate the solution to the differential Equation 4.15, we express the Taylor series expansion,

$$y(t_n + b) = y(t_n) + b\frac{dy}{dt} + O(b^2). \tag{4.17}$$

Substituting Equation 4.15 into Equation 4.17 yields

$$y_{n+1} = y_n + bf(t_n, y_n). \tag{4.18}$$

The approximated solution calculated using Equation 4.18 gets closer to the exact solution when b decreases.

4.3.1.2 Second-order Runge Kutta method

Definition RK2 states that the solution to the differential equation to Equation 4.15 can be approximated by

$$y_{n+1} = y_n + \frac{1}{2}k_1 + \frac{1}{2}k_2, \tag{4.19}$$

with

$$\begin{aligned} k_1 &= bf(t_n, y_n) \quad \text{and} \\ k_2 &= bf(t_n + b, y_n + k_1 b). \end{aligned}$$

Derivation In a similar way to the Euler integration method, RK2 takes successive steps to approximate the Taylor series of the solution. Runge and Kutta propose that

Equation 4.15 have a solution in the form of

$$y_{n+1} = y_n + \alpha k_1 + \beta k_2, \tag{4.20}$$

with

$$\begin{aligned} k_1 &= bf(t_n, y_n) \\ k_2 &= bf(t_n + \gamma b, y_n + \delta k_1 b). \end{aligned}$$

The derivation consists of finding the values of α, β, γ and δ for which Equation 4.20 will be equal to the Taylor series of $y(t_n + b)$, the expansion of which is given by

$$y(t_n + b) \simeq y_{n+1} = y_n + \frac{dy}{dt}b + \frac{1}{2!}\frac{d^2y}{dt^2}b^2 + O(b^3). \tag{4.21}$$

Substituting Equation 4.15 into Equation 4.21 yields

$$y_{n+1} = y_n + f(t, y)b + \frac{1}{2!}f'(t, y)b^2 + O(b^3). \tag{4.22}$$

Applying the chain rule to $f'(t, y)$ we obtain

$$f'(t, y) = \frac{df(t, y)}{dt} + \frac{df(t, y)}{dy}\frac{dy}{dt}, \tag{4.23}$$

which is equivalent to

$$f'(t, y) = \frac{df(t, y)}{dt} + \frac{df(t, y)}{dy}f(t, y). \tag{4.24}$$

Substituting Equation 4.24 into Equation 4.22 yields

$$y_{n+1} = y_n + f(t, y)b + \frac{1}{2!}b^2(\frac{df(t, y)}{dt} + \frac{df(t, y)}{dy}f(t, y)) + O(b^3). \tag{4.25}$$

y_{n+1} can also be calculated by using Equation 4.20. We first need to calculate the Taylor series of k_2 which is given by,

$$k_2 = bf(t, y) + \gamma b^2\frac{df(t, y)}{dt} + f(t, y)b^2\frac{df(t, y)}{dy}. \tag{4.26}$$

Substituting Equation 4.26 in Equation 4.20 yields

$$y_{n+1} = y_n + b(\alpha + \beta)f(t, y) + \beta\gamma b^2\frac{df(t, y)}{dt} + \beta f(t, y)b^2\frac{df(t, y)}{dy} \tag{4.27}$$

In order for Equation 4.27 to be equal to Equation 4.25, we set

$$\begin{aligned} \alpha + \beta &= 1, \\ \beta\gamma &= \tfrac{1}{2}, \text{and} \\ \beta\delta &= \tfrac{1}{2}. \end{aligned}$$

This is a system of three equations with four unknowns. Runge and Kutta set $\alpha = \frac{1}{2}$, and so

$$\begin{aligned} \beta &= \tfrac{1}{2}, \\ \gamma &= 1, \text{and} \\ \delta &= 1. \end{aligned}$$

4.3.1.3 The fourth-order Runge-Kutta method

Definition The fourth-order Runge-Kutta method states that the solution to Equation 4.15 is can be expressed by

$$y_{n+1} = y_n + \frac{1}{6}(k_1 + 2k_2 + k_3 + k_4), \tag{4.28}$$

with

$$\begin{aligned} k_1 &= bf(t_n, y_n), \\ k_2 &= bf(t_n + \tfrac{1}{2}, y_n + \tfrac{b}{2}k_1), \\ k_3 &= bf(t_n + \tfrac{1}{2}b, y_n + \tfrac{b}{2}k_2), \quad \text{and} \\ k_4 &= bf(t_n + b, y_n + bk_3). \end{aligned}$$

The derivation of the RK4 is a long and complicated calculation which is beyond the scope of this work. The mechanism for the Runge-Kutta nevertheless jets out in the Euler integration and RK2. RK4 develops this theme further. On Figure 4.1 we plot the solutions to the differential equation $y' = 2y, y(0) = 1$ using the Euler's integration method, RK2 and RK4. We also plot the exact solution. Note that the solution obtained with RK4 is identical to the exact solution; the higher the order of the Runge Kutta method the better is the approximation. For this reason we fitted the data with RK4

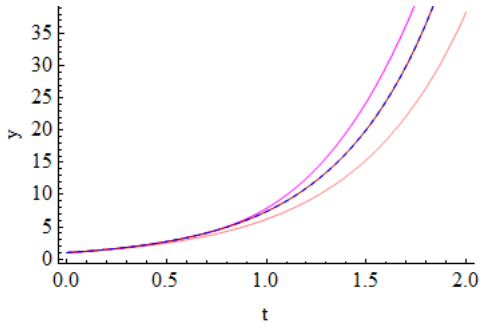

FIGURE 4.1: Plot of the solution to the differential equation $y' = 2y, y(0) = 1$. The pink curve is the solution obtained using the Euler method. The magenta curve is the solution obtained using RK2, the red curve is the solution obtained with the RK4 and the dashed blue curve is the exact solution.

We apply the RK4 method to the semi-empirical model. We write Equation 4.1 in the form $h'(t) = f(h,t)$ and the initial condition

$$f(h,t) = -e - \frac{2\omega^2 h^3}{3\nu} - \frac{W_0}{\exp(U^{t/\tau})}, \quad h(t_o) = h_o. \tag{4.29}$$

where h_o and t_o are the initial thickness and the initial time. The initial time is defined as the first distinguishable peak in the experimental data and the corresponding thickness is the initial thickness. The algorithm chooses the best step size b and the approximation of the solution is equal to

$$h_{n+1} = h_n + \frac{1}{6}b(k_1 + 2k_2 + k_3 + k_4) \tag{4.30}$$

with

$$\begin{aligned}
k_1 &= -be - \frac{2b\omega^2 h_n^3}{3\nu} - \frac{bW_0}{\exp U^{\frac{t_n}{\tau}}}, \\
k_2 &= -be - \frac{2b\omega^2\left(h_n + \frac{b}{2}k_1\right)^3}{3\nu} - \frac{bW_0}{\exp U^{\frac{t_n+\frac{1}{2}b}{\tau}}}, \\
k_3 &= -be - \frac{2b\omega^2\left(h_n + \frac{b}{2}k_2\right)^3}{3\nu} - \frac{bW_0}{\exp U^{\frac{t_n+\frac{1}{2}b}{\tau}}}, \quad \text{and} \\
k_4 &= -be - \frac{2b\omega^2\left(h_n + bk_1\right)^3}{3\nu} - \frac{bW_0}{\exp U^{\frac{t_n+b}{\tau}}}.
\end{aligned}$$

The Runge-Kutta methods can be separated into two categories, implicit and explicit methods. Implicit methods are used when solving stiff differential equations. Stiffness is a complex concept of numerical analysis which is beyond the scope of this thesis.

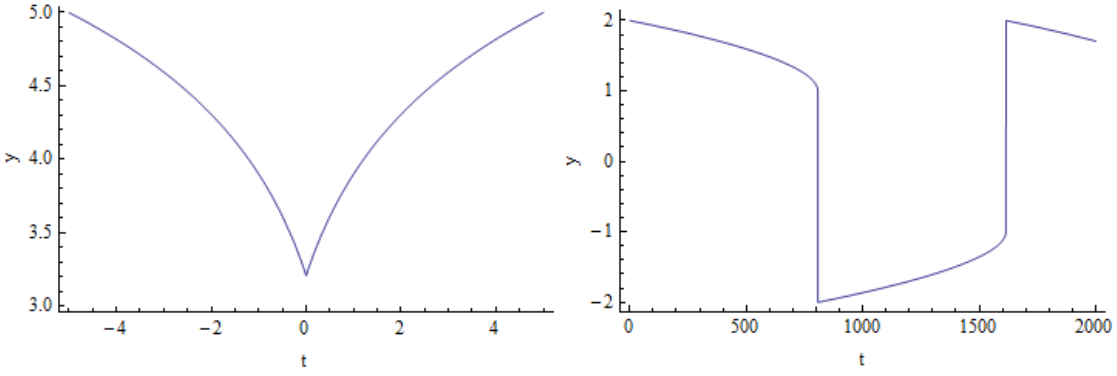

(a) (b)

FIGURE 4.2: Plot of two stiff functions.

However, prior to using an explicit Runge-Kutta method it is advisable to verify whether or not the differential equation is stiff. A differential equation is said to be stiff when its solution has one or many points where the slope changes very rapidly. Figure 4.2 shows two plots of stiff functions. Data fitting is performed using the explicit RK4 routine provided in *Mathematica 7*. Prior to solving the differential equation the algorithm tests for non-stiffness. Both the RBD model and the semi-empirical model passed the non-stiffness test.

4.3.2 Change of variable method

The work done in this thesis is a continuation of the work previously done in our research group. Mokarian-Tabari *et al.* studied the evaporation of toluene as a function of the vapour pressure. This work focused on the modelling of the late stage of the spin coating. The data was fitted to the Meyerhofer model using a change of variable. We used the same method to solve the Meyerhofer equation. According to Meyerhofer the rate of thinning of a spin coated film can be described with the following equation

$$\frac{dh}{dt} = -2kh^3 - e, \tag{4.31}$$

where $k = \frac{\omega^2}{3\nu}$ and e the evaporation rate. We define the variables

$$\begin{aligned} s &= Bt, \quad \text{and} \\ x &= Ah \end{aligned}$$

Using these variables the Meyerhofer equation can be rewritten as

$$\frac{d\left(\frac{x}{A}\right)}{d\left(\frac{s}{B}\right)} = -2k\left(\frac{x}{A}\right)^3 - e. \tag{4.32}$$

We define A and B in order that

$$\begin{aligned} k &= A^2B \quad \text{and,} \\ e &= \tfrac{B}{A}. \end{aligned}$$

Equation 4.32 can then be rewritten as

$$\frac{dx}{ds} = -2x^3 - 1. \tag{4.33}$$

This equation is then solved for $s(x)$ by integrating both sides

$$\int ds = \int \frac{dx}{-2x^3 - 1}. \tag{4.34}$$

$s(x)$ is equal to

$$s(x) = \frac{1}{2^{\frac{1}{3}}}\left(-2\sqrt{3}\text{ArcTan}\left(\frac{-1+\sqrt[3]{16x}}{\sqrt{3}}\right) - ln\left(\frac{(1+\sqrt[3]{2x})^2}{1-\sqrt[3]{2}x+\sqrt[3]{4}x^2}\right) + C. \right. \tag{4.35}$$

In Equation 4.35, C is a the constant of integration which is determined by using the boundary conditions which we take to be $x = 0$, $t = t_f$. These conditions apply only for the thinning of the solute free layer as once the solvent has evaporated the final thickness is equal to zero. According to the change of variable $s(x) = Bt$. We therefore deduce that

$$C = -\frac{1}{2^{\frac{1}{3}}}\left(-2\sqrt{3}\text{ArcTan}\left(\frac{-1}{\sqrt{3}}\right)\right) + Bt_f = \frac{\pi}{2^{\frac{1}{3}}\sqrt{3}} + Bt_f. \tag{4.36}$$

Substituting C in Equation 4.35, the solution to the Meyerhofer equation is given by

$$\begin{aligned} s(x) \quad = \quad & \frac{1}{2^{\frac{1}{3}}}\left(-2\sqrt{3}\text{ArcTan}\left(\frac{-1+\sqrt[3]{16x}}{\sqrt{3}}\right) - ln\left(\frac{(1+\sqrt[3]{2x})^2}{1-\sqrt[3]{2}x+\sqrt[3]{4}x^2}\right)\right) \\ & + \frac{\pi}{2^{\frac{1}{3}}\sqrt{3}} + Bt_f. \end{aligned} \tag{4.37}$$

Note that s is proportional to time and x is proportional to thickness. A plot of $s(x)$ shows a curve which describes time as a function of the thickness in h and t coordinates. In order to plot the curve that describes the thickness as a function of time we need to plot the parametric equation,

$$\begin{aligned} t &= \frac{s(x)}{B} \\ h &= \frac{x}{A}. \end{aligned}$$

We plot Equation 4.3.2 using *Mathemaitca 7*, the fitting parameters A and B are used to fit this curve to the experimental data.

4.4 Accuracy of the optosinometer

The correction terms in the RBD and the semi-empirical models are expected to give a better description of the early stage of spin coating. Spin coating of a solute-free liquid takes a couple of seconds. In the case of toluene spun at 1000 rpm under no controlled vapour pressure, the time necessary for the toluene to evaporate is 3 s. With such a fast process it is important to know how quickly the optospinometer reaches its final spin speed and the accuracy of the reflectivity data. With this purpose in mind we study the ramping up rate of the optospinometer. The centre of the spin coater is focused on the line separating two surfaces with different refractive indices. Figure 4.3 (a) shows the reflectivity data which comprise successive peaks and troughs. The features on this reflectivity curve are not due to a change in the thickness but a change in the refractive index. The spin coater reaches its final spin speed when the time elapsed between two successive peaks becomes constant. Figure 4.3 (b) is a plot of the time elapsed between two successive peaks versus time. After 0.06 s the time elapsed between two peaks reaches an average value. This means that after 0.06 s the spin coater has reach its final speed. The initial time will be taken as the first distinctive peak after 0.1 s.

4.5 Dynamics of a solute free layer

Studying the thinning rate of a polymer solution is more complex than studying the thinning rate of a solute free layer. For this reason we first investigate the thinning of a

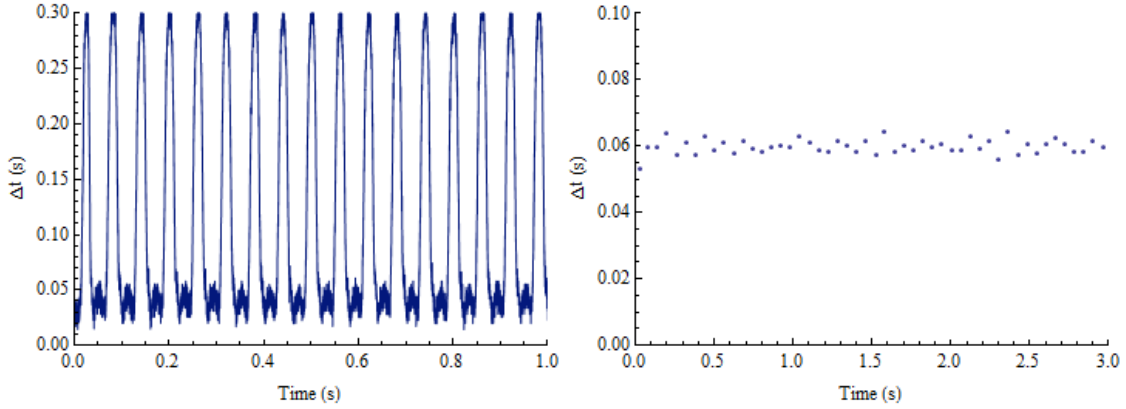

(a) (b)

FIGURE 4.3: a) Refelectivity curve showing the successive peaks and troughs due to a change in the refractive index. b) Plot of the time elapse between two peaks as a function of time

Bath temperature (°C)	Toluene vapour pressure (kPa)
no cell	0
2	3.5
6	2.6
10	2.3
14	1.8
18	1.5
22	1.2
26	0.8
no cell	0

TABLE 4.1: Table showing the temperature of the water bath, and the corresponding toluene vapour pressure in the cell

toluene layer. Table 4.1 shows the temperature of the water bath and the corresponding vapour pressure.

Figure 4.4 shows the experimental data obtained at all of the vapour pressures investigated. Note that the change in the vapour pressure does not affect the early stage of the coating. This is a nice illustration of the fact that mass transfer is negligible in this phase and that the thinning is governed by hydrodynamic forces. As the vapour pressure increases, longer drying times are necessary. This is a consequence of the slower evaporation rates.

In order to reduce the number of graphs and increase clarity we will study the result obtained for $p_v = 0$ kPa , $p_v = 0.8$ kPa , $p_v = 1.5$ kPa and $p_v = 3.5$ kPa. Figure 4.5 shows the fits to the experimental data for the three models reviewed here. The dot-dashed lines are the fits obtained using the Meyerhofer model; as one can see this model is in

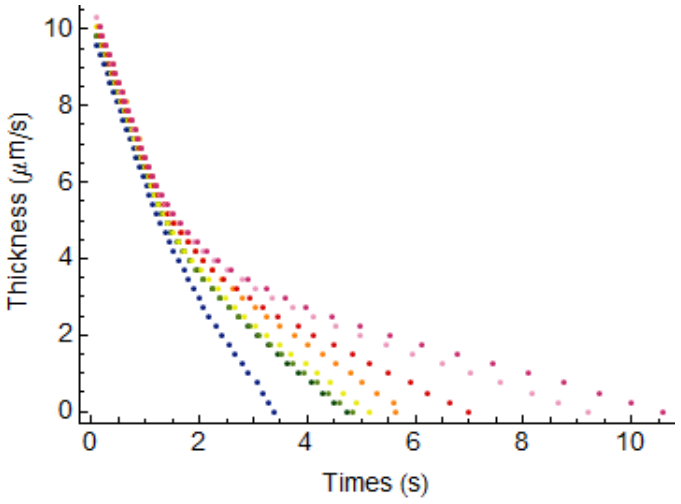

FIGURE 4.4: Experimental thickness time profile for toluene spin coated at 1000 rpm and different vapour pressures, $p_v = 0$ kPa (blue), $p_v = 0.8$ kPa (dark green), $p_v = 1.1$ kPa(light green), $p_v = 1.5$ kPa (yellow), $p_v = 1.8$ kPa (orange), $p_v = 2.3$ kPa (red), $p_v = 2.9$ kPa (pink) and $p_v = 3.5$ kPa (dark pink)

agreement with the data only in the late stage of the coating. The dashed lines are the fits obtained with the RBD model; at low vapour pressure there is a poor agreement between the results and the model in the early stage. However, as the vapour pressure increases the fits improve and good agreement is obtained between the model and the data. The solids lines are the fits obtained with the semi-empirical model. With this model the fits are in good agreement with the data regardless of the vapour pressure.

Knowing that the extra term in the RBD model and the semi-empirical model are velocity terms, we plot the velocity to understand the differences in the quality of the fits obtained. We defined the velocity terms for the three models

$$u_{z/\mathrm{RBD}} = -\frac{2}{3}\left(\frac{\rho\omega^2}{\eta}h^3 + \frac{\omega^4\rho^3}{\eta^3}\left[\frac{15e\eta}{24\rho\omega^2}h^4 - \frac{34}{105}h^7\right]\right), \tag{4.38}$$

$$u_{z/\mathrm{SE}} = -\frac{2\omega^2h^3}{3\nu} - \frac{W_0}{\exp(U^{t/\tau})} \quad \text{and} \tag{4.39}$$

$$u_{z/\mathrm{M}} = -\frac{2\omega^2h^3}{3\nu}. \tag{4.40}$$

Note that the first terms in $u_{z/\mathrm{SE}}$ and $u_{z/\mathrm{RBD}}$ are equal to $u_{z/\mathrm{M}}$. Figure 4.6 shows the plots of the three velocity terms as a function of time, note that they are all negative. This is because the velocity vector is downward and perpendicular to the substrate, whereas the $\overleftarrow{z}$ axis is defined as upward and normal to the substrate. Figure 4.6 (a)

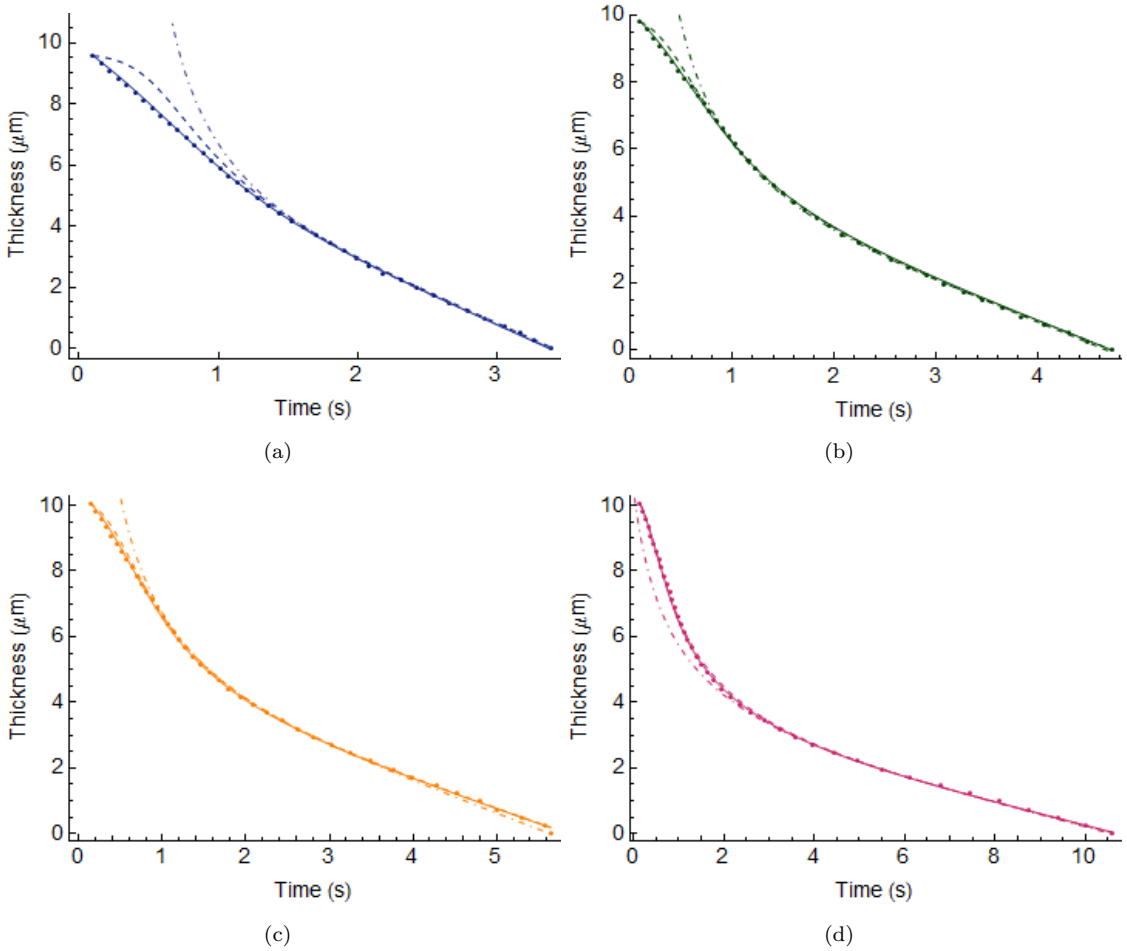

FIGURE 4.5: Thickness time profile of toluene spin coated at 1000 rpm at different vapour pressures. a) $p_v = 0$ kPa, b) $p_v = 0.9$ kPa, c) $p_v = 1.8$ kPa and d) $p_v = 3.5$ kPa. The dotted lines are the experimental data; the solid lines are the fits to the semi-empirical model; the dot-dashed lines are the fits obtained with the Meyerhofer model; and the dashed lines are the fits to the RBD model

is a plot of $u_{z/\mathrm{M}}$ which can be interpreted as follows; the vertical velocity of a thinning toluene layer decreases continuously until equal to zero. Figure 4.6 (b) shows $u_{z/\mathrm{RBD}}$ and $u_{z/\mathrm{SE}}$; these curves increase continuously until a maximum is reached and then they continuously decrease to zero. Rehg and Higgins investigated the effect of inertial forces during spin coating of a non evaporative liquid[58]. They proposed a model accounting for the inertial forces and compared it with the EBP model in which the axial velocity term is equal to $u_{z/\mathrm{M}}$. Their results revealed that the EBP model overestimates the radial velocity. Continuing this reasoning, $u_{z/\mathrm{M}}$ also overestimates the magnitude of the vertical velocity. This is clearly visible in Figure 4.6 where the magnitude of $u_{z/\mathrm{M}}$ is significantly higher than the magnitude of $u_{z/\mathrm{RBD}}$ and $u_{z/\mathrm{SE}}$. Rehg and Higgins plotted the vertical velocity at different cross section in the film as a function of time (see

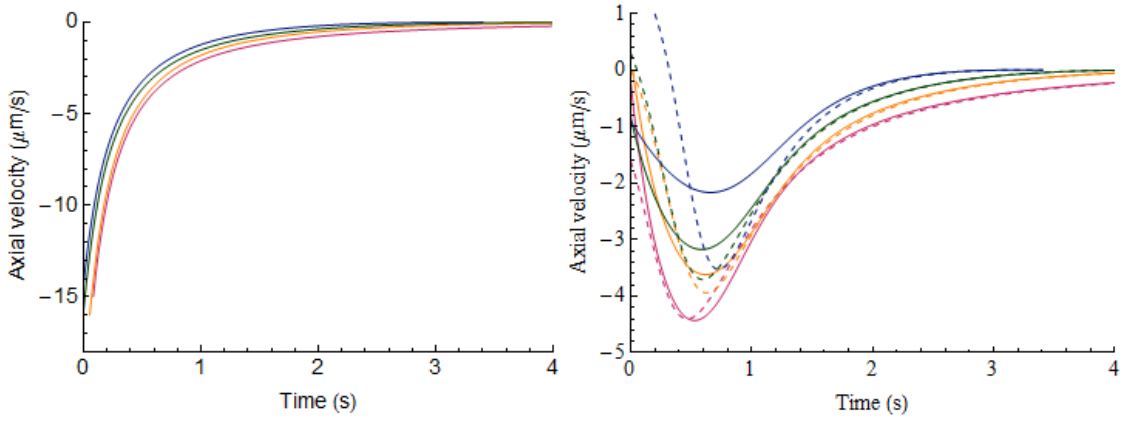

FIGURE 4.6: a) $u_{z/\mathrm{M}}$ of toluene spin coated at 1000 rpm, at different vapour pressures $p_{\mathrm{v}} = 0$ kPa (blue), $p_{\mathrm{v}} = 0.9$ kPa (green), $p_{\mathrm{v}} = 1.8$ kPa (orange) and $p_{\mathrm{v}} = 3.5$ kPa (dark pink). b) $u_{z/\mathrm{RBD}}$ and $u_{z/\mathrm{SE}}$ of toluene spin coated at 1000 rpm at different vapour pressures; $p_{\mathrm{v}} = 0$ kPa (blue), $p_{\mathrm{v}} = 0.9$ kPa (green), $p_{\mathrm{v}} = 1.8$ kPa (orange) and $p_{\mathrm{v}} = 3.5$ kPa (dark pink). The solid line show $u_{z/\mathrm{SE}}$ and the dashed line shows $u_{z/\mathrm{RBD}}$.

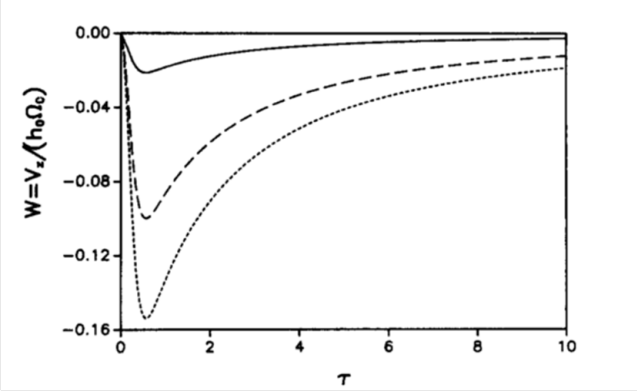

FIGURE 4.7: Dimensionless vertical velocity term versus dimensionless time. Reprinted from T. J. Rehg and B. G. Higgins, *Phys. Fluid.*, **31** 1361 (1988), with permission from AIP Publishing LLC

Figure 4.7) in which v_z is the axial velocity, W is the dimensionless axial velocity and τ is the dimensionless time. In a similar way to $u_{z/\mathrm{RBD}}$ and $u_{z/\mathrm{SE}}$, the vertical velocity increases rapidly and then decelerates gradually.

As the vapour pressure increases $u_{z/\mathrm{RBD}}$ and $u_{z/\mathrm{SE}}$ becomes closer and at the highest vapour pressure studied they overlap. In order to get a better understanding of how the inertial forces accounted for via the correction terms influence the dynamics of spin coating, we define and plot

$$c_{\mathrm{RBD}} = -\frac{2}{3}\left(\frac{\omega^4\rho^3}{\eta^3}\left[\frac{15e\eta}{24\rho\omega^2}h^4 - \frac{34}{105}h^7\right]\right) \quad \text{and} \tag{4.41}$$

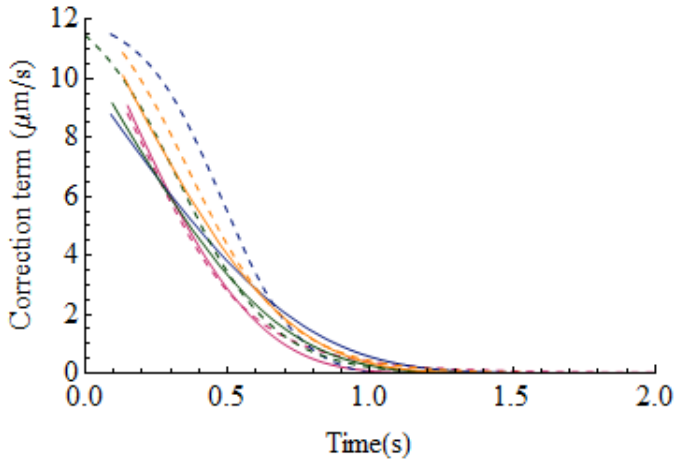

FIGURE 4.8: The correction terms on the vertical velocity of toluene spin coated at 1000 rpm at different vapour pressures $p_v = 0$ kPa (blue), $p_v = 0.9$ kPa (green), $p_v = 1.8$ kPa (orange) and $p_v = 3.5$ kPa (dark pink). The solid lines and the dashed lines show the semi-empirical and the Reisfled correction terms respectively.

$$c_{\mathrm{SE}} = -\frac{W_0}{\exp(U^{t/\tau})}, \tag{4.42}$$

where c_{RBD} is the RBD correction term and c_{SE} is the semi-empirical correction term; Figure 4.8 shows the plot of these correction terms. The dashed lines are the plots of c_{RBD} and the solid lines correspond to c_{SE}, they both continuously decrease very rapidly. After 1 s the correction terms for all the curves fitted are equal to zero. Contrary $u_{z/\mathrm{RBD}}$ and $u_{z/\mathrm{SE}}$ which are negative, c_{RBD} and c_{SE} are positive which means that they oppose the thinning, as one would expect from a term that accounts for the inertial forces.

In the following lines we are going to investigate why the fit obtained with the RBD model improves with the vapour pressure. RBD define, the Reynolds number as $\mathrm{Re} = \frac{U_o h_o \rho}{\eta}$. However Re for a liquid is defined as $\mathrm{Re}_{\mathrm{lq}} = \frac{h o^2 \omega}{\nu}$. Re and $\mathrm{Re}_{\mathrm{lq}}$ are related by

$$\mathrm{Re}_{\mathrm{lq}} = \sqrt{\mathrm{Re}}. \tag{4.43}$$

Using the fitting parameter obtained with the RBD model we calculate Re then deduce $\mathrm{Re}_{\mathrm{lq}}$ (see Table 4.2). The value of $\mathrm{Re}_{\mathrm{lq}}$ ranges between 2 to 1.5; these low Re numbers are in agreement with the value reported by Kreith *et al.*[66] who reported that in the early stage of the process $\mathrm{Re}_{\mathrm{lq}}$=6. According to Higgins, low $\mathrm{Re}_{\mathrm{lq}}$ does not mean that the viscous forces are dominant, but rather that the viscous and the centrifugal forces balance each other out [67]. Higgins defines

$$t_{eq} = \frac{\nu}{h o^2 \omega^2} \tag{4.44}$$

as the time after which the centrifugal forces are equivalent to the viscous forces. We remind the reader that the velocity term $u_{z/\mathrm{M}}$ was calculated by equating the viscous and centrifugal forces. From the definition of t_{eq} we conclude that for $t > t_{eq}$ the velocity term is dominated by $u_{z/\mathrm{M}}$ and the inertial forces are negligible. In Table 4.2 we report t_{eq} and t_{vmax}, the time at which the velocity reaches its maximum. At a given vapour pressure the two numbers are in good agreement. We concluded that graphically t_{eq} correspond to t_{vmax}, i.e. for $t > t_{eq} = t_{vmax}$, the inertial forces are negligible. This is supported by Figure 4.8. At $t = t_{vmax}$, the correction terms have decreased to more than half of their initial value. Regh and Higgins studied low and high Re number flows. As Re increases, inertial forces other than the centrifugal are important. They also reported that t_{eq} increased with Re and our experiments are in agreement with this statement; as the vapour pressure in the chamber increases, Re and t_{eq} decreases. As the vapour pressure increases, the time during which the inertial forces are important decreases whereas the total drying time increases; the toluene layer evaporates in 3 s when spin coated in a solvent free environment, whereas 10 s are necessary when coating with a vapour pressure of 3.5 KPa. Is the improvement of the fits obtained with the RBD model apparent due to the longer drying time? One way to answer to this question is to plot the reduced thickness profiles. Figure 4.9 shows the reduced thickness profiles at different vapour pressures. Although the fits obtained with the semi-empirical model are in good agreement with the data we still observed the improvement fits obtained with the RBD model. This confirms that the improvement of the RBD fits has a real effect and is not an artefact.

The lower the t_{eq}, the faster the rate of decay of the inertial forces and the better the fit obtained with the RBD model. We speculate that the fits from the RBD model improve when the inertial forces are weaker and when t_{eq} is shorter. t_{eq} is inversely proportional to the square of ω, and the centrifugal forces are proportional to the square of the spin speed. In order to verify our hypothesis we study the thinning of a toluene layer spun at 2000 and 3000 rpm.

Figure 4.10 (a) shows the fits obtained for a toluene layer spun at 2000 rpm and 3000 rpm. The two models are in excellent agreement with the experimental data. Figure 4.10 (b) is a plot of the velocity terms; the higher the spin speed the better the agreement between $u_{z/\mathrm{RBD}}$ and $u_{z/\mathrm{SE}}$. Figure 4.10 (c) is a plot of the correction term; as expected the decay rate of C_{RBD} and C_{SE} increases with the spin speed. Note also that the time

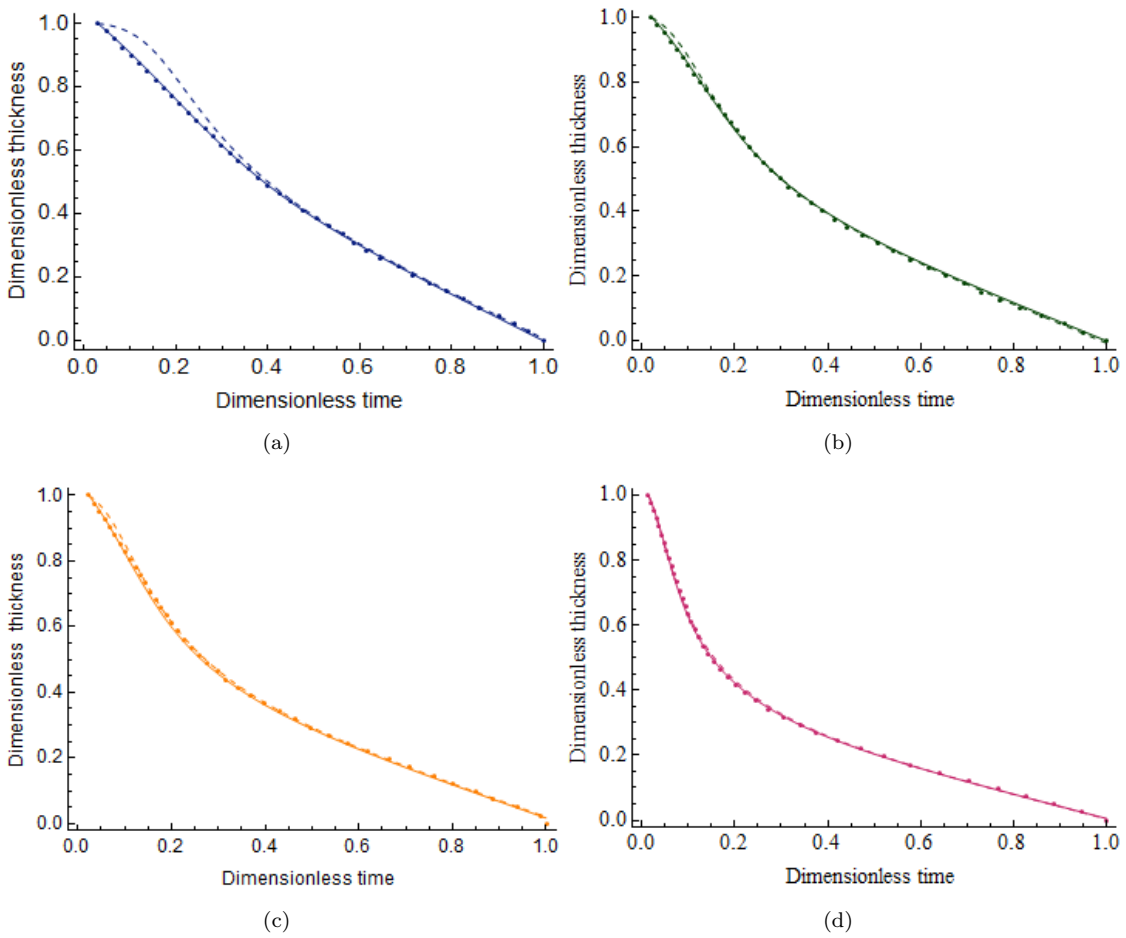

FIGURE 4.9: Dimensionless thickness time profile of toluene spin coated at 1000 rpm at different vapour pressure. a) $p_v = 0$ kPa, b) $p_v = 0.9$ kPa, c) $p_v = 1.8$ kPa and d) $p_v = 3.5$ kPa. The dotted lines are the experimental data; the solid lines are the fits to the semi-empirical model; the dot-dashed lines are the fits obtained with the Meyerhofer model; and the dashed lines are the fits to the RBD model

Vapour pressure (kPa)	Re	Re_{lq}	t_{vmax} (s)	t_{eq} (s)
3.5	1454	1.56	0.51	0.58
2.6	1561	1.60	0.51	0.55
2.3	1668	1.65	0.62	0.61
1.8	1941	1.79	0.61	0.58
1.5	1884	1.77	0.51	0.58
1.2	2108	1.85	0.57	0.60
0.8	2157	1.87	0.58	0.61
no cell	3021	2.20	0.65	0.64

TABLE 4.2: Table reporting the values of t_{eq}, t_{vmax}, Re_{lq}, and Re of toluene spin coated at 1000 rpm as a function of the vapour pressure. t_{vmax} is the time at which the maximum in the velocity is reached, beyond this time the magnitude of the inertia forces are negligible. The values of Re_{lq}, and Re were calculate using the RBD model.

ω (rpm)	Re	Re_{lq}	t_{vmax}(s)	t_{eq}(s)
1000	3021	2.20	0.65	0.63
2000	2794	1.8	0.26	0.25
3000	2622	1.72	0.12	0.14

TABLE 4.3: Table reporting t_{eq}, t_{vmax}, Re_{lq}, and Re of toluene as a function of the spin speed.t_{eq} was calculated using Equation 4.44. t_{vmax} was determined graphically. Re was The values of Re were calculated using the RBD model, from which Re_{lq} was deduced

at which the correction term cancels out decreases with increasing spin speed. t_{vmax} and t_{eq} are reported in Table 4.3; they both decrease as the spin speed increases and they are in good agreement with each other. We conclude that the RBD model is adequate to describe the thinning of a film which experiences weak inertial forces. In Table 4.3 we also report the Re and Re_{lq}; they decrease as the spin speed increases. The flow of a liquid with high Re number experiences inertial forces other than centrifugal ones. This could be one of the reasons why the fit obtained with the RBD model deteriorates as Re increases. The Meyerhofer model overestimates the radial out flow because its does not take account of the inertial forces.

There are couple of interesting points to note; the first one is that the maximum magnitude reached in the velocity curve (see Figure 4.6 (b)) increases with the vapour pressure. Regh and Higgins studied the effect of shear forces for a non-evaporative layer. They reported that the thinning rate rises when the overlaying layer is a gas [58]. All the models studied here assume zero shear rate. However, as the density of toluene vapour increases, the motion of the spin coater affects that of the overlaying toluene vapour, which in its turn enhances the thinning rate of the film, which explains the increase in the maximum velocity reached. The second interesting point is that despite the increasing velocity, when the vapour pressure is increased, the time necessary for the toluene to dry is longer (see Figure 4.11 (a)). This is due to the short duration of the phase where the velocity term dominated the process. Figure 4.6 shows that after 2s the axial velocity is negligible. From this point in time the process is dominated by the solvent removal which is controlled by the solvent molecule on the top layer of the film and by the solvent concentration above the film. The high density of toluene in the chamber creates a resistance to the mass transfer and the evaporation rate decreases (Figure 4.11 (b)). As a result, the duration of the phase where the evaporation dominates the thinning increases, therefore decreasing the net thinning rate, which explains the longer drying time. The rates of evaporation were calculated by averaging the values obtained with

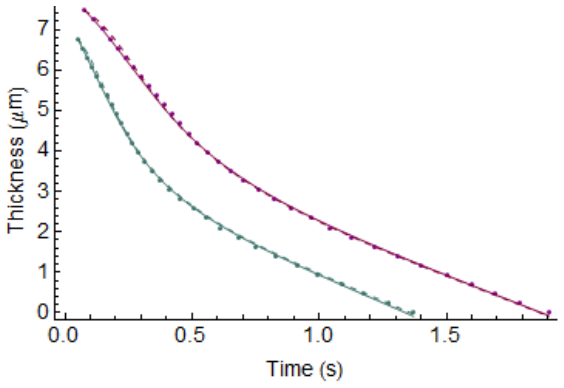

(a)

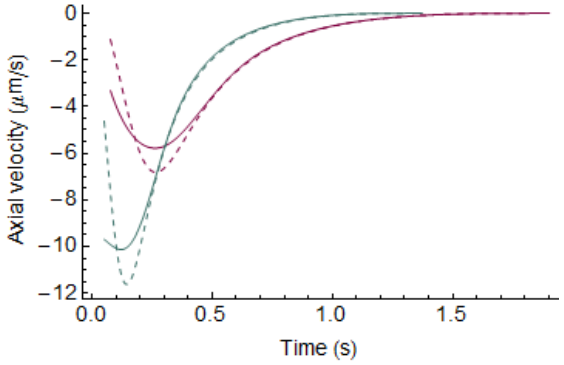

(b)

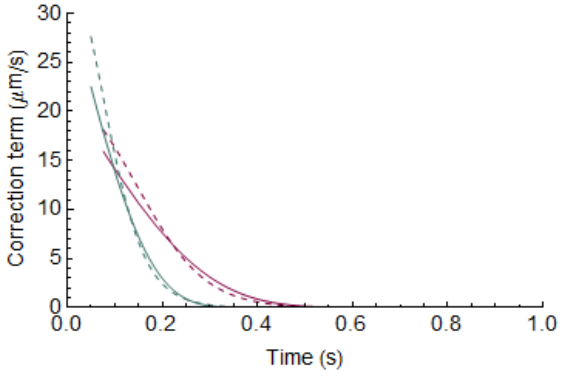

(c)

FIGURE 4.10: a) Thickness time profile of toluene spin coated at different spin speeds. b) Axial velocity of toluene spin coated at different spin speeds. c) Correction term on the vertical velocity of toluene spin coated at different spin speeds. The purple and the light blue designate the films spun at 2000 rpm and 3000rpm, repectively. The dotted lines are the experimental data; the solid lines are the fits to the semi-empirical model and the dashed lines are the fits to the RBD model.

the RBD, the Meyerhofer and the semi-empirical models. The small error bars on Figure 4.11 (b) show that the evaporation rates are in agreement. We studied how the evaporation rate changes with the spin speed. The results are shown in Figure 4.11 (c). The evaporation rate increases due the stronger centrifugal forces. Meyerhofer was the first to report that the evaporation rate related to the spin speed by

$$e = C_e\sqrt{\omega} \tag{4.45}$$

where C_e is the constant of evaporation which takes into account parameters such as the vapour pressure , the solvent diffusion rate, the viscosity and the density of the layer above the thinning film. The solid line is a fitting curve with an equation of $0.166\sqrt{\omega}$. As far as we know there is no available value for the constant of evaporation of toluene. However the constant of evaporation for ethanol, THF and CB were reported to be equal to 0.13, 0.74 and 0.055 $\mu(rad.s)^{-\frac{1}{2}}$ respectively [8]. The evaporation rate of toluene is lower than that of ethanol and THF, and higher than that of CB. Even though the value of C_e for ethanol is lower than that of toluene, the other values are in good agreement with the value that we calculated.

4.6 Dynamics of liquid and solute layer

In the previous section we showed that the Meyerhofer model is not suitable to describe the early stage of spin coating. As a consequence in this section, the data is fitted with the RBD model and the semi-empirical model. As explained previously an accurate descriptions of the dynamics of a spin coated polymer film needs to take into account the changes in viscosity as a function of the concentration. During the coating the viscosity increases rapidly and continuously. However the velocity term which contains the viscosity is important only in the early stage of the coating. As a result the expression chosen to express the viscosity should be the one that will describe more appropriately the viscosity of the polymer solution. The polymer solutions spin coated are in the semi-dilute regime; therefore we choose to express the viscosity as

$$\eta(t) = \eta_s(1 + [\eta]\phi(t) + k'[\eta]\phi(t)^2), \tag{4.46}$$

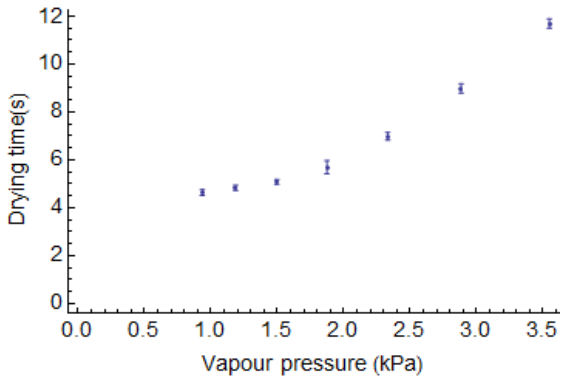

(a)

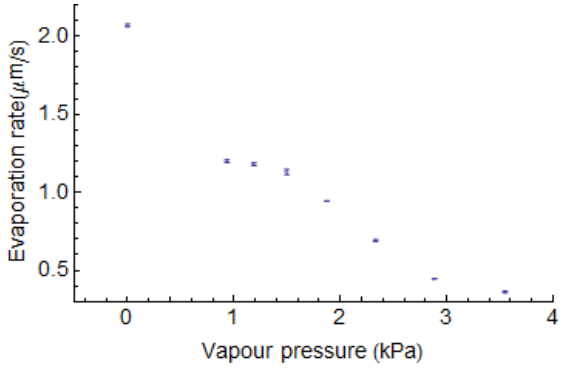

(b)

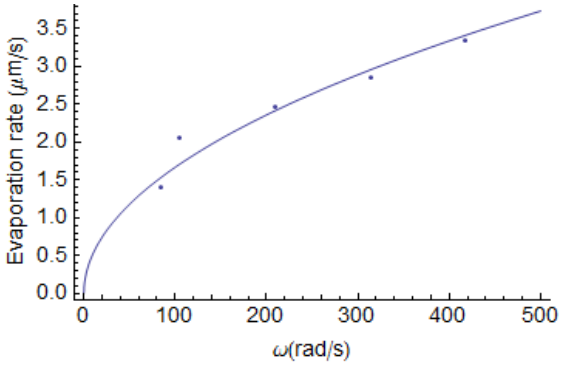

(c)

FIGURE 4.11: a) Toluene evaporation rate of toluene spin coated at 1000 rpm as a function of the toluene vapour pressure in the chamber. b) Time necessary for a toluene layer spin coated at 1000 rpm to dry as a function of the toluene vapour pressure in the chamber. c) Rate of evaporation of toluene during the spin coating of a toluene layer as a function of the spin speed

where $\eta(t)$ is viscosity of the polymer solution, η_s is the solvent viscosity,k' is the Huggins constant and ϕ the polymer volume fraction. For all solutions studied, the third term in Equation 4.46 can be neglected. The polymer volume fraction at a given time t is expressed as

$$\phi(t) = \frac{h_f}{h(t)}, \tag{4.47}$$

where h_f is the thickness of the dry film. Equation 4.47 is substituted in Equation 4.46 which in its turn is substituted into semi-empirical model (Equation 4.1) and the RBD model (Equation 4.11), which can be rewritten as

$$\frac{\partial h}{\partial t} + e + \frac{2\omega^2\rho h^3}{3\eta\left(1+[\eta]\frac{h_f}{h(t)}\right)} + \frac{W_0}{\exp(U^{t/\tau})} = 0 \quad \text{and} \tag{4.48}$$

$$\frac{\partial h}{\partial t} + e + \frac{2}{3}\left(\frac{\rho\omega^2}{\eta\left(1+[\eta]\frac{h_f}{h(t)}\right)}h^3 + \frac{\omega^4\rho^3}{\eta\left(1+[\eta]\frac{h_f}{h(t)}\right)^3}\left[\frac{15e\eta\left(1+[\eta]\frac{h_f}{h(t)}\right)}{24\rho\omega^2}h^4 - \frac{34}{105}h^7\right]\right) = 0. \tag{4.49}$$

Figure 4.12 shows the fits obtained with the RBD model and the semi-empirical model for different systems. Figure 4.12 (a), (b) and (c) show the fits for the thinning of PS films, PMMA films and films made of a blend of PS and PMMA at different vapour pressures. The solids lines are the fits obtained with the semi-empirical model. For all the polymer films investigated, the semi-empirical model is in good agreement with the experimental data. The fits obtained with the RBD model are in agreement with the experimental data only at the late stage of the coating and no improvement of the fits were observed as the vapour pressure increased.

We defined the velocity terms as being equal to

$$u_{z/\mathrm{SE}} = -\frac{2\omega^2\rho h^3}{3\eta\left(1+[\eta]\frac{h_f}{h(t)}\right)} - \frac{W_0}{\exp(U^{t/\tau})} \quad \text{and} \tag{4.50}$$

$$u_{z/\mathrm{RBD}} = -\frac{2}{3}\left(\frac{\rho\omega^2}{\eta\left(1+[\eta]\frac{h_f}{h(t)}\right)}h^3 + \frac{\omega^4\rho^3}{\eta\left(1+[\eta]\frac{h_f}{h(t)}\right)^3}\left[\frac{15e\eta_s\left(1+[\eta]\frac{h_f}{h(t)}\right)}{24\rho\omega^2}h^4 - \frac{34}{105}h^7\right]\right). \tag{4.51}$$

Figure 4.13 shows the plot of $u_{z/\mathrm{SE}}$ and $u_{z/\mathrm{RBD}}$. The interpretation of this graph suggests that unlike $u_{z/\mathrm{SE}}$, $u_{z/\mathrm{RBD}}$ underestimates the resistance to the thinning due to inertia. Note that as the vapour pressure increases the maximum velocity reached increases. This is a consequence of the shearing forces. We define the correction term for the two

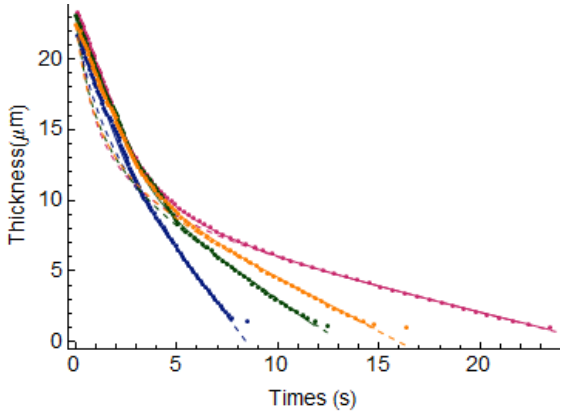

(a)

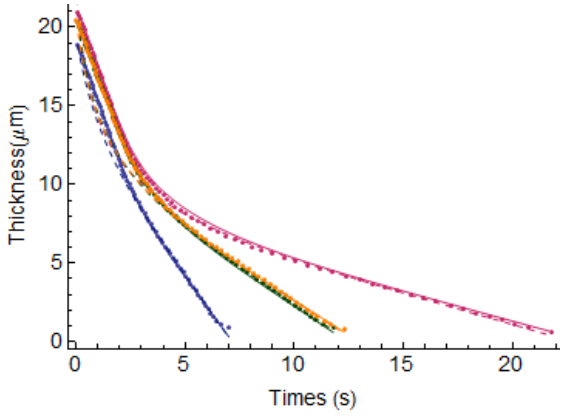

(b)

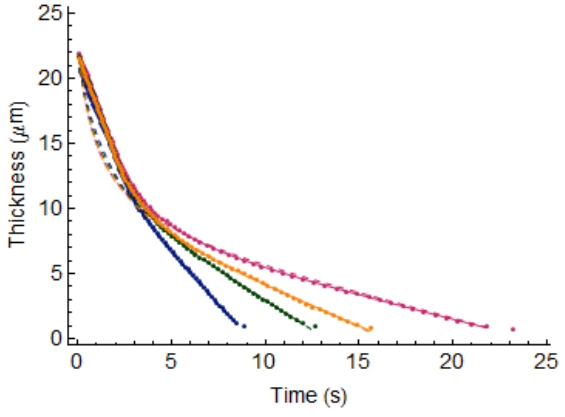

(c)

FIGURE 4.12: a) Thickness time profile of films coated from a solution made of 10% PS and 90% of toluene spin coated at 1000 rpm at different vapour pressures of toluene. b) Thickness time profile of films coated from a solution made of 10% PMMA and 90% of toluene spin coated at 1000 rpm at different vapour pressures of toluene. c) Thickness time profile of films coated from a solution made of 5% PS, 5% PMMA and 90% of toluene spin coated at 1000 rpm at different vapour pressures of toluene. The colours blue, green, orange and pink are associated to $p_v = 0$ kPa, $p_v = 0.9$ kPa, $p_v = 1.8$ kPa and d) $p_v = 3.5$ kPa . The dotted lines are the experimental data; the solid lines are the fits to the semi-empirical model and the dashed lines are the fits to the RBD model.

models as being equal to

$$c_{\mathrm{SE}} = -\frac{W_0}{\exp(U^{t/\tau})}, \quad \text{and} \tag{4.52}$$

and

$$c_{\mathrm{RBD}} = -\frac{\omega^4\rho^3}{\eta\left(1+[\eta]\frac{h_f}{h(t)}\right)^3}\left[\frac{15e\eta\left(1+[\eta]\frac{h_f}{h(t)}\right)}{24\rho\omega^2}h^4 - \frac{34}{105}h^7\right]. \tag{4.53}$$

Figure 4.13 (b) and (c) shows c_{RBD} and c_{SE}. c_{RBD} is significantly lower than c_{SE}. We conclude that the RBD model underestimates the inertial forces. The fits with the RBD model do not improve as the spin speed increased (see Figure 4.13 (d)). The plot of c_{SE} and c_{RBD} revealed that the poor fits are also due to the underestimation of the deceleration of the thinning. As a consequence the fits obtained on the late stage of the process are better than the ones obtained in the early stage. The semi-empirical model, by contrast gives a good fit to all of the data.

4.6.1 Effect of the vapour pressure on the evaporation rate, the final thickness and the drying time

Using the fits obtained with the two models we plot the evaporation rate from the polymer films as a function of the vapour pressure. The small error bars reflect the excellent agreement between the rates calculated from the two models (see Figure 4.14 (a)). At a low vapour pressure the evaporation rate from a toluene layer is always higher than the evaporation from the polymer films. The rate of evaporation relates to the mass transfer coefficient k_e by the following equation

$$e = k_e(x_{z=h} - x_\infty) \tag{4.54}$$

where $x_{z=h}$ is the solvent mass fraction on the top layer of the film and x_∞ is the solvent mass fraction above the film. k_e includes the solvent diffusion in the overlaying gas, the spin speed and other parameters that characterise the overlaying layer. Here we control x_∞. This implies that at a given vapour pressure the changes in the rate of evaporation are mainly due to $x_{z=h}$, which depends on the diffusion rate of the solvent molecules in the polymer network. During the thinning of a toluene layer, diffusion is not a barrier to the mass transfer; as a result the evaporation rate is always higher from the toluene films. Subsequently the toluene film dries faster (see Figure 4.14 (c)). The evaporation rates from the film made of a blend of PS and PMMA are the slowest. We speculate

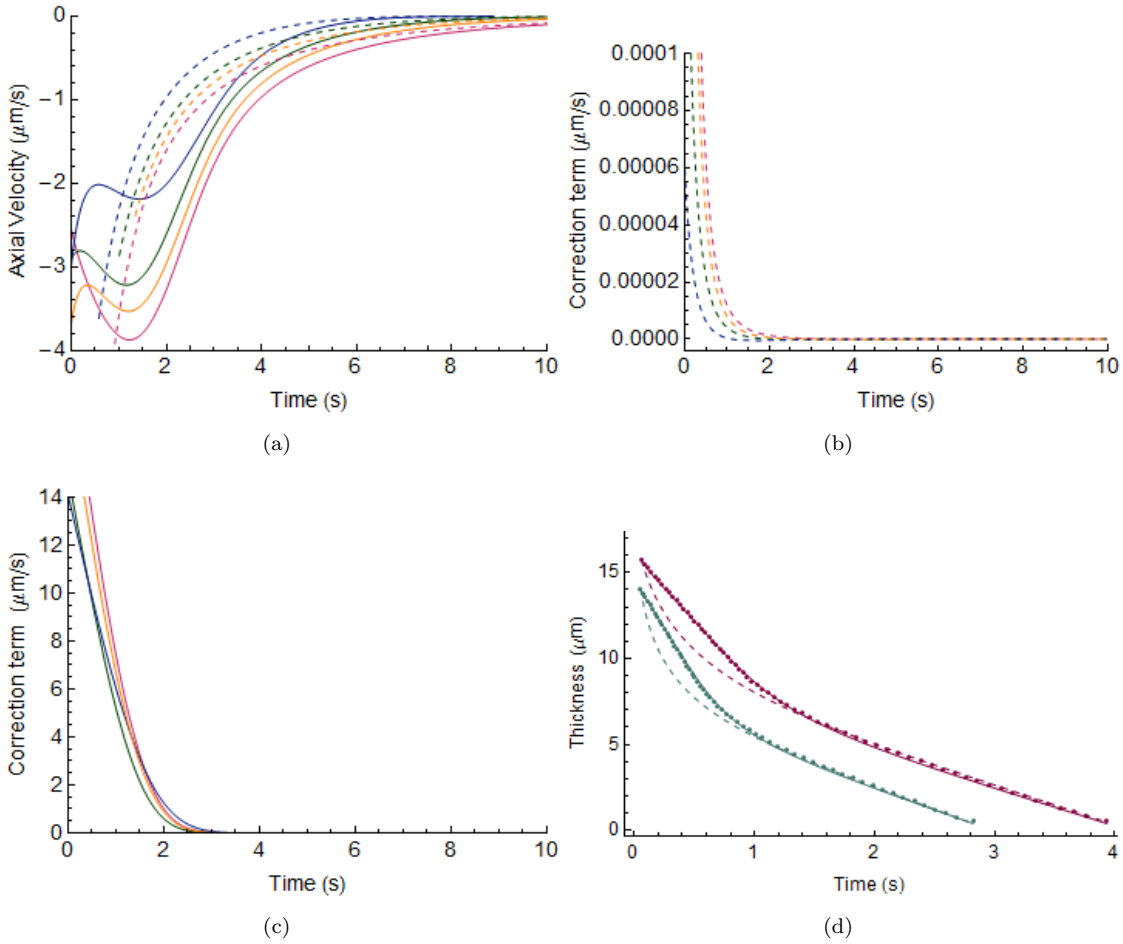

FIGURE 4.13: a) Axial velocity of films coated from a solution of 5% PS, 5% PMMA and 90% of toluene at different vapour pressures of toluene. b) RBD correction term on the vertical velocity of films coated from a solution of 5% PS, 5% PMMA and 90% of toluene at different vapour pressures of toluene. c) Semi-empirical correction term on the vertical velocity of films coated from a solution of of 5% PS, 5% PMMA and 90% of toluene at different vapour pressures of toluene. In figures a), b) and c) the films are spin coated at 1000 rpm and the colours blue, green, orange and pink are associated to the toluene vapour pressues $p_v = 0$ kPa, $p_v = 0.9$ kPa, $p_v = 1.8$ kPa and $p_v = 3.5$ kPa. d) Thickness time profile of films coated from a solution made of 5% PS, 5% PMMA and 90% of toluene at spin speed of 2000 rpm (purple) and 3000 rpm (light blue). In figure d) the dotted lines are the experimental data; the solid lines are the fits to the semi-empirical model and the dashed lines are the fits to the RBD model

that this is a consequence of repulsive interactions between the PS and PMMA films which complicates the motion of the polymer chains and the solvent molecules, therefore reducing the diffusions rate of solvent molecule to the top layer. It was reported that smaller the evaporation is, the thinner the film. This is in agreement with Figure 4.14 (b) which is a plot of the thickness of the dry film as a function of the vapour pressure. On this plot one can see that the films made of PS and PMMA are always thinner than those made of the homopolymers PS and PMMA.

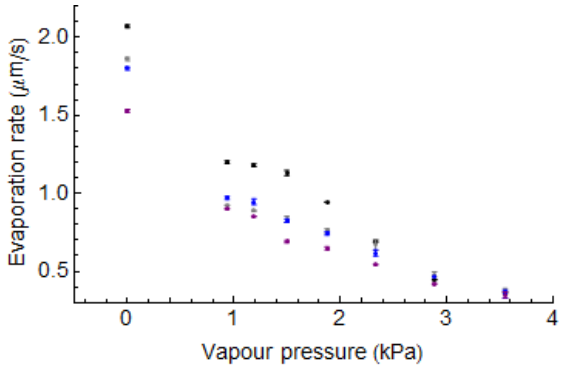

(a)

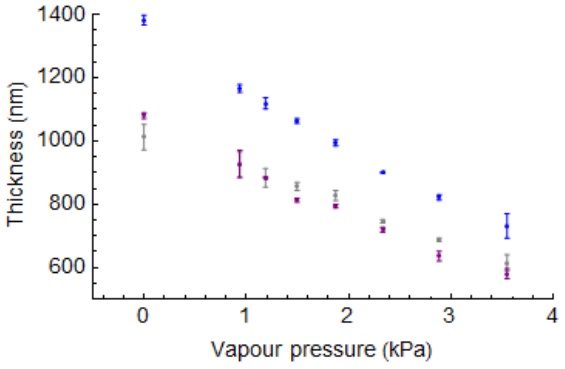

(b)

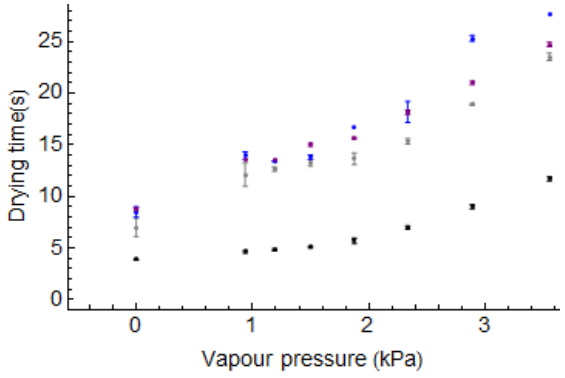

(c)

FIGURE 4.14: a) evaporation rate of toluene as a fucntion of the toluene vapour pressure in the environemental cell during the spin coating a toluene layer (black), PMMA solution (gray), PS solution (blue) and a blend of PS and PMMA (purple). b) as cast film thickness as a function of the toluene vapour pressure for PMMA solution (gray), for PS solution (blue) and a blend of PS and PMMA (purple). c) time necesssary for films to dry as a function of vapour pressure of toluene in the environemental cell during the spin coating a toluene layer (black), PMMA solution (gray), PS solution (blue) and blends of PS and PMMA (purple). In a), b) and c) the PMMA solution contained 10% PMMA and 90% toluene, the PS solution contained 10% PS and 90% toluene and the blend solution contained 5%PMMA, 5% PS and 90% toluene and the films were all coated at 1000 rpm.

As the concentration of toluene in the overlaying layer increases, the evaporation rates decrease and at the highest vapour pressure the evaporation rates from the toluene, PS, PMMA, and PS and PMMA films are equal. This suggests that regardless of the diffusion of toluene in the film, the mass fraction of toluene in the chamber is so high that the resistance to the mass transfer that it creates dictates the rate of evaporation. Despite the similar evaporation rate from the homopolymer films of PS and PMMA, the PS films are significantly thicker than the PMMA film; this was also reported elsewhere [68]. The difference in thickness is believed to be a consequence of the better affinity between PS chains and the toluene molecules leading to higher solvent retention. Gu *et al.* [69] studied solvent retention in PS films coated from toluene and reported the presence of solvent in the dry film. There is no similar experience reported for PMMA films that would enable us to have a definite conclusion. One way to verify this would be to perform gas chromatography on the films. In this procedure the polymer film is dissolved in a good solvent which is different from the one from which the film was coated. Gas chromatography is then used to determine the solvent content in the film.

4.6.2 Viscosity during spin coating

In this section we discuss the rheology and the viscosity of the film during coating by looking at the results obtained during the coating of PS and PMMA films. On Figure 4.12 (c) one can observe that at each vapour pressure the last datum is not fitted and that the final thickness modelled is lower than the experimental final thickness. Experimentally, the assumption of zero solvent remaining in the final film is shown to be inadequate. The polymer volume fraction and the relative viscosity are plotted only in the range where the experimental data are in agreement with the modelling, which is why the final volume fraction of polymer is less than unity (Figure 4.15). Figure 4.15 (b) shows the relative viscosity η/η_s at various vapour pressures, the curves are superimposed in the phase where the hydrodynamics dominates the process; this is due to the fact that very little solvent is lost in this phase. In the second phase of the process where the evaporation is dominant the polymer volume fraction increases at a slower rate when the vapor pressure in the cell increases; this is because the evaporation rate decreases significantly. According to Equation 4.46 the viscosity is linearly dependent on the concentration, this is valid only for diluted polymer solutions. One would expect the viscosity to depend on the concentration with a higher power once the polymer

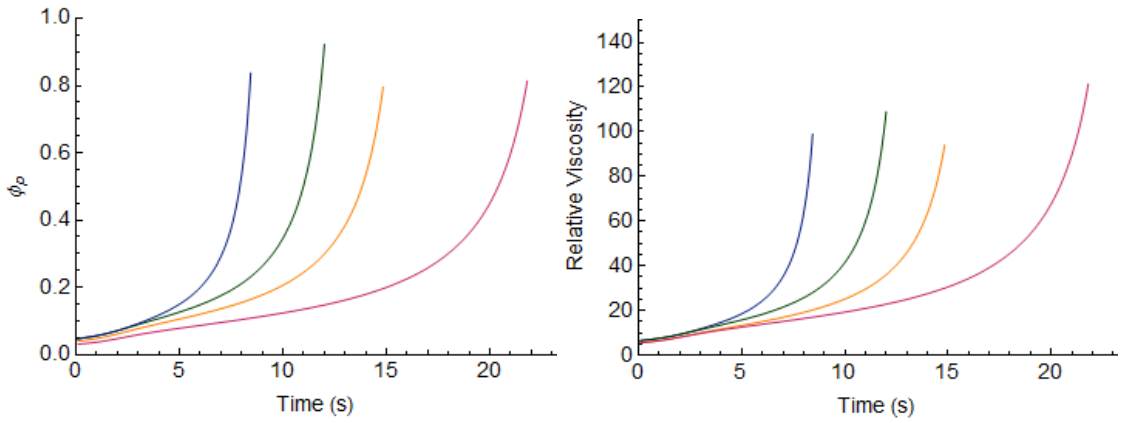

(a) (b)

FIGURE 4.15: a) Time dependence of the polymer volume fraction (ϕ_p) in films coated from a solution with 5% PS, 5% PMMA and 90% toluene, spin coated at 1000 rpm in different vapour pressures of toluene. b) relative viscosity as a function of time in films coated from a solution of 5% PS, 5% PMMA and 90% toluene spin coated at 1000 rpm in different vapour pressures of toluene. The colors blue, green, orange and pink correspond to $p_v = 0$ kPa, $p_v = 0.9$ kPa, $p_v = 1.8$ kPa and $p_v = 3.5$ kPa, respectively.

concentration is higher than the entanglement concentration. How can we explain the agreement between the data and Equation 4.46? The answer to this question lies in the fact that spin coating is a two stages process. Comparing Figure 4.13 (a) and Figure 4.15 (a), one can see that the rate of increases of the polymer volume fraction is significantly higher once the vertical velocity is negligible. Therefore the fact that Equation 4.46 underestimates the viscosity doesn't matter because the radial outflow is negligible.

From the numerical modelling we find that the initial polymer solution has a viscosity of 3.6 mPa s. This is significantly different to the ranges studied in other experiments where solutions of $1400 - 7000$ mPa s have been studied in one case [70] and $0.015 - 0.031$ mPa s in another [52]. Non-Newtonian behaviour arises in concentrated polymer solutions. The low viscosity of the initial solution and the fact that the velocity term (viscosity) is only important in the early stages of the coating justifies the assumption of a Newtonian fluid.

In summary, in this chapter we showed that the Meyerhofer model is not adequate to describe the thinning of a spin coated liquid layer or a polymer solution. The RBD is a good model to describe the thinning of a solute free layer which experiences weak inertial forces. However the correction term in the RBD model underestimates the strength of the inertial forces when spin coating a polymer solution. We proposed a semi-empirical model that gives a good description of the dynamics of a solute free layer and solute and

liquid layer. This model will become useful in the next section where we will combine it with the Flory-Huggins model to discuss the thermodynamics of spin coated films.

Chapter 5

Thermodynamics of spin coated films of PS and PMMA at 21°C

In this chapter we aim to give a better understanding of phase separation in thin films. We are aiming to correlate the phase separation of a ternary solution made of PS, PMMA and toluene with the thermodynamics of films coated from this mixture. This chapter is organised into two sections. Section 5.1 discusses the phase separation in bulk polymer solutions; we determine the bulk cloud point of PS, PMMA and toluene at 21°C. In section 5.2 we will use the semi-empirical model to calculate the solvent volume fraction of toluene on the film during coating. This information is then used to apply the Flory-Huggins theory during spin coating.

5.1 Cloud point of a bulk solution of PS and PMMA dissolved in toluene at 21°C

To determine the concentration at which a mixture of PS and PMMA phase separates at 21°C, the absorbances of solutions of known concentration were measured while the temperature was kept constant. The solutions studied have toluene volume fractions of 90%, 88% and 86% and an equal amount of PS and PMMA. All the solution studied here are in the semi-dilute regime where the chains overlap. Figure 5.1 shows the absorbance of PS and PMMA solutions as a function of the toluene volume fraction. At 21°C the solution with 84% toluene content has an absorbance significantly higher than that of

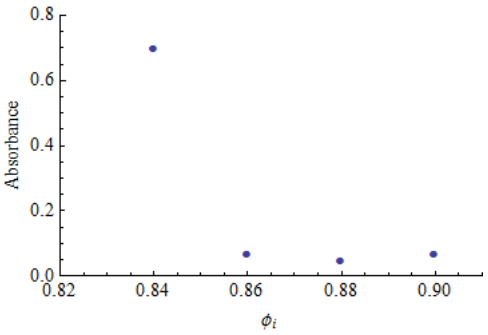

FIGURE 5.1: Light absorption of bulk ternary solution of PS, PMMA and toluene as a function of the toluene volume fraction. In each solution the volume fraction of PS and PMMA is kept constant.

the solutions containing higher toluene content. This suggests that the solutions at 90%, 88% and 86% of toluene content are in a single phase region at 21°C and that a ternary solution PS (M_w=96 Kg mol^{-1}), PMMA (M_w=106 Kg mol^{-1})and toluene enters the two phase region when the toluene volume fraction is lower than 84%.

5.2 Thermodynamics of spin coated films

The quality of the optospinogram are used to determine the range of concentrations studied. The peaks on the optospinogram of films coated from solutions with a solvent content lower than 86% were not distinct. The turbidity of a polymer solution and the morphology of a spin coated film are temperature dependent. In order for the comparison between the UV-visible data and the off-specular data to be relevant the temperature is kept at 21°C during the coating. The solutions studied here have an equal amount of PS and PMMA, therefore we define the volume fraction of polymer ϕ_{p}; as being equal to ϕ_{pmma} and ϕ_{ps}. The toluene volume fraction is defined as $\phi_{\mathrm{to}} = 1 - \phi_{\mathrm{p}}$. In the case of a thin films ϕ_{p} and ϕ_{to} can be approximated by

$$\phi_{\mathrm{p}} = \frac{h_f}{2h(t)} \quad \text{and} \tag{5.1}$$

$$\phi_{\mathrm{to}} = 1 - \frac{h_{\mathrm{f}}}{h(t)}. \tag{5.2}$$

Flory-Huggins theory is a simple means of describing the thermodynamics of polymer solutions. The free energy depends on the volume fraction of the components, the interaction parameters and the molecular weights. During spin coating, polymer films

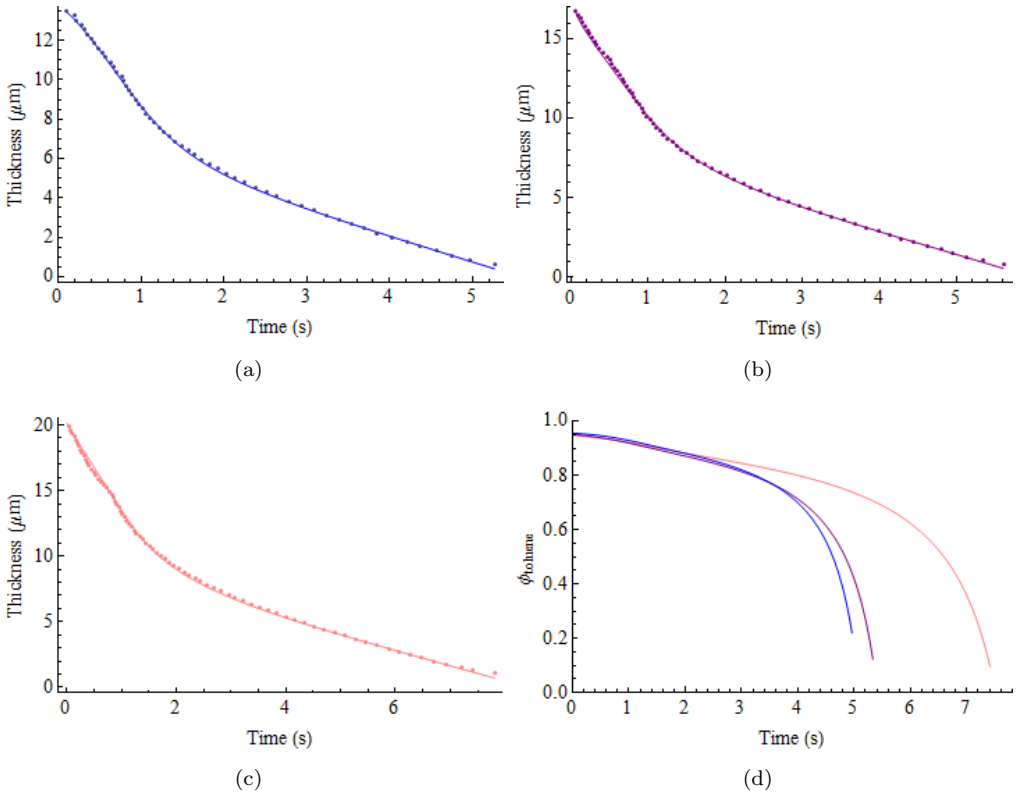

FIGURE 5.2: a) Thickness versus time curves for films coated from solutions of 5% PS, 5% PMMA and 90% toluene. b) Thickness versus time curves for films coated from solutions of 6% PS, 6% PMMA and 88% toluene. c) Thickness versus time curves for films coated from solutions of 7% PS, 7% PMMA and 86% toluene. d) Toluene volume fraction in the films as a function of time; the blue, purple and pink curves correspond to the film coated from the polymer solution with 90%, 88% and 86% toluene. In a), b) and c) the films were spin coated at 2000 rpm

are dynamic systems where the concentrations and the interaction parameters are time dependent. As seen in section 2.1 χ is inversely proportional to the temperature and also depends on the concentration [71–74]. In the case of a polymer dissolved in a good solvent χ is not dependent on the concentration [75, 76]. During the coating the relative amount of PS and PMMA are always equal therefore $\chi_{ps/pmma}$ is constant. As the solvent evaporates $\chi_{ps/to}$ and $\chi_{pmma/to}$ changes. Koningsveld *et al.* [72, 77] proposed an expression for χ which account for the concentration dependence. However the physical meaning of the additional terms is not clear. χ is a phenomenological term and the concentration dependence is accounted for only when the experimental data cannot be understood. Here we consider that the interaction parameters are constant and the results presented below show that this assumption is good enough to describe our results.

The interaction parameters of the system studied are equal to $\chi_{\mathrm{ps/pmma}}$= 0.041 [78], $\chi_{\mathrm{ps/to}}$=0.44 and $\chi_{\mathrm{pmma/to}}$=0.409 [18, 21]. Using Equation 5.1 and 5.2, the Flory-Huggins equation during spin coating can be expressed as

$$\frac{\triangle G_{\mathrm{mix}}}{k_{\mathrm{B}T}} = \frac{h_{\mathrm{f}}}{h(t)} \ln\left[\frac{h_{\mathrm{f}}}{2h(t)}\right]\left(\frac{1}{N_{\mathrm{ps}}} + \frac{1}{N_{\mathrm{pmma}}}\right) + \frac{h_{\mathrm{f}}(h(t)-h_f)}{2h(t)^2}(\chi_{\mathrm{pmma/to}} + \chi_{\mathrm{ps/to}}) + \frac{h_f^2}{4h(t)^2}\chi_{\mathrm{ps/pmma}}, \tag{5.3}$$

Figure 5.2 (a), (b) and (c) show the thickness profile curves for the films cast from polymer solutions with 90%, 88% and 86% toluene. The dots are the experimental data and the solid lines are the fits obtained with the semi-empirical model. The time necessary for the film to dry increases with the concentration of the solution. Figure 5.2 (d) shows the temporal evolution of the solvent volume fraction. The initial toluene volume fraction is unchanged as the polymer concentration increases. This error is due the assumption that there is no solvent retention in the film. As the concentration of the coated solution increases, solvent retention increases leading to a larger error in the toluene volume fraction. The solvent volume fraction is plotted only in the range where $h(t) > h_f$, because when $h(t) < h_{\mathrm{f}}$, ϕ_{to} is a negative.

Figure 5.3 shows the free energy of mixing plotted using Equation 5.3 and the off-specular scattering profiles. A minimum in the free energy is observed and the time at which this minimum is reached is defined as $t_{\triangle \mathrm{Gmin}}$. In the off-specular scattering profile $t_{\triangle Gmin}$ is marked by a red line. Previous research in our group revealed that prior to the lateral phase separation in PS and PMMA films, the films form a bilayer which breaks due to the Marangoni instabilities. In the off-specular scattering profiles, $t_{\triangle \mathrm{Gmin}}$ corresponds to what was reported as the breaking up of the transient bilayer [9, 11, 42]. As the concentration of the polymer solution was reduced, phase separation became less pronounced. This was also reported by Dunbar *et al.* [6]. In their study a bilayer structure was obtained at the lowest the concentration studied. The different morphologies were believed to be due to the Marangoni instabilities. The films coated from 86% and 88% toluene show clear scattering peaks which correspond to length scales of 71 μm and 52 μm. Although there was no scattering peak on the film coated from

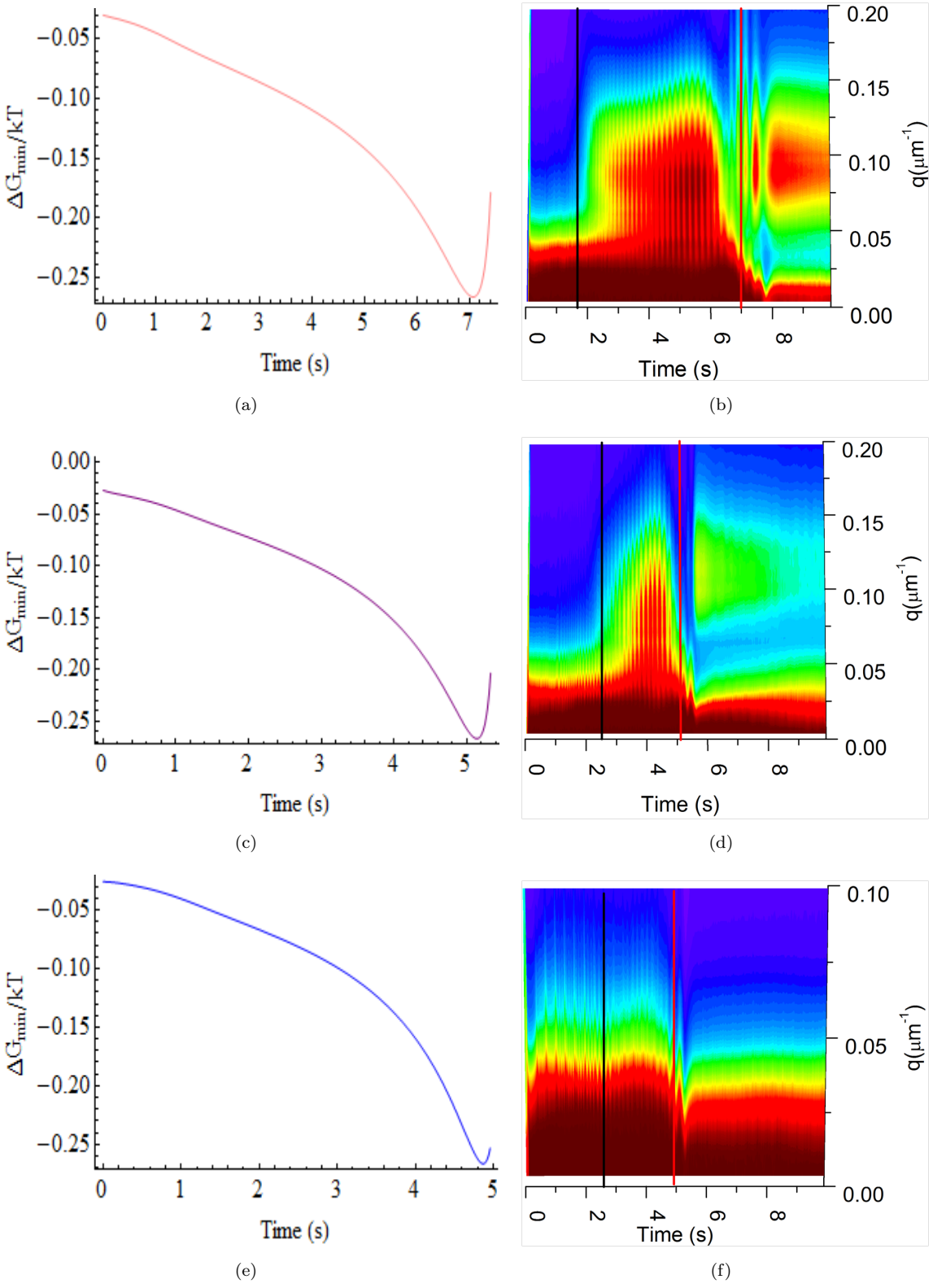

FIGURE 5.3: (a) Free energy of mixing as a function of time for a solution of 7% PMMA, 7% PS and 86% toluene coated at 2000 rpm; (b) shows the corresponding off-specular scattering. (c) Free energy of mixing versus time for a solution of 6% PMMA, 6% PS and 88% toluene coated at 2000 rpm; (d) shows the corresponding off-specular scattering. (e) Free energy of mixing versus time for a solution of 5% PMMA, 5% PS and 90% toluene coated at 2000 rpm; (b) shows the corresponding off-specular scattering.

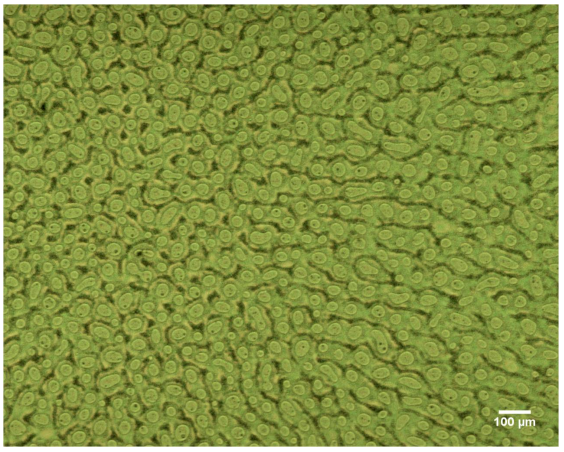

(a)

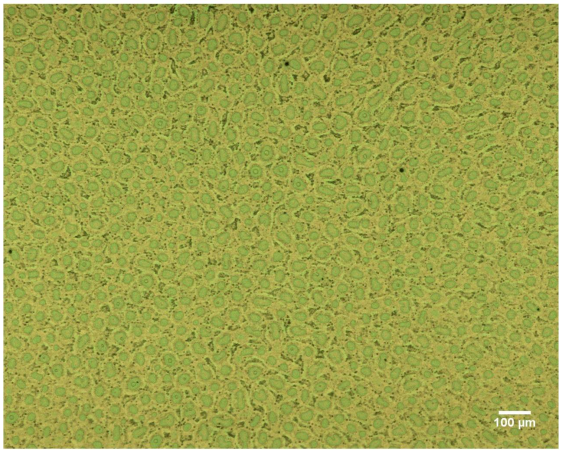

(b)

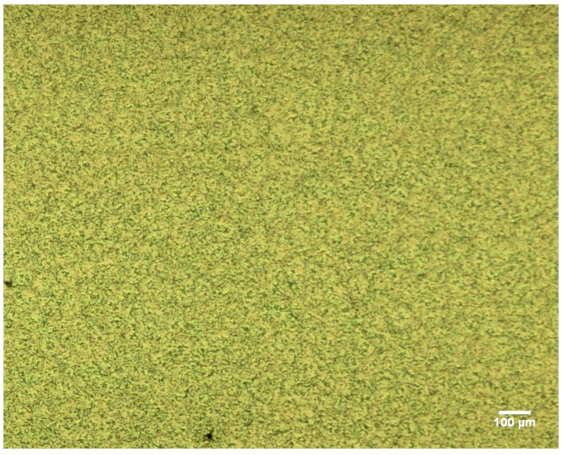

(c)

FIGURE 5.4: (a) microscopic image of a film obtained by coating a solution made of 7% PMMA, 7% PS and 86% toluene at 2000 rpm. b) microscopic image of a film obtained by coating a solution made of 6% PMMA, 6% PS and 88% toluene at 2000 rpm. c) microscopic image of a film obtained by coating a solution made of 5% PMMA, 5% PS and 90% toluene at 2000 rpm.

90% toluene, the Fast Fourier Transform (FFT) of the optical image revealed a length scale of 50 μm.

t_{on} is defined as the time at which the instabilities in the scattering profile start and is marked by the black lines in the Figure 5.3 (b), (b) and (f). $t_{\triangle \mathrm{Gmin}}$ and t_{on} are plotted as a function of the toluene volume fraction (see Figure 5.5 (a)). t_{on} reduces with increasing solution concentration whereas $t_{\triangle \mathrm{Gmin}}$ increases with the solution concentration. Figure 5.5 (b) shows $\phi_{\triangle \mathrm{Gmin}}$ and ϕ_{on}, the volume fraction of toluene at $t_{\triangle \mathrm{Gmin}}$ and t_{on}. Despite the change in t_{on} , ϕ_{on}= 85±2% at all the concentrations and corresponds to the cloud point of the bulk polymer solution at 21°C. Similar results were also reported by Jukes *et al.* [9] when studying the phase separation of films made of F8BT and PFB. t_{on} cannot be the time where phase separation occurs as the free energy plot does not have a minimum. Regardless of the changes in $t_{\triangle \mathrm{Gmin}}$, $\phi_{\triangle Gmin}$= 33% in all the films studied. Figure 5.5 (a) and (b) suggests that a change in solvent volume fraction changes the kinetics of the phase separation, whereas the thermodynamics is not affected. This is confirmed by Figure 5.5 (e) and (f), which shows the free energy as a function of the toluene volume fraction for films coated from solutions with toluene contents equal to 90%, 88% and 86% and spun at 2000 rpm and 1000 rpm. In both graphs the curves overlay and the minimum is reached at toluene volume fractions of 33% and 30.8%. The quench depth increases with the spin speed and is the reason why $\phi_{\triangle Gmin}$ decreases with the spin speed. The instabilities in the film start when the toluene volume fraction is equal to 85%. Figure 5.5 (d) shows that the maximum velocity reached increases with the polymer volume fraction i.e. the radial outflow increases with the polymer concentration. This and the fact that the most concentrated solution is closer to the cloud point explains why the instabilities start earlier in the most concentrated solution. On the other hand the minimum in the free energy is reached in the phase where the solvent evaporation dominates the thinning rate. $t_{\triangle Gmin}$ is delayed when the polymer volume fraction increases because the evaporation rate decreases with increasing polymer concentration, therefore requiring more time to reach $\phi_{\triangle Gmin}$. The lower evaporation rates obtained when the polymer concentration increases is due to the slower diffusion rate.

We shall now discuss the physical meaning of t_{on} and $t_{\triangle Gmin}$, and attempt to understand what is happening in the films at these times. Coveney and Clarke [79] studied the phase separation in a polymer film which contained no solvent. The simulation showed that

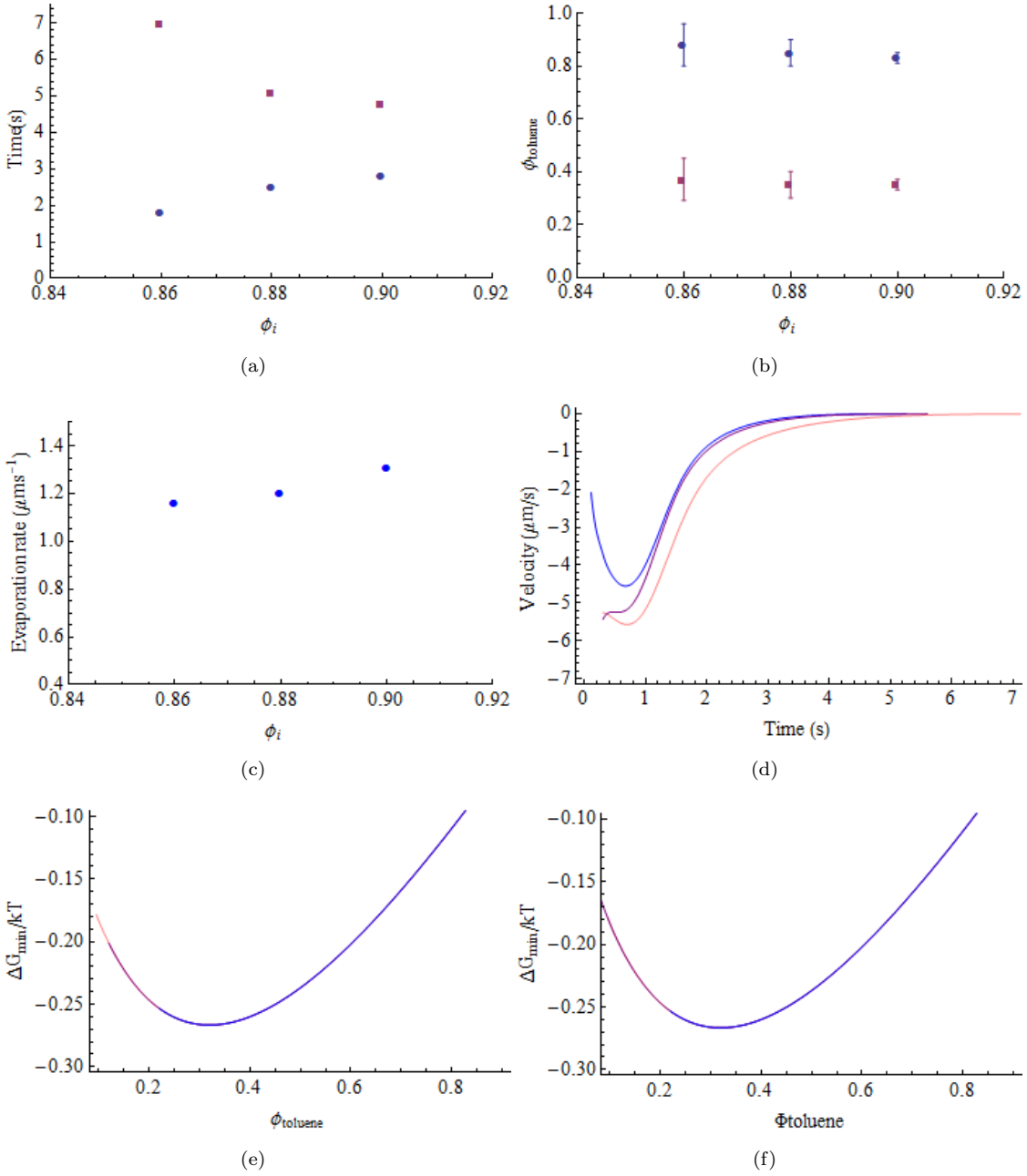

FIGURE 5.5: (a) $t_{\triangle \mathrm{Gmin}}$ (purple) and t_{on} (blue) as a function of the initial toluene volume fraction in the solution ϕ_{i}. (b) $\phi_{\triangle \mathrm{Gmin}}$ (purple) and ϕ_{on} (blue) as a function of the initial toluene volume fraction in the solution. (c) evaporation rate versus the initial toluene volume fraction in the solution. (d) velocity as a function of time for film coated from solutions with equal amounts of PS and PMMA, and 86% toluene (pink), 88% toluene (purple) and 90% toluene (blue). In a), b), c), and d) the films are coated at 2000 rpm. (e) free energy of mixing calculated with the Flory-Huggins equation as a function of the toluene content in the film for films coated from solutions with equal amounts of PS and PMMA, and 86% toluene (pink), 88% toluene (purple) and 90% toluene (blue) at 2000 rpm. (f) free energy of mixing calculated with the Flory-Huggins equation as a function of the toluene content in the film, for film coated from solutions with equal amounts of PS and PMMA, and 86% toluene (pink), 88% toluene (purple) and 90% toluene (blue) at 1000 rpm

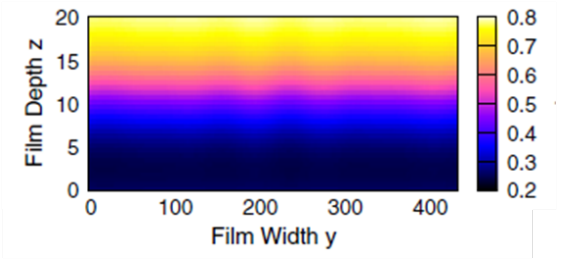

(a)

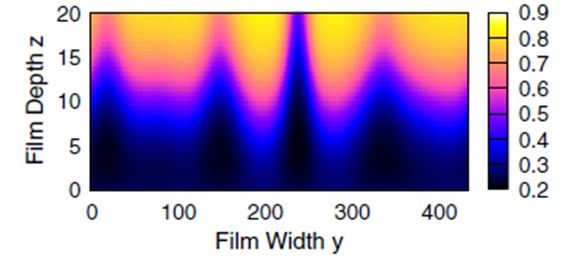

(b)

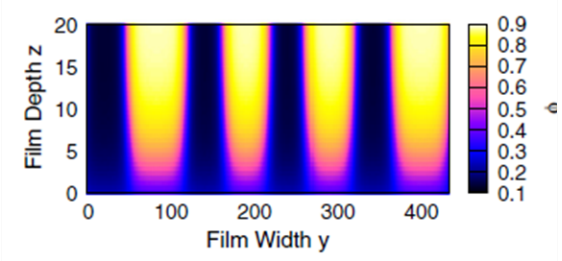

(c)

FIGURE 5.6: Depth profile of film made of two polymers with χ=0.026 and no solvent. (a) shows a bilayer structure with the polymer A at the top of the film, polymer B segregated at the bottom and a flat interface in the middle. (b) the interface starts to distort leading to composition fluctuation at the top and bottom of the film. (c) the film is completely laterally phase sperated. Reprinted with the permission from S. Coveney and N. Clarke *Phys. Rev. Lett* **111** 125702 (2013). Copyright (2013) by the American Physical Society.

at first a bilayer structure is formed with an A rich phase at the top and a B rich phase at the bottom. The interface of these two layers is flat see Figure 5.6 (a). As the interface of the bilayer starts to distort, the top layer of the film is no longer only made of polymer A, the composition of the top layer has two values and the film is laterally phase separated (see Figure 5.6 (b) at film width 20, 200, 250, 350). Coveney and Clarke explained that the concentration fluctuations further enhance the breaking up of the layer and the initial composition fluctuation on the top surface determines where the film will laterally phase separate. In Figure 5.6 (c) the bilayer is broken and the film is laterally phase separated with a dominant length scale

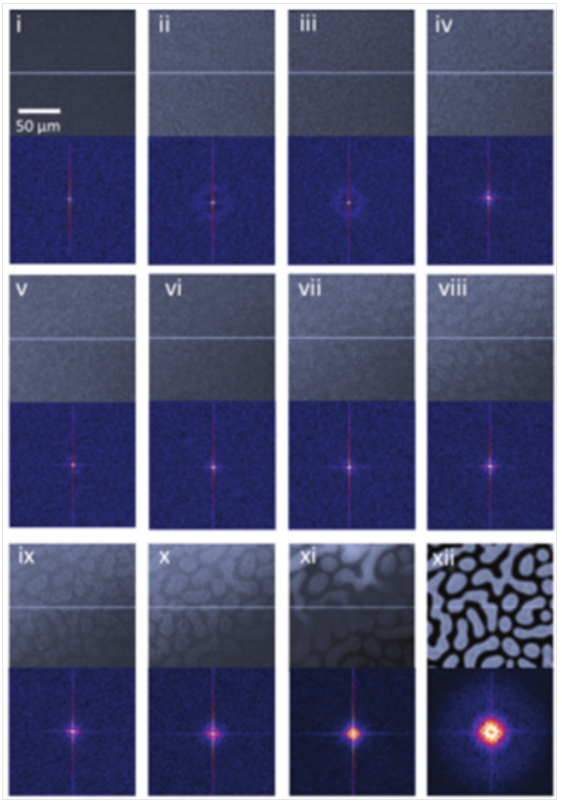

(a)

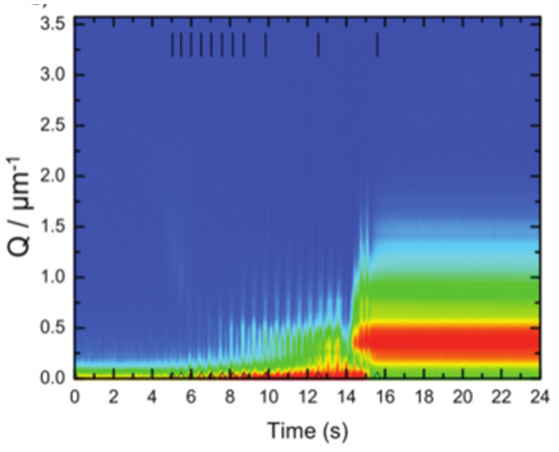

(b)

FIGURE 5.7: Snapshots of the top layer of a thinning films during the spin coating of PS:PMMA film coated from o-xylene. (I-XII) correspond to 0.0, 5.04, 5,48, 6.00, 6.52, 7.04, 7.60 8.16 8.72 9.84 12.56 and 15.60 s. (b) corresponding off-specular scattering profile. Reprinted from D. T. W. Toolan ,E. Haq, A. Dunbar, S. Ebbens ,N. Clarke, P. D. Topham and J. R. Howse, *J. Poly. Sci. Part B: Poly. Phys.* **51** 561 (2013), with permission from John Wiley and Sons

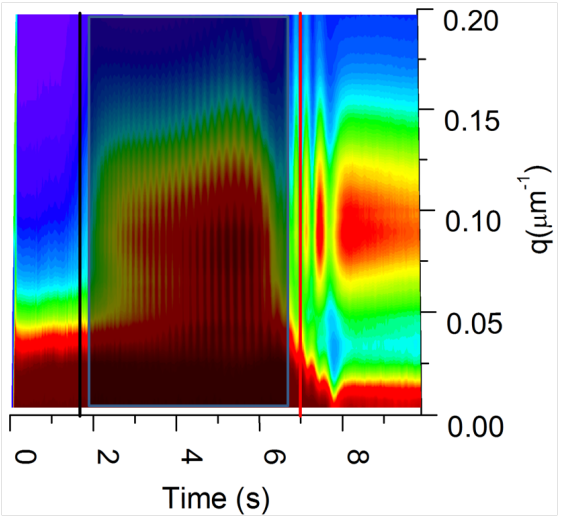

(a)

FIGURE 5.8: Typical off-specular profile of a phase separated film. The shaded period is the time over which the bilayer structure breaks. The black and red line are named the onset of the breaking up of the bilayer and the end of the breaking of the bilayer

Toolan *et al.* [80] used a technique that enables direct observation of the top layer of a spin coated film to investigate the thinning of PS and PMMA film coated from o-xylene. Figure 5.7 (a) shows snapshots of the top layer during the coating and Figure 5.7 (b) shows the off-specular scattering as a function of time. Note that in the off-specular data, t_{on} is observed and the feature that corresponds to the minimum on the free energy in our experiment is also observed. The onset of the concentration fluctuations corresponds to the onset of the instabilities in the off-specular data. Combining Coveney and Clarke's work [79] with Toolan *et al.* work [80], we conclude that at t_{on} concentration fluctuations appears on the top layer and prior to t_{on} the interface of the bilayer starts to distort. t_{on} is the onset of the breaking up of the bilayer. Note that previously the feature observed at $t_{\triangle Gmin}$ was thought to be the time at which the bilayer breaks; we need to re-define this feature. Figure 5.8 shows a typical off-specular profile. We propose to define the period shaded in black as the period when the bilayer breaks up. The black line and the red line correspond to the onset and the end of the breaking up of the bilayer.

In conclusion, changing the concentration of the spin coated solution while keeping the temperature and the spin speed constant changes the kinetics of phase separation. The thermodynamics however remain unchanged. Regardless of the initial solvent fraction, phase separation takes place at the same solvent volume fraction. The cloud point of a bulk solution of PS, PMMA and toluene corresponds to the volume fraction at which

the instabilities in the film starts due to the distortion of the bilayer interface. At the end of the instabilities the free energy reaches its minimum; the experiment performed here does not allow us to understand what is happening in the film when this minimum is reached and future work should attempt to answer to this question. As the spin speed is lowered the quench depth is shallower and the minimum in the free energy is reached at a higher solvent content.

Chapter 6

Dependence of the morphology of PS and PMMA film on χ

In this chapter we will be investigating the effect of the interaction parameter on the morphology of spin coated films. We will also study the effect of the solvent volume fraction on the spin coated film. The change in the interaction parameter will be induced by controlling the coating temperature and the temperature of the solution before coating. In section 6.1 we measure the cloud points of mixtures of PS and PMMA dissolved in toluene, then we discuss the temperature dependency of the interaction parameters $\chi_{\text{ps/pmma}}$, $\chi_{\text{ps/to}}$ and $\chi_{\text{pmma/to}}$. In section 6.2 we present the experimental results and discuss the morphology of the film in terms of the time and volume fraction at the beginning and the end of the instabilities. We will also discuss which phenomenon is at the origin of the different morphologies.

6.1 Cloud point of solutions of PS, PMMA and toluene

UV-visible spectroscopy is used to determine the cloud point of mixtures of PS, PMMA and toluene. The absorbance was measured as the temperature of the solutions was lowered. The solutions studied had toluene concentrations of 88%, 86% and 90%. The cloud point is the point of inflection on the curve describing the absorbance as a function of the temperature. Table 6.1 reports the cloud points of the solutions.

ϕ_t (%)	Cloud point (°C)
90	2
88	3
86	5

TABLE 6.1: Cloud point of ternary solutions with equal amounts of PS, PMMA as a function of the toluene volume fraction

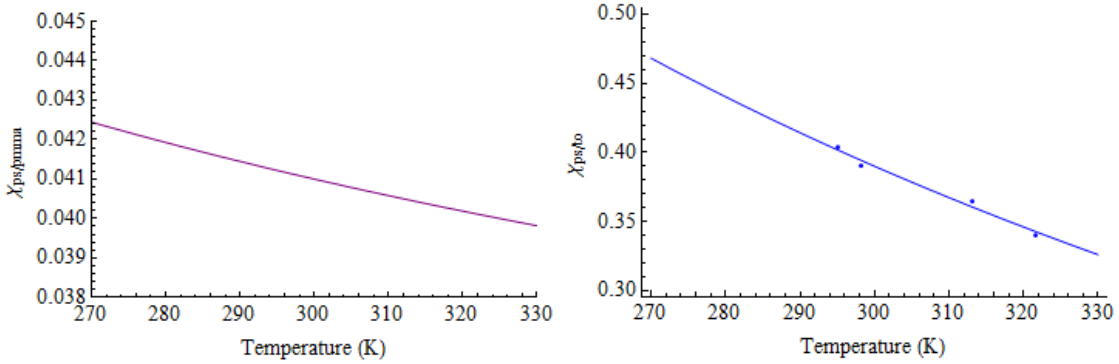

(a) (b)

FIGURE 6.1: (a) Illustrates the temperature denpendence $\chi_{\mathrm{ps/pmma}}$. (b)The temperature dependence of $\chi_{\mathrm{ps/to}}$, the dots are the average of χ reported by Shuld and Wolf, the line is the fit of the data.

The cloud point decreases with decreasing concentration i.e. the higher the concentration of the solution the higher will be the temperature at which its phase separates. We assume that the interaction parameters in the ternary system PS, PMMA and toluene only depend on the temperature. Russell *et al.* [78] proposed the following equation to describe the temperature dependence on $\chi_{\mathrm{ps/pmms}}$

$$0.028 + \frac{3.9}{T}, \tag{6.1}$$

where T is the temperature in Kelvin [78]. Figure 6.1 (a), shows a plot of $\chi_{\mathrm{ps/pmma}}$. Schuld and Wolf reviewed the interaction parameters of polymer and solvent mixtures [81]. The abundant experimental data on the PS and toluene mixture was used to estimate the temperature dependence of $\chi_{\mathrm{ps/to}}$; the experimental data are fitted with an equation in the form of $A + \frac{B}{T}$ in which A and B are fitting parameters and T is the temperature.

The results are shown in Figure 6.1 (b) in which the dots are experimental results and the line is the fit to the data. The measured values of $\chi_{\mathrm{ps/to}}$ decrease with increasing temperature. This is in concordance with the inverse proportionality dependence of the

interaction parameter on the temperature. A low interaction parameter implies that the contact between the two components is more favourable. The values of $\chi_{\text{pmma/to}}$ reported in the literature are limited and they are in poor agreement with each other. At 21°C, $\chi_{\text{ps/pmma}}$ is equal to 0.041 [18, 21], this is significantly lower than $\chi_{\text{ps/to}}$ and $\chi_{\text{pmma/to}}$. This implies that in a bulk solution the contact between PS and toluene, and PMMA and toluene are more energetically favourable compared to the contact between PS and PMMA.

6.2 Morphology of spin coated film

We will investigate the effect of the interaction parameters on the morphology of spin coated films by comparing the thickness of the films, the evaporation rates, the time and the solvent volume fraction at the beginning and at the end of the instabilities. A quantitative study of the thermodynamics of the films (like we performed in chapter 5) is not possible as the temperature dependence of $\chi_{\text{pmma/to}}$ is unknown. The coating temperature is controlled by using the environmental cell described in subsection 3.2.2. This cell is relatively small and there is a build up of solvent vapour above the film which lowers the evaporation rate and influences the morphology of the film. However this error is systematic throughout the whole experiment. The temperature of the solutions prior to coating was controlled using a water bath.

Figures 6.2 (a), (b), and (c) show the thickness profiles of the films coated from solutions with 86%, 88% and 90% toluene at coating temperatures of 21°C to 15°C, to 7°C and 0°C. The time necessary for the film to dry decreases with the temperature and the solvent concentration. The change in temperature does not affect the stage governed by the hydrodynamic forces, whereas the phase controlled by the solvent removal lasts longer when the temperature decreases. Figures 6.3 (a) and (b), (c) and (d), and (e) and (f) show the off-specular profile and the microscopic images of the film coated from the polymer solution with 86% toluene at 21°C, 15°C and 7°C respectively. The off-specular data are characterised by three phases. At first a smooth layering is observed. The second phase is delimited by the beginning and the end of the instabilities. At the onset of the instabilities the film has several length scales; a dominant length scale subsequently appears. The third phase starts from the time when the dominant length scale appears until the films dries. The off-specular data reveals length scales of 70 μm,

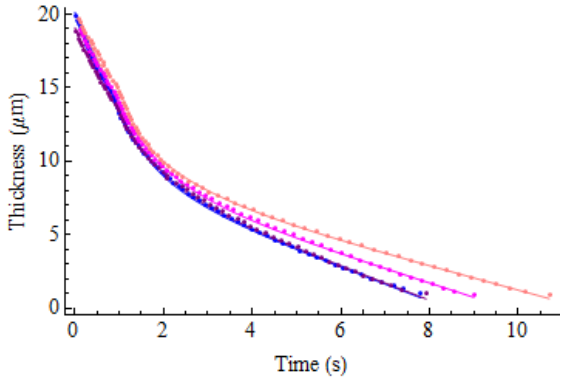

(a)

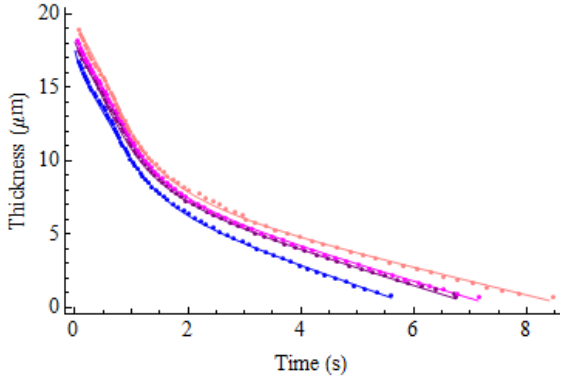

(b)

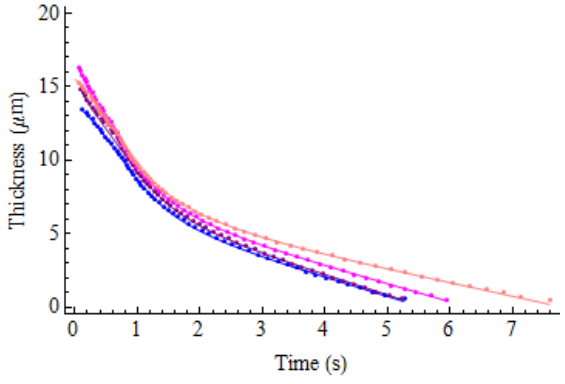

(c)

FIGURE 6.2: (a), (b), and (c) show the thickness profiles for films coated at 2000 rpm polymer blends solution with an equal amout of PS and PMMA and 86%, 88% and 90% toluene, respectively. In (a), (b), and (c) the blue, purple, magenta and pink lines correspond to the coating temparature of 21°C, 15°C, 7°C and 0°C.

57 μm and 50 μm for the films coated at 21°C, 15°C and 7°C respectively. These length scales are in agreement with those calculated from the FFT of the microscopic images which are equal to 69 μm, 57 μm and 52 μm for films coated at 21°C, 15°C and 7°C. At 0°C the solution with 86% toluene has entered the two phase region. The off-specular profile and the microscopic images show that phase separation is not as pronounced at this temperature (see figures 6.3 (g) and (h)). However looking closely at Figure 6.3 (g), one can still distinguish three phases in the off-specular data and length scale of 50 μm. This is in agreement with the length scale of 52 μm measured from the FFT of the microscopic image.

Figures 6.4 (a) and (b) show the off-specular profile and microscopic image of the film coated from a solution containing 88% toluene at 21°C. The dried film shows a length scale of 45 μm. This is in accordance with the length scale of 50 μm calculated from the light scattering data. Figures 6.4 (c), (e) and (g) show the off- scattering profiles for the film coated at 15°C, 7°C and 0°C. Figures 6.4 (d), (f) and (g) are the corresponding microscopic images. Only the solution at 0°C is in the two phase region and yet the off-specular profile of films coated at 15°C, 7°C and 0°C are very similar. They are characterised by a smooth layering following the onset of a weak instability which then disappears to leave a smooth surface. Note that the scattered light in the off-specular data decreases with the temperature. Figure 6.5 (a) and (c) show the off-specular data for the films coated from the solution with 90% solvent at temperature of 21°C and 15°C. Figures 6.5 (b) and (d) are the corresponding microscopic images. There is no dominant length scale and the instabilities in the off-specular data although weak are clearly visible. Figures 6.5 (e) and (g) are the off-scattering profile for the film coated from the 90% solvent solution at 7°C and 0°C. Here again there is no dominant length scale and the onset of the instability cannot be defined. The microscopic images suggest that one polymer is segregated on the top layer of the film. At 0°C all the bulk solutions have entered the two phase region but there seem to be little or no correlation between the phase region of the solutions and the morphology of the films. What therefore are the phenomena that lead to the morphology changes? We will discuss this after first considering the morphologies obtained with respect to the onset and the end of the instabilities which are noted as t_{on} and t_{end}. Studying the thinning rates of the films we calculate ϕ_{on} and ϕ_{end} which are the toluene volume fractions at t_{on} and t_{end}. Figure 6.6 (a) shows t_{on} as a function of the temperature. t_{on} is not reported for the film coated

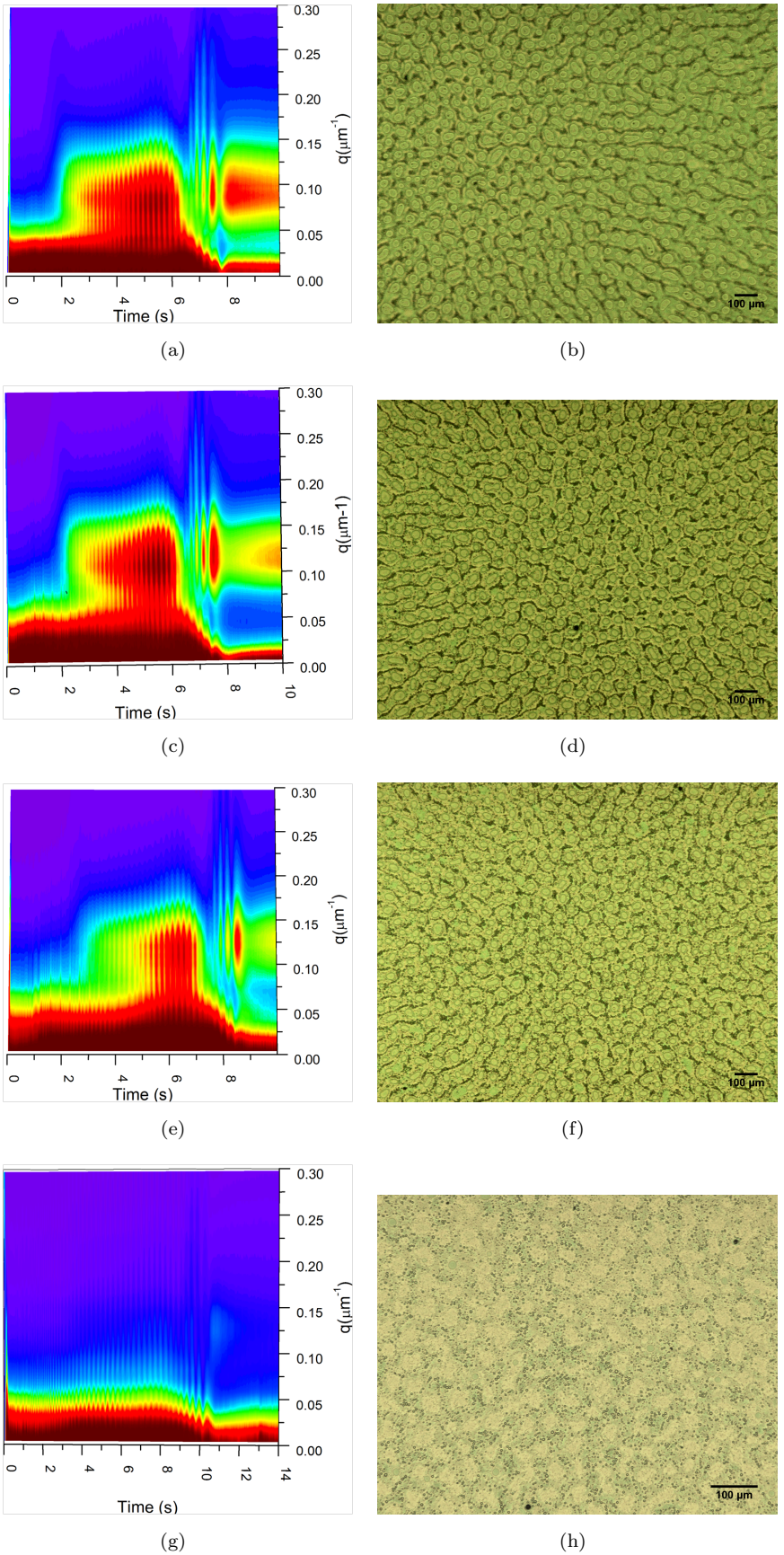

FIGURE 6.3: (a), (c) ,(e) and (f) show the off-specular profile for films coated from a polymer solution with 7% PS, 7% PMMA and 86% toluene at temperatures of 21°C, 15°C, 7°C and 0°C, (b), (d), (f) and (h) are the corresponding microscopic images taken at the centre

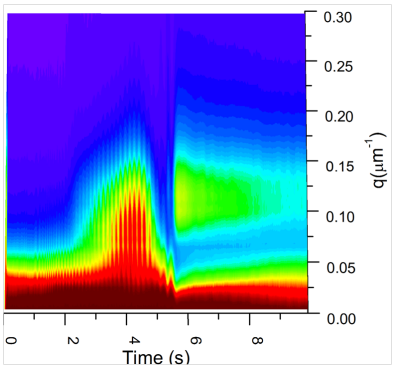

(a)

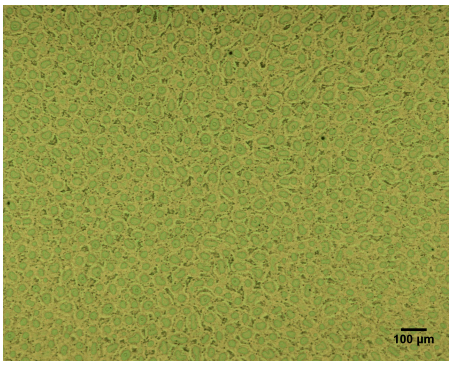

(b)

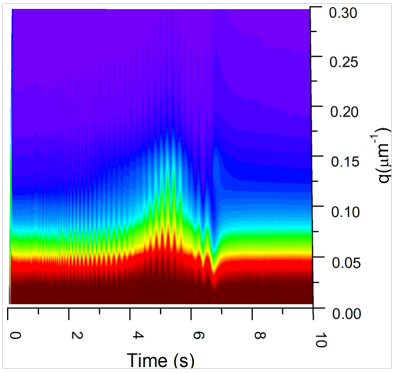

(c)

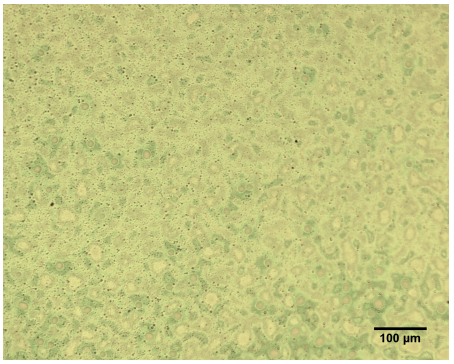

(d)

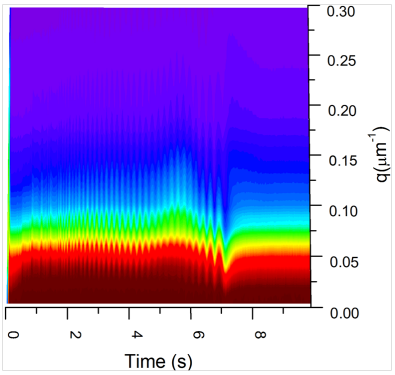

(e)

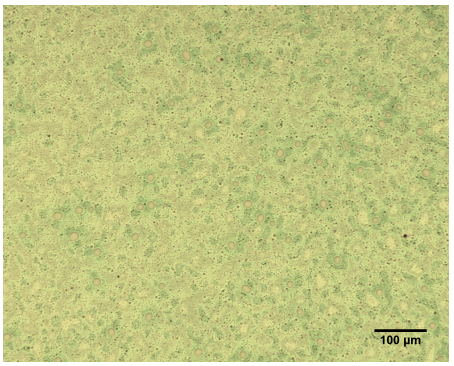

(f)

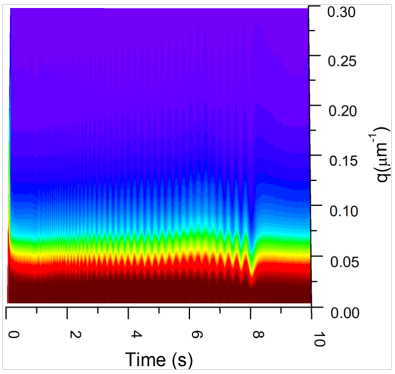

(g)

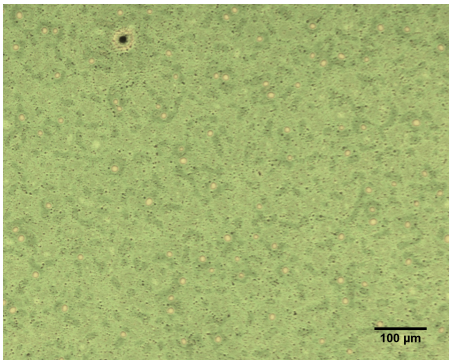

(h)

FIGURE 6.4: (a), (c), (e) and (f) show the off-specular profile for films coated from a polymer solution with 6% PS, 6% PMMA and 88% toluene at temperatures of 21°C, 15°C, 7°C and 0°C, (b), (d), (f) and (h) are the corresponding microscopic images

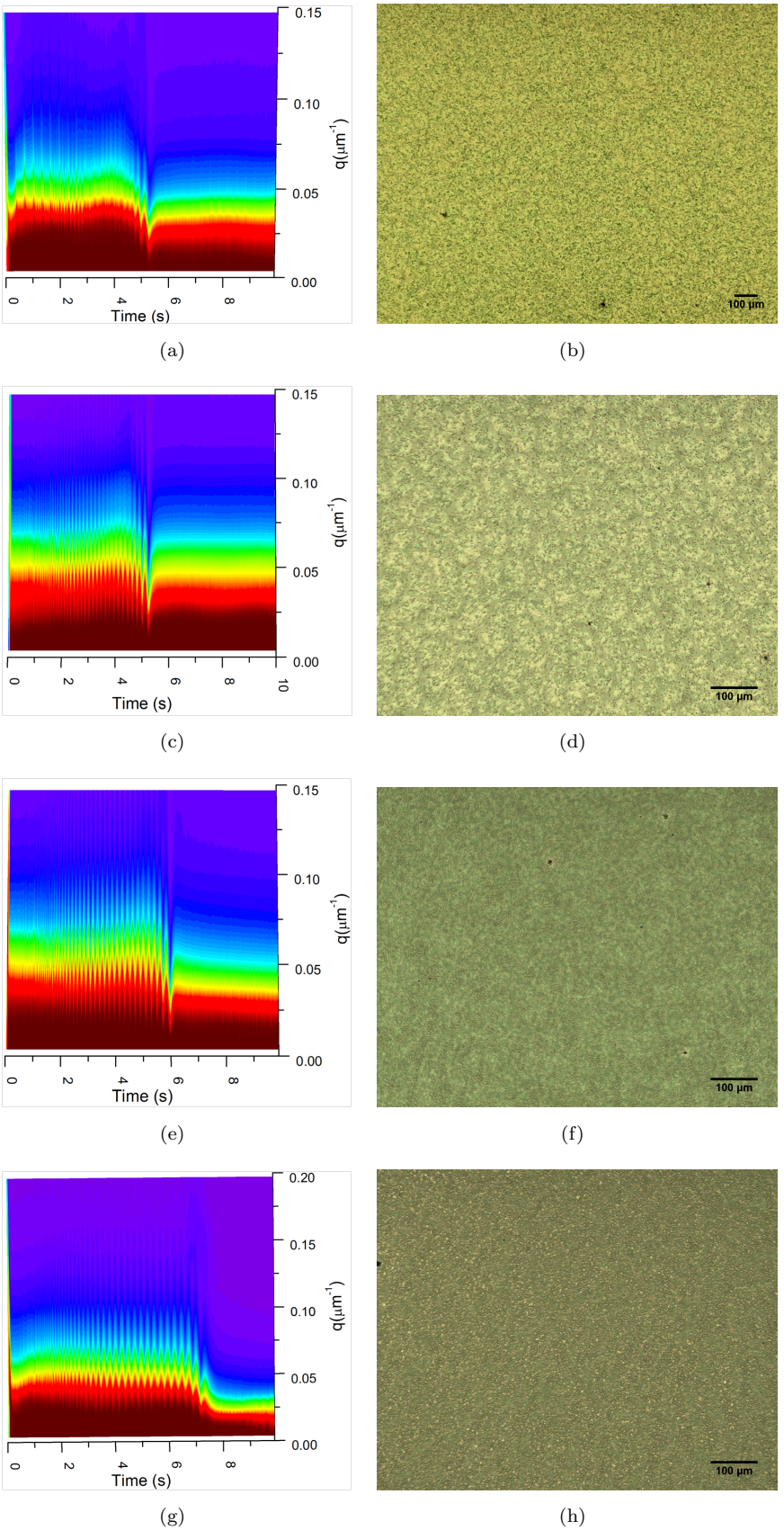

FIGURE 6.5: (a) ,(c), (e) and (f) show the off-specular profile for films coated from a polymer solution with 5% PS, 5% PMMA and 90% toluene at temperatures of 21°C, 15°C, 7°C and 0°C, (b), (d), (f) and (h) are the corresponding microscopic images

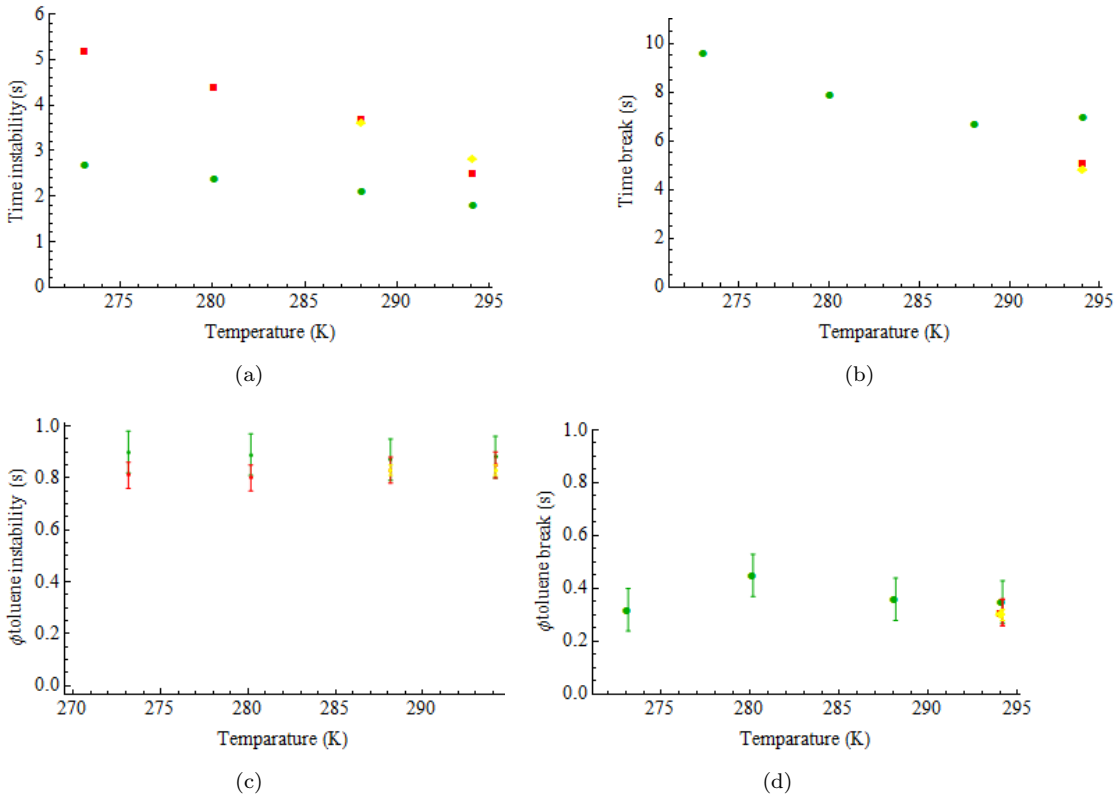

FIGURE 6.6: (a) shows the time at which the instabilities in the film start as a function of the temperature. (b) is a plot of the time at which a dominant length scale appears as function of the coating temperature. (c) shows the solvent volume fraction at which the instabilities in the film starts and (d) shows the toluene volume fraction at which the final phase separtion length scale in the film appears In each of these figure, the colors green, red and yellow correspond to the film coated from the polymer solutions with equal amount of PS and PMMA, and 86%, 88% and 90% toluene.

from 90% solvent at 7°C and 0°C, as they not clearly visible. t_{on} is delayed when the coating temperature decreases and when the concentration of the polymer solution is reduced. ϕ_{on} is plotted as a function of the temperature in agreement with results in chapter 5. At 21°C and 15°C the volume fraction at the onset of the instability is independent of the solution concentration and the coating temperature. For the films coated at 7°C and 0°C, the error bars on ϕ_{on} overlap and we cannot confidently say that ϕ_{on} is independent of the temperature. Figure 6.6 (b) show t_{end} as a function of the coating temperature. t_{end} is observable on the off-specular data only when the film is laterally phase separated. For that reason t_{end} is not reported for all the temperatures and concentration studied. t_{end} increases as the temperature decreases. Similar to what we reported in chapter 5 t_{end} is reached sooner as the polymer concentration decreases. Figure 6.6 (d) shows ϕ_{end} as a function of the temperature. This graph suggests that ϕ_{end} is independent of the temperature. Note that ϕ_{end} has an average value of 35%

toluene which is in agreement with the value of 33% reported in chapter 5.

In section 2.2 we discussed phase separation near a surface. Other than the interactions between the two polymers, phase separation at the vicinity of a surface is also controlled by the interaction between the polymers and the surface and the geometrical constraints on the chain conformation due to the presence of boundaries. The thinner the film the stronger the influence of the substrate. In the presence of a surface the free energy is lowered by having the polymer with the lowest surface energy segregated at the surface. However, there is a cost in having a layer of the film with a composition that differs from that of the bulk. Kraush studied the dependence of the composition profile on the thickness of (PEP) and (dPEP) [10]. As the film thickness decreases the morphology of the film changes from a phase separated structure in the bulk with segregation of the two polymers at the interfaces to a bilayer structure. Using depth profiling methods they observed interferences of two spinodal waves from the two interfaces. Once the film thickness is smaller than the spinodal wavelength which is approximatively equal to 100 nm the coarsening of the phase separated structure is reduced and a bilayer structure will form. This raises the question whether surface directed spinodal decomposition is at the origin of the different morphologies obtained in our experiment? The answer to this question lies in the comparison of the film thickness to the spinodal wave length. Figure 6.7 (a) shows that the thickness of the film decreases with the temperature and the volume fraction of the polymer. The thickness of the films ranges from 600 nm to 1200 nm. The films for which the bilayer like structure is observed are thick enough to sustain a phase separated structure. The different morphologies observed cannot solely be due to the effect of the surface.

In section 2.2 we also saw that at equilibrium a polymer blend at a temperature above T_w will have a wetting layer. In agreement, with this Souche *et al.* reported that when films are coated at a temperature below T_w the films are phase separated [46]. However, as we approach the wetting temperature a bilayer structure forms then breaks because the bilayer structure is metastable compared to the lateral phase separated structure. For $T > T_w$ the bilayer structure is stable. One should consider the possibility that the bilayer structure is favoured because we are approaching the T_w and χ_w. As the temperature is lowered the interaction parameter increases but we do not know the value of χ_w, therefore we can not confirm or disprove this hypothesis.

It was shown that laterally phase separated spin coated films of PS and PMMA transit via a bilayer structure which breaks due to Marangoni instabilities driven by the surface tension gradient. For all the solutions studied, at 21°C, 15°C and 7°C the solutions are in a single phase. The morphology of the films change from laterally phase separated structures when coated from concentrated solutions to bilayer structures when the films are coated from diluted solutions. The Marangoni instabilities are quantified by the Marangoni number

$$\mathrm{Ma} = \frac{\left(\frac{\partial\sigma}{\partial C}\right) h^2 \nabla C}{\mu D}. \tag{6.2}$$

where $\frac{\partial\sigma}{\partial C}$ is the change in the surface tension due to the concentration gradient, h is the thickness of the film, D and ∇C are the diffusion rate and the concentration gradient of the component driving the changes in the surface tension. In spin coating the solvent is the component which drives the concentration gradient. At a given concentration the films are thinner when the temperature is reduced (see Figure 6.7 (a)). We will discuss qualitatively Ma as a function of the film thickness and the temperature. Ma is proportional to the square of the thickness of the film; the thicker the film the stronger the Marangoni instabilities. This suggests that Ma decreases when the temperature is lowered. Ma is inversely proportional to the viscosity; the higher the concentration of the polymer solution the lower the Marangoni number. Figure 6.7 (b) which shows the rate of evaporation as function of the concentration and the temperature is used to discuss how the viscosity changes as the temperature is lowered. The evaporation rate decreases when the polymer concentration increases and when the temperature decreases. During the experiment the films are enclosed in a chamber. At a given temperature the changes in the solvent evaporation rate depend on the solvent mass fraction at the top of the film, which depends on the diffusion rate of the solvent. This implies that at a given temperature the diffusion rate decreases when the thickness of the film increases. We cannot predict how the diffusion rate changes with the temperature. Similarly we cannot predict how $\frac{\partial\sigma}{\partial C}$ changes as a function of the polymer concentration and the temperature. However, in the early stage of the process the surface tension of the film is essentially equal to the surface tension of toluene. According to the Eötvös's rule the surface tension increases when the temperature decreases [82]. As the film solidifies, the surface tension increases. However, it is complicated to predict the gradient in the surface tension as the solvent evaporates. The surface tension gradient depends on the difference in the surface energy of the two polymers, the structure of the film and the temperature. If one

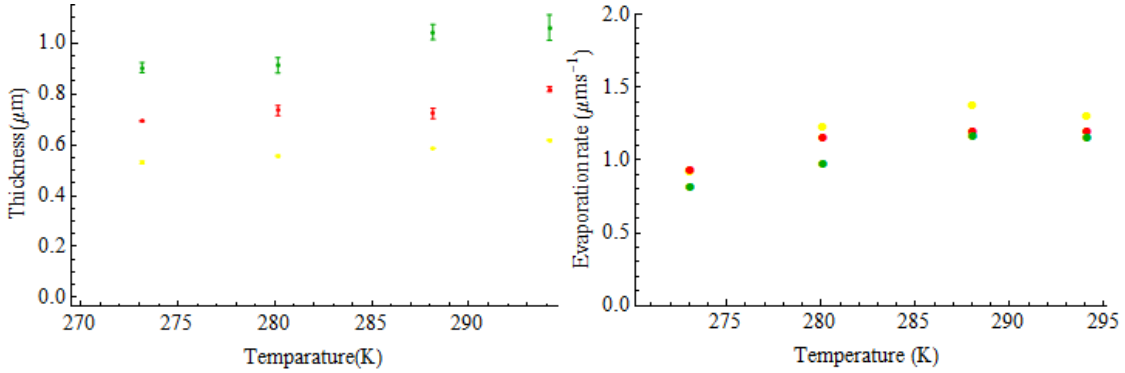

(a) (b)

FIGURE 6.7: (a) dry thickness versus the temperature (b) Evaporation rates as a function of the temperature. The green, red and yellow correspond to the evaporation rate for films coated at 2000 rpm from solutions with eaqual amount of PS and PMMA and 86%, 88% and 90% of toluene

of the polymers is segregated at the surface, the surface gradient will be reduced and if the coating temperature approaches the critical temperature the system will undergo a wetting transition in which case the $\frac{\partial\sigma}{\partial C}$ will decrease further. We cannot predict how the concentration gradient (∇C) changes as a function of the film thickness and the temperature.

The Marangoni effect arises by having a greater rate of evaporation compared to the diffusion rate [11]. Mokarian-Tabari *et al.* show that the Marangoni instabilities are reduced as the rate of evaporation is lowered. We will compare our results with those obtained by Mokarain-Tabari. At a given temperature the evaporation rate is lower in the film coated from 86% toluene and yet the films are all phase separated. This is in disagreement with Mokarian-Tabari *et al.* With Figure 4.14 (a), we showed that at low vapour pressure the evaporation rate is controlled by the solvent diffusion rate and at high vapour pressure the rate of evaporation is controlled by the amount of solvent in the overlaying layer. This suggests that in the experiment performed by Mokarian-Tabari, as the vapour pressure was increased the rate of evaporation was not controlled by the solvent diffusion. Our results show that low evaporation does not always lead to the formation of the bilayer. The contradiction between Mokarian-Tabari *et al.*'s work and ours comes from the different phenomena that caused the lowering of the evaporation rate. In our experiment at a given temperature, the lower evaporation rate in the film coated from the most concentrated solution is a consequence of the slower diffusion of toluene molecules at the surface. In the experiment performed by

Mokarian-Tabari *et al.* the low evaporation rates are due to the fact that evaporation is not controlled by the diffusion but rather by the solvent vapour above. This results in a low solvent gradient and a reduced Ma. A more accurate statement to explain Mokarian-Tabari *et al* results and ours is that the Ma is reduced when the evaporation is not controlled by the diffusion. As we decrease the temperature the evaporation rate is lowered; essentially, our experiment is similar to Mokarian-Tabari's. We put forward that the bilayer structures observed when the temperature is lowered are due to the lowering of Marangoni instabilities. The films coated from the solutions with 88% and 90% at 0°C have bilayer structures, whereas the ones coated at 86% at 0°C are phase separated. The expression of Ma shows that there is a threshold evaporation rate (diffusion rate) and a threshold thickness for which the bilayer appears depending on viscosity.

Phase separation during spin coating differs from bulk phase separation due to the presence of a surface and the presence of shear. We discussed the formation of the bilayer in terms of the surface effect, the interaction parameters and the Marangoni instabilities. Until now we have not discussed the effect of the shear on the phase separation and its role during the formation of the bilayer. In order to answer to this question we first need to discuss phase separation of bulk polymer solutions in the presence of a shear. At a given polymer concentration and in a steady shear a polymer solution of PS dissolved in toluene is more viscous than a solution of PMMA dissolved in toluene; however the viscosity difference is negligible [83]. According to Onuku [84] in the presence of a shear, the phase separation of a ternary solution with negligible viscosity difference between the two polymers leads to an anisotropic phase separation with the less viscous polymer acting as a matrix and spheroidal domains of the more viscous polymer aligned in the direction of the fluid motion. In the presence of shear the phase separation of PS/PMMA/toluene, PMMA will act as the matrix and PS will form spheroidal domains. In spin coated films the shear rate is proportional to the radius and as a consequence it is equal to zero at the centre then linearly increases with the radius. By comparing the morphology of the film at the centre and the edge of the film one can understand the influence of the shear. A remarkable difference between the centre and the edge is the presence of striations. Striations are lines oriented in the direction of the fluid motion. In order to understand the effect of the shear rate on the formation of striations, Haas *et al* studied striation width as a function of the radial

position in a spin coated sample [85]. It was found that the width of the striation was independent of the radial position. This experiment proves that the striations result from more complex phenomena than the simple elongation of the phase separated domains. Haas *et al* propose the following mechanism for the formation of striations: striation forms via a combination of the Marangoni effect and the local fluid flows through the following mechanism. Marangoni cells are formed over the whole film. At the edges of the substrate the local motion of the fluid leads to an elongation of the cells in the direction of the flow. This hypothesis is supported by several studies which show that striations can be suppressed by using a solvent with a high boiling point or by increasing the solvent vapour above the film during the coating [5, 86]. In addition, striations have also been observed in drop coated or dip coated films [87]. Mokarian-Tabari *et al* studied the morphology of the film as a function of the radial position and the vapour pressure [11]. In the absence of solvent vapour, Marangoni cells where observe at the centre of the film and striations at the edges. In the presence of vapour, a bilayer was formed at the centre and the striations where eliminated. The fact that the bilayer is formed at the centre of the film where the shear rate is low shows that the surface effect is the dominant factor in the formation of bilayers. The local fluid motion at the edges disturbs the formation of the bilayer. However during the spin coating of PS and PMMA films, it was shown that PS is segregated at the top and PMMA at the bottom. Rheological studies showed that PMMA in toluene has a lower viscosity than PS [83]. This could explain why the PS is segregated at the top. This is a question that we are unable to answer which requires further investigation. In this study the laser was pointed in the centre of the film. The morphologies obtained here are subject to negligible shear rates. As a result we state that shear does not play any role on the formation of bilayers obtained here.

In summary, we studied how the interaction parameters affect the morphology of PS and PMMA films. The films were coated from solutions in the single phase and from solutions in the two phase region. There is no significant distinction in the morphologies when the solution is in either of the two phase regions. Lateral phase separation is promoted when the temperature and the concentration increases and the morphology of the film approaches a bilayer structure when the temperature and concentration are reduced. Comparing our experiment with another reported elsewhere [11] we suggest that the bilayer structures are obtained because the Marangoni instabilities are reduced.

Chapter 7

Conclusion

We have studied the dynamics and the thermodynamics of spin coated polymer films. During spin coating, polymer films are dynamic systems in which the thickness, the viscosity, the solvent and the polymer volume fraction are time dependent. We wish to gain a deeper understanding of the phase separation in polymer films by taking account of the dynamic aspect of the process. The optospinometer was used to monitor the thickness changes and the off-specular scattering as a function of time.

In chapter 4 we studied the dynamics of spin coating of a liquid layer exposed to solvent vapour. We proposed a semi-imperial model which contains a correction term in the velocity to model the inertial forces. This model was compared to the Meyerhofer and the RBD model. The latter also accounts for the inertial forces. Poor agreement was reported between the Meyerhofer model and the data in the early stage of the coating because this model neglects the inertial forces which are important in the first stage of the coating. The fits obtained with the RBD model improve as the vapour pressure increases. Further analysis revealed that the RBD equation of motion is excellent to describe the spin coating of a solute free layer when the inertial forces are weak. The semi-empirical model is in good agreement with the data regardless of the solvent vapour pressure or spin speed. The viscosity terms in the RBD and the semi-empirical model were modified to account for the changes in the viscosity as the film thins. The RBD model underestimated the magnitude of the inertial forces, resulting in poor agreement with the data in the early stage of the coating. The semi empirical model gave excellent agreement with the thickness profile data; this model opens new perspectives such as

allowing us to retrieve the evaporation rate and plot the velocity and the solvent and polymer volume fractions as a function of time.

In chapter 5, we used the semi-empirical model to study the thermodynamics of films containing an equal amount of PS and PMMA while changing the toluene volume fraction. We aimed to find out whether the cloud point in spin coated films depends on the solution's solvent content. In agreement with the work previously reported when studying the morphology of spin coated films of PS and PMMA, the off-specular scattering revealed that lateral phase separation results from the breaking up of a transient bilayer structure. The off-specular data showed a distinct period during which the bilayer structure is breaking. The time at which the instabilities in the film starts is delayed as the solvent volume fraction increases. However the instabilities enda sooner as the the solvent volume fraction increases. Comparing our results with the literature, we attribute the onset of the instabilities to the start of the distortion of the bilayer interface. Regardless of the initial solvent volume fraction, the solvent volume fraction in the film is equal to 84% at the onset of the breaking up of the bilayer and 33% at the end of the instabilities. We plot the free energy of mixing as a function of time. A minimum in the free energy is observed when the breaking up of the bilayer ends. This experiment revealed that the thermodynamics remains unchanged when the initial solvent volume fraction is changed whereas the kinetics strongly depends on the starting solvent volume fraction.

In chapter 6 we aimed to answer the question of how the interaction parameters affect the morphology of spin coated films. The change in the interaction parameters were induced by controlling the temperature of the solutions and the coating temperature. Solutions with toluene volume fractions of 86% , 88% and 90% and equal amounts of PS and PMMA were coated at 21°C, 15°C, 7°C and 0°C. The morphology of the films changed from laterally phase separated structures to bilayer structures when the temperature is reduced. The lateral phase separation is more pronounced when the polymer concentration of the solution increases. The change in morphology is believed to be due the to Marangoni instabilities, which reduce with the evaporation rate.

We believe that the work done here contributes to a better understanding of the phase separation and dynamics of spin coated film. However there are still many unanswered questions which we will list in chapter 8.

Chapter 8

Future work

Dynamics of spin coated solvent mixtures

Striations in spin coated polymer films are due to non uniform solvent evaporation rate. One method of improving the uniformity of the film is to mix two solvents with different evaporation rates. The solvent with the highest evaporation rate allows for a good coverage of the substrate whereas the second solvent delays the glass transition and lowers the Marangoni instabilities. Figure 8.1 (a) and (b) show the thinning of toluene and o-xylene layers.

The solid lines are the fits obtained with the semi-empirical model and the dashed lines are the fits obtained with the RBD model. The RBD model describes accurately the thinning of an o-xylene layer. O-xylene has a higher kinematic density and the correction term in the RBD model is inversely proportional to ν. This implies that the inertial forces are lower in the o-xylene layer than the toluene layer. Figure 8.1 (c) shows the thinning of a mixture of o-xylene and toluene (50:50 by volume). The semi-empirical model and the RBD model are in good agreement with the data in the first stage of the coating. However, these models are in poor agreement with the data in the phase where the solvent removal dominates the process. The evaporation rate is time dependent. Birni and Haas studied the evaporation of a mixture of solvents [30] and they observed three different stages. In the first stage the thinning is governed by the hydrodynamic forces and two distinct evaporation stages with different evaporation rates are observed. The first one corresponded to the more volatile solvent and the second one that corresponded to the less volatile solvent. It would be interesting to expresses

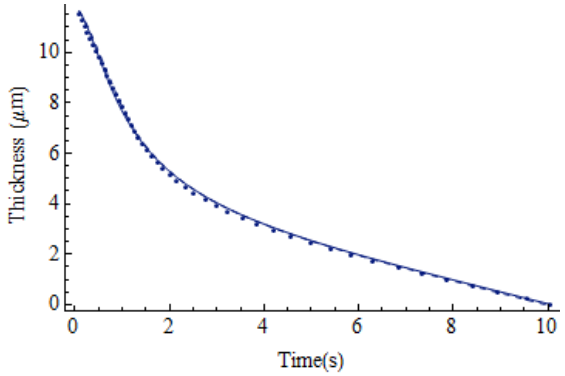

(a)

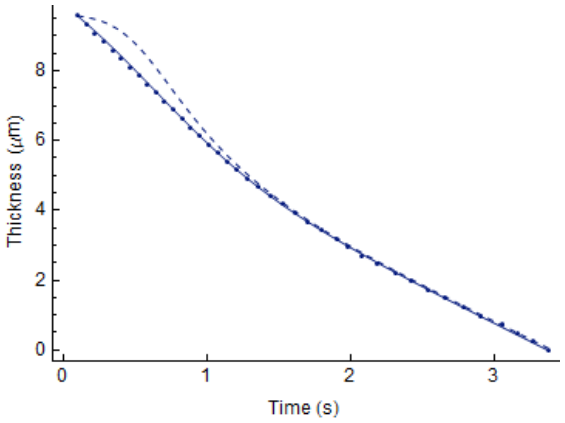

(b)

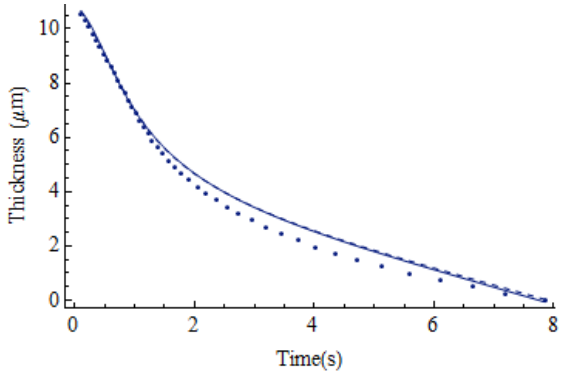

(c)

FIGURE 8.1: Thickness profile of a toluene layer (a), Oxylene (b) and of a mixture of toluene and o-sylene at 50:50 by volume (c)

.

the time dependent evaporation rate as a function of the respective solvent evaporation rates. The ultimate aim of this project would be to use the knowledge acquired when studying the dynamics of spin coating of a solvent mixture to understand the dynamics of spin coating of a ternary solution made of two solvents and one polymer.

Non uniform evaporation rates

Non uniformities in the film thickness are believe to be due to the change in evaporation rate through the surface. However this has not be proven experimentally. One way to verify this statement would be to monitor the radial evaporation rate profile during the coating. The optospinometer needs to be upgraded to enable monitoring of the thickness over a line that passes through the center of the film. The RBD model or the semi empirical model can be used to determine the radial evaporation rate profile. Using the semi-empirical model one would be able to plot the radial axial velocity profile; this is valuable information to understand the non-uniformity in spin coated films.

Quantification of the Marangoni number

Marangoni instabilities are believed to cause the breaking up of the transient bilayer. However to the best of our knowledge the Marangoni number has never been quantified during spin coating. The Marangoni number is expressed as

$$\mathrm{Ma} = \frac{\left(\frac{\partial \sigma}{\partial C}\right) h^2 \nabla C}{\mu D}. \tag{8.1}$$

where $\frac{\partial \sigma}{\partial C}$ is the change in the surface tension due to the concentration gradient, h is the thickness of the film and D is the solvent diffusion rate. Marangoni cells form when the Marangoni number reaches the threshold value of 80. All of the terms in Equation 8.1 are time dependent; the aim of this project would be to estimate the Marangoni number and correlate it with the morphology of the film and also determine whether the threshold value corresponds to a specific time in the off-specular data.

The project should first investigate the thinning rate of a ternary system polymer A/ Polymer B/solvent. The thinning rate of a film is extremely reproducible as long as the spin speed, the temperature, the vapour pressure, the concentration of the solution and the air flow above the film are kept unchanged. The first stage of this project would be

to create a database to determine the time necessary for the film to dry and how the solvent volume fraction in the film changes over time. In order to estimate the changes in the surface tension one could prepare a series of films coated for different times. The surface tension could then be calculated using contact angle measurements. Using the database, the duration of the coating will be associated to a certain value of the solvent volume fraction. The challenge of this experiment would be finding a method to freeze the structure of the film without removing any of the of the solvent. In order to estimate the concentration gradient (∇C) the optospinometer needs to be modified so that the thinning rates could be monitored over the film. The semi-empirical model could be used to estimate the solvent volume fraction at different points on the surface over time and knowing the distance between these points the solvent gradient over the film could be estimated. In this experiment one would neglect the solvent gradient in the vertical axis.

Interaction parameter

In chapters 5 and 6, the chamber used to control the coating temperature was relatively small. As a consequence, solvent build up also contributed to the lowering of the evaporation rate and the changes in the morphology. A better way to study only the effect of the interaction parameter would have been to allow an inert gas to flow above the film. Also Figure 6.1 shows that $\chi_{\mathrm{ps/pmma}}$ does not change much in the range of temperatures that we studied. Perhaps this would explain the reason why the morphology of the films seems to be dominated by the Marangoni instabilities. It would be interesting to repeat this experiment with a polymer blend for which the interaction has a stronger dependence on the temperature.

Phase diagram of spin coated film

In chapter 5 we calculate the solvent volume fraction for which the system phase separates. However all the solutions contain an equal amount of PS and PMMA. By changing the relative volume fraction of the two polymers we could plot the phase diagram of PS and PMMA during spin coating.

Bibliography

[1] A. G. Emslie, F. T. Bonner, and L. G. Peck. *J. Appl. Phys.*, **29**:858–862, 1958.

[2] D. Meyerhofer. *J. Appl. Phys.*, **49**:3993–3997, 1978.

[3] B .Reisfeld, S. G. Bankoff, and S. H. Davis. *J. Appl. Phys.*, **70**:5258–5266, 1991.

[4] B. K. Daniels, Charles R. Szmanda, M.l K. Templeton, and P. Trefonas III. pages 192–201. International Society for Optics and Photonics, 1986.

[5] X. Min, X. Orignac, and R. M. Almeida.

[6] A. D. F. Dunbar, P. Mokarian-Tabari, A. J. Parnell, S. J. Martin, M. W. Skoda, and R. A. L. Jones. *Euro Phys J. E*, **31**:369–75, 2010.

[7] D. E. Bornside, R. A. Brown, P. W. Ackmann, J. R. Frank, A. A. Tryba, and F. T. Geyling. *J. Appl. Phys.*, **73**, 1993.

[8] D. E. Haas, J. N. Quijada, S. J. Picone, and D. P. Birnie III. **3943**:280–284, 2000.

[9] P. C. Jukes, S. Y. Heriot, J. S. Sharp, and R. A. L. Jones. *Macromolecules*, **38**:2030–2032, 2005.

[10] G Krausch. *Mater Sci. & Eng.*, **14**:1–94, 1995.

[11] P. Mokarian-Tabari, M. Geoghegan, J. R. Howse, S. Y. Heriot, R. L. Thompson, and R. A. L. Jones. *Eur. Phys J. E*, **33**:283–289, 2010.

[12] D. P. Birnie and M. Manley. *Phys. Fluids*, **9**:870–875, 1997.

[13] D. P. Birnie. *J. Non-Cryst. Solids*, **218**:174–178, 1997.

[14] J. W. Cahn and J. E. Hilliard. *J. Chem. Phys.*, **28**:258–267, 1958.

[15] T.G Fox. *Bull. Americ. Phys. Soc.*, **1**, 1956.

[16] J. Arnauts and H. Berghmans. *Polymer communications*, **28**:66–68, 1987.

[17] S. Z. D. Cheng. *Phase Transitions in Polymers: The Role of Metastable States: The Role of Metastable States*. Elsevier, 2008.

[18] W. W. Y. Lau, C. M. Burns, and R. Y. M. Huang. *Eur. Poly. J.*, **23**:37–39, 1987.

[19] D. Berek, D. Lath, and V. urovič. *J. Poly. Sci. Part C: Poly. Symp.*, **16**:659–667, 1967.

[20] V. Narasimhan, R. Y. M. Huang, and C. M. Burns. *J. Appl. Poly. Sci.*, **26**:1295–1300, 1981.

[21] W. W. Y. Lau, C. M. Burns, and R. Y. M. Huang. *J. Appl. Poly. Sci.*, **29**:1531–1536, 1984.

[22] H. Bérnard. *Comptes Rendus Hebdomadaire des Sciences des Séances de l'Académie des Sciences*, **130**:1004–1007, 1900.

[23] C. Marangoni. *Annalen der Physik und Chemie*, **219**:337–354, 1871.

[24] L. Rayleigh. *Phil. Mag.*, **32**:529–546, 1916.

[25] M. J. Block. *Nature*, **178**:650–651, 1956.

[26] J. R. A. Pearson. *J. Fluid. Mech.*, **4**:489–500, 2006.

[27] I. G. Currie. *J. Fluid. Mech.*, **29**:337–347, 2006.

[28] A. Vidal and A. Acrivos. *Ind. & Eng. Chem. Fund.*, **7**:53–58, 1968.

[29] D. E. Haas and D. P. Birnie. *J. Mater. Sci.*, **37**:2109–2116, 2002.

[30] D. P. Birnie. *J. Mater. Res.*, **16**:1145–1154, 2011.

[31] S. C. Luo, V. Craciun, and E. P Douglas. *Langmuir*, **21**:2881–2886, 2005.

[32] S. Reich and Y. Cohen. *J. Poly. Sci.*, **19**:1255–1267, 1981.

[33] R. A. L Jones, E. Kramer, M. Rafailovich, J. Sokolov, and S. Schwarz. *Phys. Rev. Lett*, **62**:280–283, 1989.

[34] R. C. Ball and R. L. H. Essery. *J. Phys: Cond. Matter.*, **2**:10303–10320, 1990.

[35] F. Bruder and R. Brenn. *Phys. Rev. Lett.*, **69**:624–627, 1992.

[36] R. A. L. Jones, L. J. Norton, E. J. Kramer, F. S Bates, and P. Wiltzius. *Phys. Rev. Lett.*, **66**:1326, 1991.

[37] S. Puri and K. Binder, 1992.

[38] M. Geoghegan, R.A.L. Jones, R.S. Payne, P. Sakellariou, A.S. Clough, and J. Penfold. *Polymer*, **35**:2019–2027, 1994.

[39] S. Walheim, M. Böltau, J. Mlynek, G. Krausch, and U. Steiner. *Macromolecules*, **30**:4995–5003, 1997.

[40] M. Boltau, S. Walheim, J. Mlynek, G. Krausch, and U. Steiner. **391**:877–879, 1998.

[41] K. Dalnoki-Veress, J.A. Forrest, J.R. Stevens, and J.R. Dutcher. *Physica A.*, **239**:87–94, 1997.

[42] S. Y. Heriot and R. A. L. Jones. *Nature Mater.*, **4**:782–6, 2005.

[43] N Clarke. *Eur. Phys. J. E*, **14**:207–210, 2004.

[44] N. Clarke. *Macromolecules*, **38**:6775–6778, 2005.

[45] M. Souche and N. Clarke. *Eur. Phys. J. E, Soft matter*, **28**:47–55, 2009.

[46] M. Souche and N. Clarke. *Macromolecules*, **43**:5433–5441, 2010.

[47] M. Souche and N. Clarke. *J. Chem. Phys.*, **131**:244903–1–244903–9, 2009.

[48] W. Ostwald. *Kolloid-Zeitschrift*, **47**:176–187, 1929.

[49] A. Acrivos, M. J. Shah, and E. E. Petersen. *AIChE J.*, **6**:312–317, 1960.

[50] S. A. Jenekhe and S. B. Schuldt. *Ind. & Eng. Chem. Fund.*, **23**:432–436, 1984.

[51] P. J. Carreau. *J. Rheo.*, **16**:99–127, 1972.

[52] J. H. Lai. *Poly. Eng. Sci.*, **19**:1117–1121, 1979.

[53] B. D. Washo. *IBM J. Res & Develo*, **21**:190–198, 1977.

[54] W. J. Daughton and F. L. Givens. *J. Electrochem. Soc.*, **129**:173–179, 1982.

[55] B. T. Chen. *Poly. Eng & Sci*, **23**:399–403, 1983.

[56] W. W. Flack, D. S. Soong, A. T. Bell, and D. W. Hess. *J. Appl. Phys.*, **56**:1199–1206, 1984.

[57] S. A. Jenekhe. *Ind. & Eng. Chem. Fund.*, **23**:425–432, 1984.

[58] T. J. Rehg and B. G. Higgins. *Phys. Fluids.*, **31**:1360–1371, 1988.

[59] D. E. Bornside, C. W. Macosko, and L. E. Scriven. *J. Appl. Phys.*, **66**:5185–5193, 1989.

[60] Th. V. Kármán. *J. Appl. Math. & Mech*, **1**:233–252, 1921.

[61] F. Horowitz, E. Yeatman, E. Dawnay, and A. Fardad. *J. Phys III*, **3**:2059–2063, 1993.

[62] D. E. Haas and D. P. Bimie. *Ceramic Transactions*, **123**:133–138, 2001.

[63] D. P. Birnie III. *Mater. Lett.*, **58**:2795–2800, 2004.

[64] D. P. Birnie, D. E. Haas, and C. M. Hernandez. *Opt & Lasers Eng.*, **48**:533–537, 2010.

[65] S. Ebbens, R. Hodgkinson, A. J. Parnell, A. Dunbar, S. J. Martin, P. D. Topham, N. Clarke, and J. R Howse. *ACS nano*, **5**:5124–5131, 2011.

[66] F. Keith, J. H. Taylor, and J.P. Chong. Technical report, DTIC Document, 1958.

[67] B. G. Higgins. *Phys. Fluids*, **29**:3522, 1986.

[68] D. B. Hall, P. Underhill, and J. M. Torkelson. *Poly. Eng. & Sci.*, **38**:2039–2045, 1998.

[69] J. Gu, M. D. Bullwinkel, and G. A. Campbell. *Poly.r Eng. & Sci.*, **36**:1019–1026, 1996.

[70] S. A. Jenekhe. *Poly. Eng. & Sci.*, **23**:830–834, 1983.

[71] I. Noda, Y. Higo, N. Ueno, and T. Fujimoto. *Macromolecules*, **17**:1055–1059, 1984.

[72] R. Koningsveld and L. A. Kleintjens. *Macromolecules*, **4**:637–641, 1971.

[73] P.J. Flory and H. Daoust. *J. Poly. Sci.*, **25**, pages=429–440, year=1957,.

[74] B. E. Eichinger and P. J. Flory. *Trans. Faraday Soc.*, **64**:2061–2065, 1968.

[75] R. D. Newman and J. M. Prausnitz. *J. Phys. Chem.*, **76**:1492–1496, 1972.

[76] B. E. Eichinger and P. J. Flory. *Trans. Faraday Soc.*, **64**:2053–2060, 1968.

[77] R. Koningsveld, L. A. Kleintjens, and A. R. Shultz. *J. Poly. Sci. Part A-2: Poly. Phys.*, **8**:1261–1278, 1970.

[78] T. P. Russell, R. P. Hjelm, and P. A. Seeger. *Macromolecules*, **23**:890–893, 1990.

[79] S. Coveney and N. Clarke. *Phys. Rev. Lett.*, **111**:125702–125702, 2013.

[80] D. T. W. Toolan, E. Ul Haq, A. Dunbar, S. Ebbens, N. Clarke, P. D. Topham, and J. R. Howse. *J. Poly. Sci. Part B*, **51**:875–881, 2013.

[81] N. Schuld and B. A. Wolf. *J. Poly. Sci. Part B: Poly. Phys.*, **39**:651–662, 2001.

[82] R Eötvös. 14:33–44, 1886.

[83] S.R. Vashishtha, N. Chand, and S.A.R. Hashmi. *Ind. J. Chem. Tech.*, 9:316–323, 2002.

[84] A. Onuki. *EPL*, 28:175, 1994.

[85] D. E. Haas, D. P. Birnie, M. J. Zecchino, and J. T. Figueroa. *J. Mat. Sci. Lett.*, 20:1763–1766, 2001.

[86] H. Kozuka, Y. Ishikawa, and N. Ashibe.

[87] H. Uchiyama, W. Namba, and H. Kozuka. *Langmuir*, **26**:11479–11484, 2010.

[88] C.C. Han and B. Mozer. *Macromolecules*, 10(1):44–51, 1977.

[89] R. M. Hikmet, S. Callister, and A. Keller. *Polymer*, **29**:1378–1388, 1988.

[90] R. J. Young and P. A. Lovell. *Introduction to polymers*. CRC press, 2011.

[91] D. W. Van Krevelen and K. Te Nijenhuis. *Properties of polymers: their correlation with chemical structure; their numerical estimation and prediction from additive group contributions*. Elsevier, 2009.

[92] M. Muthukumar. *Polymer translocation*. CRC Press, 2011.

[93] E. Antoniou. *Structure-property relationships in associating polymer solutions.* ProQuest, 2008.

[94] W. Luo and N. Zhou. *Journal of Central South University of Technology*, **15**:72–75, 2008.

[95] A. M. Stephen and G. O. Phillips. *Food polysaccharides and their applications*, volume 160. CRC Press, 2010.

[96] D. I. Bower. *An introduction to polymer physics.* Cambridge University Press, 2002.

[97] J. W. Goodwin and R. W. Hughes. *Rheology for chemists: an introduction.* Royal Society of Chemistry, 2008.

[98] J. Läuger, C. Laubner, and W. Gronski. *Physical review letters*, **75**:3576–3579, 1995.

[99] C. Aust, M. Kröger, and S. Hess. *Macromolecules*, **32**:5660–5672, 1999.

[100] M. Geoghegan. *Prog. Poly. Sci.*, **28**:261–302, 2003.

[101] *Properties and Behavior of Polymers* . John Wiley & Sons, 2012.

[102] I. Schmidt and K. Binder. *J. Phys.*, **46**:1631–1644, 1985.

[103] R.A.L. Jones. *Polymer*, **35**:2160–2166, 1994.

[104] X. Li, Y. Han, and L. An. *Polymer*, **44**, 2003.

[105] R. A. L. Jones and R. W. Richards. *Polymers at Surfaces and Interfaces.* Cambridge University Press, 1999.

[106] C. J. Lawrence. *Phys. Fluids.*, **31**:2786–2795, 1988.

[107] A. Munch, C. P. Please, and B. Wagner. *Phys. Fluids*, **23**:102101–1–102101–12, 2011.

[108] G. Rabilloud. *High-performance Polymers: Chemistry and Applications, Volume 3.* Editions Ophrys, 2000.

[109] A. E. Nesterov and Yuri S. Lipatov. *Thermodynamics of Polymer Blends, Volume 1.* CRC Press, 1998.

[110] V. Cregan and S. B. G. OBrien. *Appl. Math. & Comp.*, **223**:76–87, 2013.

[111] N. Sahu, B. Parija, and S. Panigrahi. *Indian. J. Phys.*, **83**:493–502, 2009.

[112] R. Koningsveld, W. H. Stockmayer, and E. Nies. *Polymer Phase Diagrams: A Textbook*. Oxford University Press, 2001.

[113] G. A Buxton and N. Clarke. *Model. Simul. Mater. Sci. & Eng.*, **15**:13–26, 2007.

[114] R. A.L. Jones. *Soft Condensed Matter*. Oxford University Press, 2002.

[115] M. Rubinstein and R. H. Colby. *Polymer Physics*. OUP Oxford, 2003.

[116] S. Middleman. *J. Appl. Phys.*, **62**:2530–2532, 1987.

[117] P. Lambooy, K. Phelan, O. Haugg, and G. Krausch. *Phys. Rev. Lett.*, **76**:1110–1113, 1996.

[118] A. Öztekin, D. E. Bornside, R. A. Brown, and P. K. Seidel. *J. Appl. Phys.*, **77**:2297–2308, 1995.

[119] Y. Li, Y. Yang, F. Yu, and L. Dong. *J. Poly. Sci. Part B: Poly. Phys.*, **44**:19–21, 2006.

[120] C. Xavier. *C Language And Numerical Methods*. New Age International, 2007.

[121] V. Cregan. Initial-boundary Value Problems in Industry. 2011. PhD. University of Limerick.

[122] S. M. Akers, J. L. Conkle, S. N. Thomas, and K. B. Rider. *J. Chem. Educ.*, **83**:260–262, 2006.